

**The characterisation of the first SmartPET
HPGe planar detector.**

Thesis submitted in accordance with the requirements of
the University of Liverpool for the degree of Doctor in Philosophy

by

Gerardus Henricus Bernardus Turk

Oliver Lodge Laboratory

April 2006

Abstract

The characterisation of the first SmartPET
HPGe planar detector.

Gerardus Henricus Bernardus Turk

The SmartPET project is aiming to use two HPGe planar detectors to improve a small animal PET system. The detailed analysis of the performance of one of the detectors is the subject for this work. The detector has a $60 \times 60 \times 20$ mm HPGe crystal electrically segmented into $5 \times 5 \times 20$ mm orthogonal strips on opposite faces of the crystal. The average energy resolution is measured to be 1.4 keV. This work shows that the position resolution beyond the initial segmentation can be improved by using the combination of digital electronics and pulse shape analysis.

Two orthogonal surface scans have been performed using γ radiation on the crystal to be able to improve the position sensitivity in all 3 dimension. The response of the detector is calibrated against different positions of a 662 keV collimated beam of γ -rays. A calibration method has been developed to find the optimum position resolution using both the real and transient charge signals measured from the strips.

All signals are parameterized to provide the response in depth (i.e. along the short axis of the crystal). The real charge signals are parameterized by using the $T_{1,70}$ and the $T_{1,40}$ rise times for the AC and DC side respectively. The transient charge signals are corrected for lateral dependence before they are used for a depth measurement. The optimum position resolution in depth is obtained by splitting the depth into two parts and using the transient charges of the AC and DC side to identify extract the depth. The lateral position resolution can only be improved by using the transient charges of each side of a particular strip. The outcome of this investigation is a position resolution of $1.1 \times 1.7 \times 1.2$ mm for the information from the AC, DC contacts and depth respectively.

Believe nothing just because a so-called wise person said it.

Believe nothing just because a belief is generally held.

Believe nothing just because it is said in ancient books.

Believe nothing just because it is said to be of divine origin.

Believe nothing just because someone else believes it.

Believe only what you yourself test and judge to be true.

The Buddha

Acknowledgements

I would like to take this opportunity to thank all the people who supported me throughout my Ph.D.. I would like to thank to following people in particular:

- Prof. P.J. Nolan for giving me the opportunity to do a Ph.D. and for the discussions when I was finishing this work.
- Dr. A.J. Boston, for his supervision, and Dr. H.C. Boston for all the help in the lab.
- The Medical Research Council (MRC) to provide me with the funding to do my Ph.D.
- I would like to thank my parents and sister for your continuous support throughout my Ph.D.
- Jenny Dobson for your friendship and for all the discussions we had. Thank you also for proof reading my thesis.
- The rest of the detector characterisation group, in particular Majid, Sebastian, Andy, Ren, Matt, Laura, David and Alex.
- The members of staff in the nuclear structure group, especially Terry Burns, Dr. J. Cresswell, Dr. R. Herzberg, Mark Norman, Janet Sampson and Ian Lazarus (Daresbury Laboratory). I also would like to thank the rest of the students, postdocs and members of staff in the nuclear structure group for all the help provided.
- The Total Taekwondo Club with all its members. Especially Master P. Hankin for all the encouragements throughout the training.
- I also would like to thank my housemates over the last four years. In particular, Simon, Andrew, Ged, Suzy, Kim, Sarah, Kate, Verity and Pete.

Thank you all very much.

Contents

Contents	i
1 Introduction	1
1.1 The PET imaging technique	1
1.2 Small animal imaging	2
1.3 The improvement SmartPET can make	2
1.4 Research aims	3
2 The Physical Principles of Radiation Detection	4
2.1 Interactions of γ -rays with matter	4
2.1.1 Photoelectric effect	6
2.1.2 Compton scattering	6
2.1.3 Pair Production	7
2.2 Semiconductor materials	8
2.3 Germanium detectors	10
2.4 Production of charge carriers	10
2.5 Signal generation	12
2.5.1 Electric field	12
2.5.2 Weighting Field	14
2.5.3 Lattice orientation	15
2.6 Implications of the weighting field on the signal generation	16
2.6.1 Real charge signals	16
2.6.2 Transient charge signals	17
2.6.3 Preamplifier response	19

2.7	Detector operational characteristics	20
2.7.1	Energy resolution	20
2.7.2	Efficiency	21
3	Experimental setup	23
3.1	The 1st SmartPET detector	23
3.2	Scanning setup	24
3.3	Data acquisition system	26
3.4	Trigger	26
3.5	Scanning methods	27
4	Basic detector characteristics	30
4.1	Signal characterisation	30
4.1.1	Baseline offset and noise level	30
4.1.2	Preamplifiers	31
4.2	Intensity map	31
4.2.1	The side scan	32
4.2.2	The front face scan	33
4.3	Multiplicity for 662 keV γ -rays	34
4.4	Energy resolution and charge collection	35
4.4.1	The charge sharing of DC11	37
4.4.2	Depth depending charge collection	37
4.5	Efficiency	39
4.6	Cross-talk	40
5	The signal analysis of the SmartPET detector	43
5.1	The concept of Pulse Shape Analysis	43
5.1.1	The parameterisation of real charges	44
5.1.2	The parameterisation of transient charge	44
5.2	The detector response - rise time, transient charge area	44
5.2.1	Rise time plots	46
5.2.2	Transient charge areas	46
5.3	Filtering method	46

5.4	Depth information from the pulse shape	52
5.4.1	Considerations of the parameterisation for the depth	54
5.4.2	The choice of parameterisation of the pulse shapes	54
5.5	Depth dependence of the transient charges	56
5.5.1	Parameterisation of the transient charge	56
5.5.2	Average transient charge database	57
5.5.3	The transient charge value through depth	61
5.6	The improvement in position resolution	61
5.6.1	Rayleigh criterion	63
5.6.2	Depth position	63
5.6.3	Lateral position	65
6	Conclusion and discussion	75
6.1	Conclusion	75
6.2	Discussion	77
6.3	Future work	78
A	Energy measures	80
B	Weighting field construction	83
B.1	A simple model	83
B.2	Comparison with experiments	86
C	Average transient response within a strip	89
D	Position resolutions	98

List of Figures

2.1	The total linear attenuation coefficient is built out of the three individual interaction processes. In the region of interest, the dominating factors for germanium are photoelectric absorption (20- 175 keV) and Compton scattering (175 - 6000 keV).	5
2.2	Interaction mechanisms for γ -rays in hyper pure germanium.	6
2.3	Scattering profile for different energies. The initial γ -ray is coming from the left.	7
2.4	The band gap structure for insulators, semiconductors and conductors. Hyper pure germanium is a semiconductor with a band gap energy of 0.75 eV.	9
2.5	When there is a thermal equilibrium, the Fermi energy (E_f) is equal throughout both types of material. The conduction (E_c) and valence energy (E_v) of the two sides are therefore different from each other.	10
2.6	The three Miller indices are shown on top. From left to right it is [100], [110] and [111]. The Face Centered Cubic structure of germanium is shown below them.	11
2.7	A schematic diagram of a planar germanium configuration. The AC-side has the high voltage applied which will, with a negative polarity, collect the holes. The electrons are collected on the DC side.	12
2.8	The lines of equal potential for the weighting field for electrode 3 are shown. The current induced on the sensing electrode 3 is drawn for two different interaction points: an interaction within the electrode 3 and an interaction within the adjacent electrode 2	15
2.9	The electron drift velocity as a function of electric field strength for different lattice orientations: $\langle 111 \rangle$ green, $\langle 110 \rangle$ blue, $\langle 100 \rangle$ red [Mih00].	16

2.10	The weighting field for the strip with an interaction has been calculated for a detector with a strip pitch to thickness ratio of 1 to 6. The shape of the real charge induced is dependent on the depth of the interaction position. The inducing electrode is placed at depth = 0.	17
2.11	The weighting potential for the adjacent strip has been calculated for a detector with a strip pitch to thickness ration of 1 to 6. Three regions have been pointed out. These regions represent the regions where the positive, bipolar and negative transient charges occur.	19
2.12	A simplified circuit diagram of a charge sensitive preamplifier. [Kno00a]	20
3.1	The first SmartPET planar germanium detector	24
3.2	The dimension of the HPGe crystal showing the orthogonal segmentation on both sides of the detector	25
3.3	The scanning setup with the detector positioned for the front face scan (left). The 1 mm diameter Tungsten collimator is drawn schematically on the right. The collimator is mounted inside the lead.	25
3.4	The DC signal is used as the trigger of the data acquisition. The system gets triggered if an energy deposition of > 50 keV is measured.	27
4.1	An intensity map has been made using the side scan data. The design of the detector only allows the AC strips to be visible.	33
4.2	An intensity map has been made using the front face scan data. Both AC and DC strips are clearly visible.	34
4.3	The multiplicity has been investigated for both the AC and DC sides separately. A total energy deposition of 662 keV was required defined by an energy gate of 650- 670 keV.	35
4.4	The energy resolutions for the strips on the AC and DC side measured with conventional analogue electronics. The shaping time was set to 6 μ s.	36
4.5	The charge sharing of DC11 has been investigated. The photo peak energy of DC11 varies when a interaction is required in one of the AC strips.	36

4.6	The energy resolution of the DC signals is degrading ~ 4 mm from the AC contacts (top). From this point the collected energy, expressed as the peak position, shows a stronger decrease. The AC signals do not show a significant change in position or resolution.	38
4.7	The absolute efficiency for the two different size contacts (AC: $0.3 \mu\text{m}$ thick, DC: $50 \mu\text{m}$ thick). The lines drawn are indicating the trend of the efficiency for each side.	40
4.8	The cross-talk behaviour for the AC and DC side. The cross talk can be corrected by adding back the much smaller (~ 5 keV) baseline difference from the adjacent strips. The different lines represent different multiplicity events (i.e. M1 equals multiplicity 1, etc)	42
5.1	An example of a 662 keV M11 event is shown. 6 signals are of interest: 2 real charges and 4 image charges. The DC contacts are rotated for schematic purposes. The figures of the real charges include the three risetime parameterisation of the pulse shape: $T_{10,30}$, $T_{10,60}$ and $T_{10,90}$. The proposed parameterisation of the transient charges is shown by the shaded area underneath the 4 signals.	45
5.2	Rise time distribution for the AC and DC side. The arrows are indicating the peaks at the start and end of the $T_{10,30}$ distributions. The peaks are an indication of a non-linear behaviour towards the edges of the detector discussed in section 5.4.1. The fastest peak (1) is due to only one charge carrier inducing the charge inside the detector. The slower peak (2) is caused by the starting point (T_{10}) of the risetime parameter.	47
5.3	The area of the transient charges from either side of the real charge are plotted against each other for both sides. Two lines are drawn in the figures which show the asymmetry and the polarity of the transient charges.	48
5.4	The filtering method to achieve the most probable pulse shape	51
5.5	The sum of squares vs number of excluded pulse shapes (AC side). The lines in red represents depths close to the DC side (1 - 10 mm). The lines in blue represents depths close to the AC side. (11 - 20 mm). The black line represents a dataset of background events.	52

5.6	Pulse shapes varying with depth. The AC signals are shown in the top graph. The DC signals are shown in the bottom graph. The colour scheme is the same for both graph: the lines in red represents depths close to the DC side (1 - 10 mm), the lines in blue represents depths close to the AC side. (11 - 20 mm)	53
5.7	Nine different responses are shown with varying end-points for the rise time measurement. The starting point is set to T_1 . The responses of the AC and DC side are shown.	55
5.8	The transient charge area from the adjacent strips are added together to correct for the lateral dependence. A uniform lateral response is shown for the AC and DC side.	58
5.9	The average transient charge shape for different depths for the AC signals. The two different types of transient charges do vary in amplitude but also in shape. It can be seen that the number of negative transient charges is larger for the next-to-adjacent transient charges than for the adjacent transient charges.	59
5.10	The average transient charges shapes for different depths for the DC signals. The same observations can be made as with the AC transient charges (see figure 5.9) the adjacent transient charges are larger in amplitude and there are less negative transient charges.	60
5.11	The area of the transient charge for each depth.	62
5.12	The position resolution has been measured using four different techniques. For depths without position resolution, the values were too large to put in the graph (see text for details).	65
5.13	The first method (top) as a depth determination uses the adjacent transient charge area of the AC and DC side. The separation between the most sensitive region is set at 12 mm because the AC transient charges provide a better position resolution past this point (see figure 5.12). The combination of the $T_{1,70}$ rise time of the AC side and the transient charge area (bottom) are used as a comparison with the first method used. This method provides a slightly worse position resolution for the first part of the detector.	66

5.14	The reconstructed position has been calculated by using the combination of two methods. Both methods show good agreement with the collimator position. The error bars are indicating the position resolution. Note that the graphs are drawn on different axis.	67
5.15	Asymmetry for the transient charge on AC side using the collimator position of the scanning table. Position 1 and 5 are close to the strip boundary. Position 3 is in the middle of the strip. The insensitive region is the region where the asymmetry changes polarity.	68
5.16	Asymmetry for the DC side using the AC and DC transient charges to reconstruct the depth position. A similar insensitivity can be seen using the DC transient charges. It is positioned on the opposite side of the detector, close to the DC contacts.	72
5.17	The position resolutions expressed as the Rayleigh criterion for all three dimensions.	74
6.1	The parameterisation of the real charge should be changed so the complete signal is used. Shown are two different pulse shapes for an interaction close to and far away from a contact. The area underneath the signals are significant different. This should reduce the noise level on an event-by-event basis and could have potential to deconvolve multiple / convolved events.	79
A.1	The working of moving window deconvolution method is shown in this schematic. The trapezoid width equals twice the average window. The sample time is the length of the trace used for the decay correction. The peak sample time defines the position where the average is taken from. This should be chosen just before the sample time so no rise time effects interrupt the measure of the energy. The peak separation time is the time the complete process takes. This is important for baseline calculations.	82
B.1	Twelve points have been taken to show the concept of the weighting field. Four interaction depths are chosen within each strip. The lines drawn are indicating the coverage of the Coulomb field by the electrode.	84
B.2	The weighting field constructed out of the two parameters of coverage and distance. The graph is split up into three regions defining the shape of the transient charges.	86
B.3	The weighting field reconstructed compared with the data	87

List of Tables

2.1	The physical properties of germanium [NSM]	11
3.1	The different symbols used as a description for the various scans of the detector described later.	29
4.1	The preamplifier baseline offset and peak-to-peak noise level for each of the strips .	31
5.1	The depth for the example event of figure 5.1 is determined using the four different methods. Note that according to figure 5.11 the adjacent transient charges on the DC side are not very sensitive. The AC side are more sensitive in this region. . . .	63
5.2	The position resolution expressed using the Rayleigh criterion for each depth. The two methods best suitable to reconstruct the depth are highlighted in bold. . . .	64
5.3	Average lateral position resolution for the AC side scan using different methods for depth. The figures highlighted in bold are used to calibrate the AC side asymmetry. The italic figures are indicating the regions where the depth measure is not sensitive (see figure 5.12). The purpose of this table is to show the influence of the different methods of determining depth on the position resolution in lateral position. All figures are expressed as the Rayleigh criterion. Depths with a larger position resolution than 5 mm should be considered as insensitive throughout the strip width. The larger value is due to the method of calculating the position resolution. . . .	70
5.4	The average lateral position resolution has been calculated using the front face data set for both the AC and DC side. The depth is reconstructed by using the AC and DC transient charges. The positions with a position resolution over 5 mm should be considered for the trend but not for an exact value.	73

A.1	MWD parameters used to improve the energy resolution	81
A.2	The energy resolution for strip AC06 measured with the three different methods. The three methods are ordered in worsened resolution.	81
B.1	The weighting field values for the twelve points chosen.	85
C.1	Adjacent transient charges for depths 1 - 3 mm	90
C.2	Adjacent transient charges for depths 4 - 8 mm	91
C.3	Adjacent transient charges for depths 9 - 13 mm	92
C.4	Adjacent transient charges for depths 14 - 18 mm	93
C.5	Next-to-adjacent transient charges for depths 1 - 5 mm	94
C.6	Next-to-adjacent transient charges for depths 6 - 10 mm	95
C.7	Next-to-adjacent transient charges for depths 11 - 15 mm	96
C.8	Next-to-adjacent transient charges for depths 16 - 18 mm	97
D.1	The position resolution based on the Rayleigh criterion for the lateral position as a function of depth. The position resolutions over 5 mm are due to the method chosen for the calculation. (-) means no peak could be identified in the distribution.	99

Chapter 1

Introduction

The work presented in this thesis is part of the SmartPET project. The aim of the project is to develop a PET scanner using hyper pure germanium (HPGe) detectors. The detection system consists of two HPGe planar detectors. The subject of this work is to improve the position resolution by using digital electronics and pulse shape analysis.

1.1 The PET imaging technique

Positron emission tomography (PET) scanners have been around for several decades to image whole or parts of bodies. The principle of PET imaging is based on the detection of an annihilation event of a positron and electron. With the annihilation of the particles, two 511 keV γ -rays are emitted back-to-back. The object to be imaged and the γ -rays emitted can be surrounded by a ring of detectors, detecting both 511 keV γ -rays at the same time. A line of response can be drawn between the two detectors which have detected the γ -rays. When this is done for many events, the original position of emission can be reconstructed by developed algorithms [She82][Lan84]. The spatial resolution of the system defines the width of the reconstructed position. The spatial resolution for whole body imaging system used in hospitals is ~ 5 mm [Tar03].

To get the positron annihilation, a radioactive positron emitter has to be injected in the patient. The radioactive marker consists of a specific labelled chemical. The chemical of choice depends on the tissue of the region where the image should be taken from. The chemical with the positron emitter attached is chosen in a way to provide a high concentration

in the tissue of interest.

1.2 Small animal imaging

The use of PET systems has been extended towards the imaging of small animals (i.e. rats and mice) due to the growing interest for the studies of the development and growth of tumours. There is a requirement for a better spatial resolution compared with a whole (human) body system due to the small object size. The main improvement comes about by using smaller size detector crystals. Currently used small animal PET scanning system achieve a spatial resolution of 1.1 mm^3 [Mis04]. The detectors used in current systems are mainly LSO scintillators with a crystal size of $1.5 \times 1.5 \times 10 \text{ mm}$.

1.3 The improvement SmartPET can make

One of the factors influencing the quality of the image is the position resolution determined by the size of the detectors. To get an accurate line of response through the point of emission, the position of the interaction point should be determined as accurate as possible. In scintillator detectors, the position resolution can not be improved beyond the size of the crystal which is a drawback for their use. By decreasing the size and hence increasing of the number of crystals, the electronics and the reconstruction algorithms become very complex and hence is not feasible.

Since the 1970's, semiconductor technology has been improved significantly. The semiconductor detectors have been used in the field of nuclear physics research configured in different arrays [Nol94] and developments in this field have been ongoing for years. Due to the development towards new γ -ray tracking arrays [Aga01], the detector development is now at the stage where it can be applied to the field of medical imaging.

The SmartPET project is the development of a small animal PET system using HPGe detector technology. The electrical segmentation of these detectors can vary for different configurations but will not achieve the aim required for small animal PET systems. However, the semiconductor technology allows an improvement of the position resolution beyond the electrical segmentation using digital techniques and pulse shape analysis.

1.4 Research aims

The work for this thesis is on the first SmartPET planar germanium detector. The aims are:

- To gain a better understanding of the signal generation within hyper pure germanium planar detectors.
- To develop algorithms which supply more information about the interaction position using pulse shape analysis.
- To use the developed algorithms to improve the position resolution.

Chapter 2

The Physical Principles of Radiation Detection

An outline of the background knowledge is required to understand the working of the detector. In this chapter every step towards the signal generation is described. This involves photon interactions with matter, semiconductor physics, signal generation and preamplifier response.

2.1 Interactions of γ -rays with matter

The interaction of γ -ray radiation with matter involves different processes [Dav52a], such as photoelectric absorption (PE), coherent (Compton scattering (CS)) and incoherent scattering (Rayleigh scattering) and pair production (PP). The interaction processes which involves energy exchange are of interest of this work. The total cross section of an interaction taking place can be found by adding each individual cross section:

$$\sigma_{total} = \sigma_{PE} + \sigma_{CS} + \sigma_{PP} \quad (2.1)$$

The linear attenuation is the product of the cross section and the number of atoms released (N) after the interaction:

$$\mu = N\sigma = \left(\frac{N_a\rho}{A}\right)\sigma \quad (2.2)$$

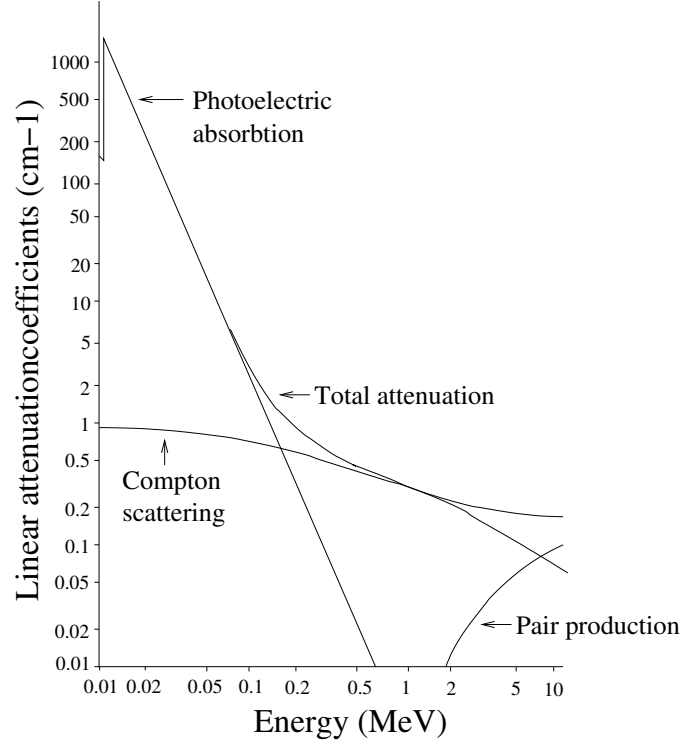


Figure 2.1: The total linear attenuation coefficient is built out of the three individual interaction processes. In the region of interest, the dominating factors for germanium are photoelectric absorption (20 - 175 keV) and Compton scattering (175 - 6000 keV).

where μ is the linear attenuation coefficients, N_a Avogadro's number, ρ the material density and A the atomic weight. Figure 2.1 shows the linear attenuation coefficients for three different processes as a function of energy [Har84]. In the energy range of interest for the project (i.e. 50 keV - 1 MeV), PE and CS are the dominating processes. The fraction of an incident beam of γ -radiation penetrating through a material is described by:

$$I = I_0 e^{-\mu t} \quad (2.3)$$

where I_0 is the initial intensity, t equals the material thickness and I the intensity after the material. The linear attenuation coefficient can also be expressed as the mean free path which is the reciprocal of it.

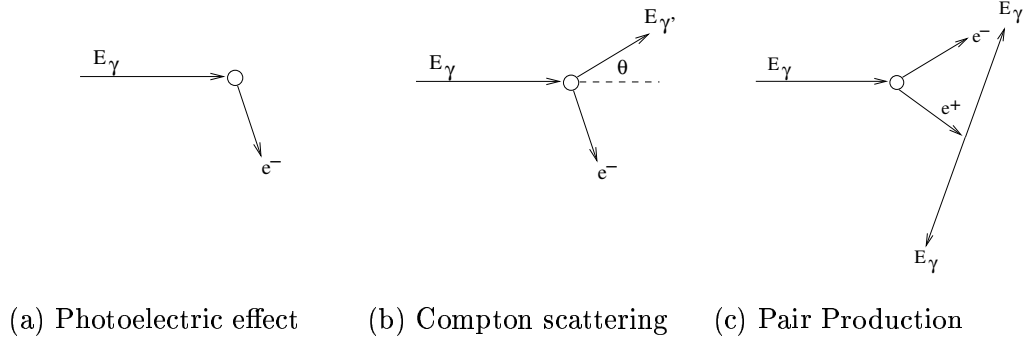


Figure 2.2: Interaction mechanisms for γ -rays in hyper pure germanium.

2.1.1 Photoelectric effect

For energies smaller than ~ 150 keV, the dominating type of interaction is the photoelectric effect. The photon is interacting with the most tightly bound electron. The free photoelectron is created by a γ -ray interaction (see figure 2.2a). The energy transferred as kinetic energy to the electron is the excess of the energy it takes to create an electron-hole pair over the binding energy. The binding energy of germanium is in this energy range neglectable.

$$E_{e^-} = E_\gamma - E_b \quad (2.4)$$

where E_b is the binding energy and E_γ is the initial energy of the γ -ray. After the electron has been released from the atom, the atom becomes positively charged (i.e. a hole). The probability of an incoming γ -ray interacting with matter by the photoelectric effect is given by equation 2.5 [Dav52b].

$$P_{photoelectric} = Constant \times \frac{Z^5}{E_\gamma^{7/2}} \quad (2.5)$$

As shown, the probability varies strongly with both atomic number and γ -ray energy. A high Z material has a much higher PE cross section.

2.1.2 Compton scattering

For γ -rays with an energy between ~ 150 keV and 6 MeV, the most probable interaction process is a Compton scatter (figure 2.2b). The γ -ray interacts with a weakly bound atomic

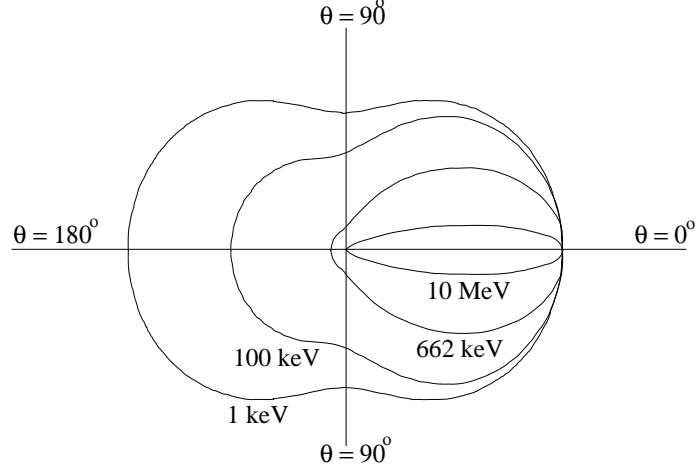


Figure 2.3: Scattering profile for different energies. The initial γ -ray is coming from the left.

electron but only depositing part of its energy. The energy deposited is transferred to an electron and the γ -ray still continues to exist but with a reduced energy. The secondary γ -ray can undergo either another Compton scatter or is fully absorbed by the photoelectric effect.

The scattering angle (θ) is depending on the initial energy and defines the energy of the secondary γ -ray. The Klein-Nishina formula [Dav65] describes the angular probability of the scattering process (figure 2.3). The higher the initial energy, the more likely the γ -ray is scattering forward ($\theta < 90^\circ$). For a 511 keV γ -ray, the scattering profile is forward. Equation 2.6 is used to derive the secondary γ -ray energy ($E_{\gamma'}$) which is dependent on the scattering angle

$$E_{\gamma'} = \frac{E_{\gamma}}{1 + \frac{E_{\gamma}}{m_e c^2} (1 - \cos\theta)} \quad (2.6)$$

where E_{γ} is the initial energy in the γ -ray before the interaction and the θ is the scattering angle.

2.1.3 Pair Production

Above an energy of 1022 keV (twice the rest mass of an electron) pair production can occur. The interaction can only happen in the Coulomb field of a nucleus to conserve momentum.

In a pair production interaction an electron and positron are created which together hold the total γ -ray energy (figure 2.2c). If the energy exceeds 1022 keV, the excess energy is transferred as kinetic energy to both particles. The positron annihilates after a short distance ($\lesssim 1$ mm) with a free electron emitting two back-to-back 511 keV γ -rays. Pair production in germanium is dominant above an energy of 6 MeV.

2.2 Semiconductor materials

Solid material can be categorised into 3 different groups: insulators, semiconductors and conductors, which vary in electrical properties. The electrical properties of a material is related to the number of free (unbound) electrons inside the material. The number of free electrons depends on the band gap energy and the thermal energy [Sze02a]. The band gap energy (E_g) is defined as the energy it takes to move one electron from the valence band to the conduction band. An insulator has a band gap energy of > 5 eV. The band gap in semiconductors is smaller than an insulator (~ 1 eV). In conductors the valence and conduction bands are overlapping. The thermal energy is described by:

$$E = \frac{3}{2}kT \quad (2.7)$$

where E is the thermal energy, k is the Boltzmann constant and T is the temperature. The differences between the materials are shown schematically in figure 2.4.

In order to modify the electrical properties of a semiconductor, it is possible to add impurity atoms to the material, which can modify the effective band gap energy. The impurity atoms have either an electron extra (n-type atoms from group V) or an electron less (p-type atoms from group III) than the bulk semiconducting material. N-type impurity atoms are also called donors, where p-type are also known as acceptors. In the case of n-type doping, the extra electron inhabits an energy level between the conduction and the valence band (see figure 2.5), which results in a smaller band gap energy.

When n-type and p-type material are put together in good thermal contact, the excess charge carriers can diffuse across the contact. This is called a p-n junction. Whenever the extra electrons of the n-type material come into contact with holes of the p-type material recombination happens. This recombination process continues until the impurity concen-

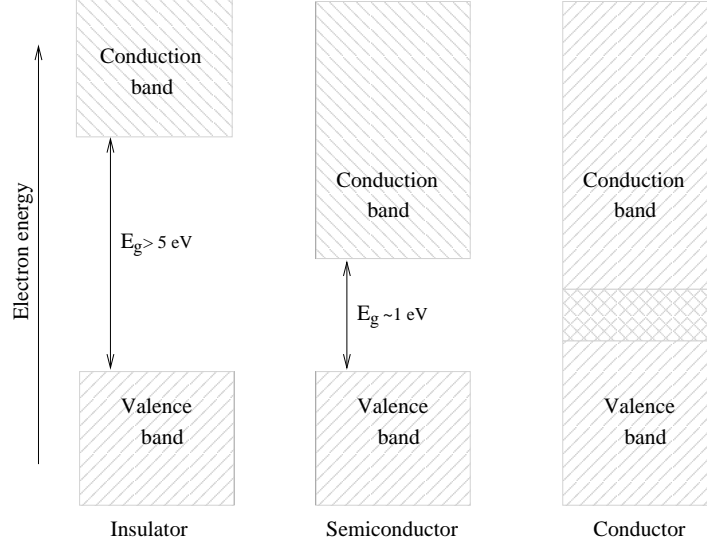


Figure 2.4: The band gap structure for insulators, semiconductors and conductors. Hyper pure germanium is a semiconductor with a band gap energy of 0.75 eV.

tration on both sides of the junction is equal. Although a lot of recombinations happened, both sides still have an excess of impurity atoms from being a n-type or p-type material. This can be seen in the figure as the difference between conduction energy (E_c) and fermi energy (E_f). Whenever one of the excess charge carriers drifts into the depletion region, it will find a region of the opposite polarity. If the energy of the particle entering is not large enough to cross the depletion region, it gets forced back into its original region. A reverse bias applied across the material makes it less likely for excess charge to cross the depletion region. This can also be seen as an expansion of the depletion region because the charge carriers are pulled to one side of the doped material.

For a planar p-n junction, the size of the depletion region can be calculated by equation 2.8, where d is the depletion region, V is the reversed bias applied, ϵ is dielectric constant of the material and N equals the impurity concentration [Sze02b].

$$d \simeq \left(\frac{2\epsilon V}{eN} \right)^{0.5} \quad (2.8)$$

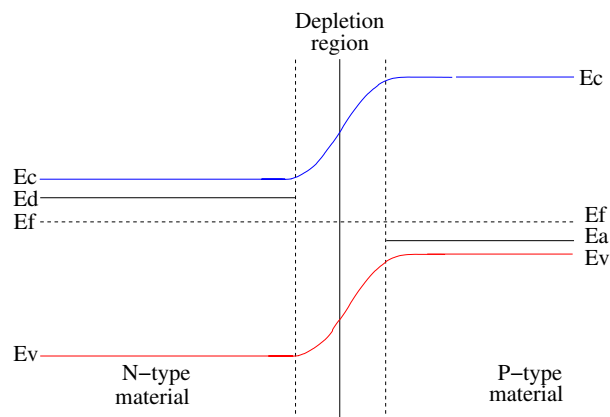


Figure 2.5: When there is a thermal equilibrium, the Fermi energy (E_f) is equal throughout both types of material. The conduction (E_c) and valence energy (E_v) of the two sides are therefore different from each other.

2.3 Germanium detectors

Germanium is a widely used semiconducting material. Table 2.1 shows the electrical properties of germanium. It is an element from group IV of the periodic table. It has a face centred cubic (FCC) or cubic closed structure (see figure 2.6). Hyper pure germanium is widely used as a radiation detector due its excellent energy resolution. There are two different detector configurations existing: i.e. planar and coaxial. Figure 2.7 shows a schematic drawing of a planar detector. The high voltage is applied to the AC side of the crystal. The DC side is grounded. It depends on the polarity of the high voltage, which of the charge carrier is collected at which contact.

2.4 Production of charge carriers

In all γ -ray interactions where energy is deposited, there is an electron released with a large kinetic energy. For energies below a few MeV, the electron loses its energy by the ionisation of other atoms. This is described as function of path length by the Bethe-Bloch formula [Knp65].

The volume where the electron loses its energy is small ($< 1 \text{ mm}^3$). The number of electron/hole pairs created in the electron cloud is related to the energy of the incoming

Atomic Number A	32
Atomic Weight Z	72.6
Atoms	$4.4 \times 10^{22} \text{ cm}^{-3}$
Density	5.32 g/cm^{-3}
Crystal Structure	diamond (FCC)
Dielectric constant ϵ_r	16.2
Intrinsic carrier concentration (300 K)	$2.0 \times 10^{13} \text{ cm}^{-3}$
Intrinsic resistivity	$46 \Omega \cdot \text{cm}$
Energy gap (300 K)	0.67 eV
Energy gap (0 K)	0.75 eV
Ionization energy (77 K) ϵ_{pair}	2.96 eV
Fano factor (77 K)	0.08
Electron mobility (300 K)	$3900 \text{ cm}^2 \text{ V} \cdot \text{s}$
Hole mobility (300 K)	$1900 \text{ cm}^2 \text{ V} \cdot \text{s}$
Lattice constant (a)	565.75 pm

Table 2.1: The physical properties of germanium [NSM]

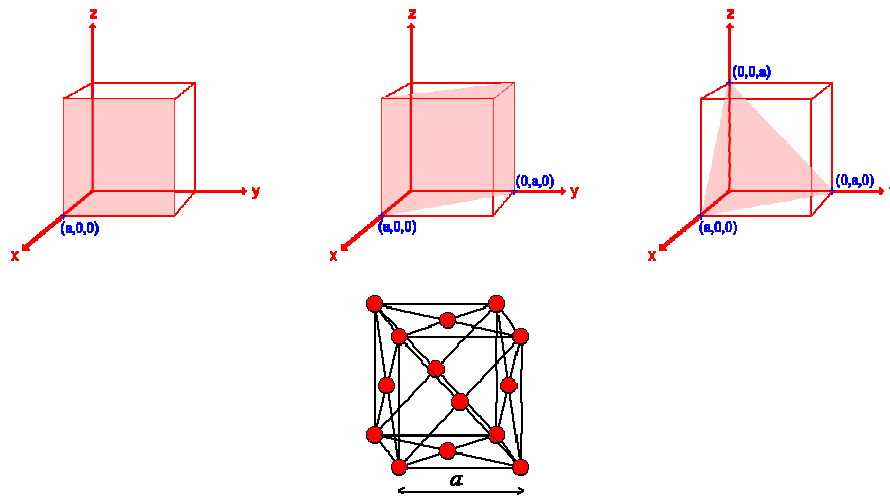


Figure 2.6: The three Miller indices are shown on top. From left to right it is [100], [110] and [111]. The Face Centered Cubic structure of germanium is shown below them.

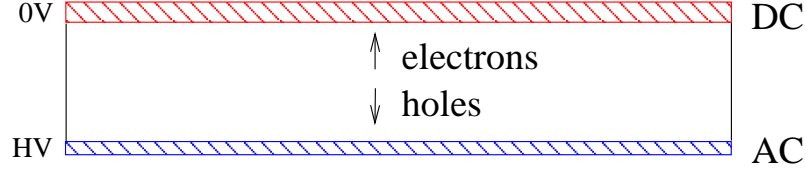


Figure 2.7: A schematic diagram of a planar germanium configuration. The AC-side has the high voltage applied which will, with a negative polarity, collect the holes. The electrons are collected on the DC side.

γ -ray and the ionization energy (ϵ_{pair}):

$$N_{pair} = \frac{E_{\gamma}}{\epsilon_{pair}} \quad (2.9)$$

where N_{pair} is the number of electron/hole pairs created, E_{γ} is the gamma ray energy and ϵ_{pair} equals the germanium ionisation energy ($\simeq 3 \text{ eV}$). The statistical spread of the number of electron/hole pairs varies from a Poisson process because each interaction is not independent. To correct for this, the Fano factor [Fan47] has been introduced (Eq. 2.10).

$$\Delta N_{pair} = \sqrt{F N_{pair}} = \sqrt{F \frac{E_{\gamma}}{\epsilon_{pair}}} \quad (2.10)$$

The Fano factor (F) of germanium is about 0.08 which is small compared to other materials used as detectors. By having a small Fano factor, the variance in number of free electrons per event is small which will leads in a smaller spread in energy. Hence the excellent energy resolution.

2.5 Signal generation

Once the electron cloud has been created, there are three factors of the signal generation, i.e. the electric field, the weighting field and the lattice orientation.

2.5.1 Electric field

The detector signal is generated by the movement of the electron/hole pairs. As the electric field created by the junction is too small to move the charge carriers towards the edges of

the crystal an external electric field is applied to improve this. The high voltage is chosen to fully deplete the thickness of the detector using equation 2.8.

The field strength at each point in the detector crystal can be calculated by solving the Poisson equation for points inside the detector:

$$\frac{d^2V(x)}{dx^2} = -\frac{\rho(x)}{\epsilon} \quad (2.11)$$

where $V(x)$ is the electric potential, $\rho(x)$ is the charge density and ϵ is the dielectric constant of the detector material.

By doing this for a planar configuration, the electric field strength at each point inside the detector is described by equation 2.12 for the uniform part (i.e. middle of the crystal) of the detector.

$$|E(x)| = \frac{V(x)}{d} + \frac{eN_A}{\epsilon} \left(x - \frac{d}{2} \right) \quad (2.12)$$

where x is the depth inside the detector, d is the detector thickness and N_A equals the impurity concentration. The equation shows a linear behaviour of the electric field strength through depth. The electric field determines the trajectory and velocity of the charge carriers. The influence of the electric field on the drift velocity can be calculated by:

$$v_d(x(t)) = \mu_{e,h}E(x) \quad (2.13)$$

where $\mu_{e,h}$ is the mobility of the electron and holes. Both equation 2.8 and 2.12 are assuming an infinite long detector. However in reality this is not the case which results in a weaker electric field near the edges of the contacts.

The current inside the detector has been calculated by Ramo [Ram39] and is proportional to the field strength and the velocity of the charge carriers:

$$i(t) = q \frac{E(x)v_d(x,t)}{V(x)}, \quad (2.14)$$

where $E(x)$ is the electric field strength at the position of the charge, v_d the drift velocity and $V(x)$ the electric potential.

2.5.2 Weighting Field

The cloud of charge carriers inside the detector has a Coulomb field extending throughout the complete volume of the detector and hence will also cover each electrode of the detector. When the cloud of charge carriers is moving under the force of the electric field, the Coulomb field is changing with time. The electrodes convert the change of the Coulomb field into a current. Because the Coulomb field is not homogeneous throughout the complete detector volume, the induced current changes depending on the position of the charged particle. The weighting field ¹ is a normalised measure related to the induced current for each position inside the detector and therefore is of importance for the signal analysis in the detector. The current induced can be calculated by:

$$i(t) = -qE_w(x)v_d(x(t)) \quad (2.15)$$

where E_w is the weighting field and v_d the drift velocity which is dependent on the electric field and the electron/hole mobility ($\mu_{e,h}$).

The weighting field can be calculated by solving the Poisson equation for a unit voltage on the electrode of interest where all others are grounded [Sho38]. This is done for a specific configuration and shown in figure 2.8. As the figure show the weighting field is depending on the geometry (i.e. strip size, interstrip gap size and thickness) of the detector. With a small strip size, a very small area of the Coulomb field is covered by the electrode. A change in this part of Coulomb field will therefore induce a small amount of current and hence will not be very sensitive. This is also known as the small electrode or small pixel effect [Ham96]. Although this effect is especially important when the strip size is of the same order as the thickness of the detector, this effect is also present in detectors with larger contact.

The charge can be calculated from the induced current [Rad88]:

$$Q = \int i(t)dt = -q \int_{x_2}^{x_1} E_w dl = q[V_w(x_1) - V_w(x_2)] \quad (2.16)$$

¹Two terms are used describing the effect of the Coulomb field on the electrode: the weighting field and the weighting potential. The difference between these two terms is similar to the terms used to describe electric field and electric potential. The weighting field includes a collection of weighting potential for a certain area / plane. The weighting potential varies for each point inside the detector crystal.

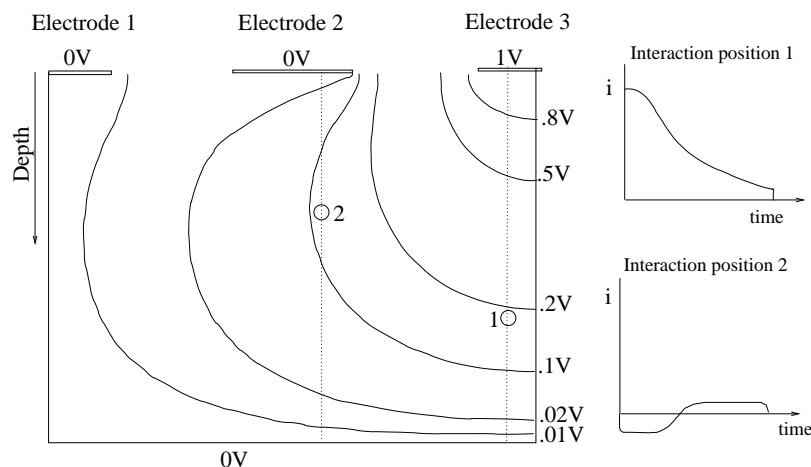


Figure 2.8: The lines of equal potential for the weighting field for electrode 3 are shown. The current induced on the sensing electrode 3 is drawn for two different interaction points: an interaction within the electrode 3 and an interaction within the adjacent electrode 2

where Q is the collected charge, $i(t)$ is the induced current, x_1 and x_2 the position before and after the displacement of the charge carriers, V_w the weighting potential. Equation 2.16 shows that the induced charge is proportional to the difference between two points in the weighting field (i.e. the gradient of the weighting field). The lines of equal potential in figure 2.8 are showing that the gradient is a lot larger close to the contact and hence the induced charge in this region will be a lot higher. Appendix B discusses the origin of the weighting field in more detail.

2.5.3 Lattice orientation

The induced charge is a function of the drift velocity. In germanium detectors, the drift velocities of the charge carriers is depending on the crystal plane in which they travel through the crystal. Figure 2.9 shows the drift velocity as a function of electric field strength for the three crystal orientations [Mih00]. In a planar germanium detector, the drift direction is for the majority of the crystal parallel to one of its lattice orientation, hence the lattice orientation does not influence the velocity throughout the drift path.

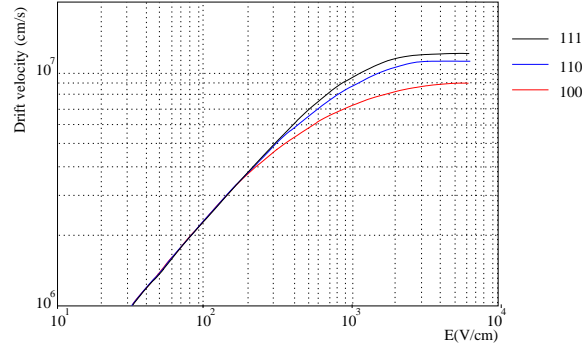


Figure 2.9: The electron drift velocity as a function of electric field strength for different lattice orientations: $\langle 111 \rangle$ green, $\langle 110 \rangle$ blue, $\langle 100 \rangle$ red [Mih00].

2.6 Implications of the weighting field on the signal generation

The technique used to improve the position resolution is called pulse shape analysis (PSA). This technique utilises the shape of the signals to determine the interaction position. Two signals are of importance in PSA: real charge signals and transient charge signals. Real charge signals are induced in strips where the interaction happened and hence where the charge carriers are collected. The transient charges are in theory induced in all other strips. However due to noise, they are mainly seen in the adjacent and next-to-adjacent strips. Both types of signal are influenced by the interaction depth (i.e. the short axis of the crystal). In the absence of noise, each lateral position will affect the shape of the transient charge. However, with noise present it is assumed that the shape of the transient charge is the same for the lateral position inside the strips.

2.6.1 Real charge signals

The shape of the rising edge of the real charge pulse is dependent on the interaction position in depth and the difference in electron/hole drift velocities (see equation 2.15). When the difference in electron/hole drift velocity is ignored, the induced current is only dependent on the weighting field. The weighting field for a detector with a strip pitch to thickness ratio of 1:6 is shown in figure 2.10 [Spi01]. The explanation of the induced signal is done by using

the two charge carriers 1 and 2 traveling in opposite direction inside the detector. For an interaction close the contact (position A), the induced current is initially very large because of the high weighting field. When charge carrier 2 is in the weaker part of the weighting field the remainder of the charge will be collected slower. An interaction at position A will therefore have a quick rise initially and a slower end of the pulse, i.e. a convex pulse shape. For an interaction at position B, the opposite will happen. Initially the induced current is small, but as charge carrier 1 is getting near the contact, the induced current increases. The pulse shape will therefore have a concave shape.

By adding a factor for the drift velocities, the shape of the pulse depends not only on the weighting field but also on which type of charge carrier is inducing the charge.

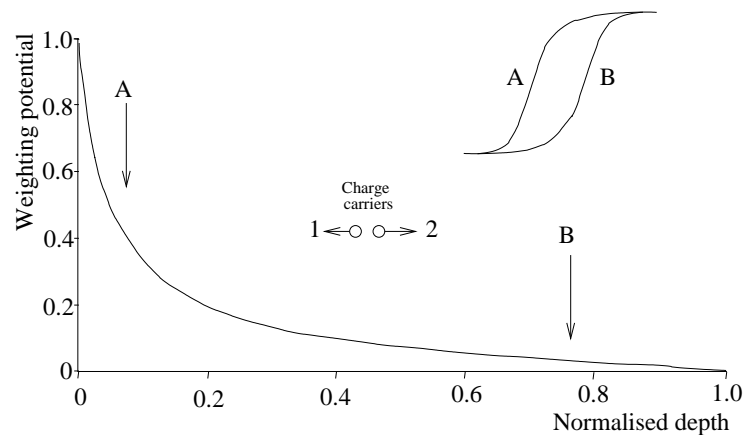


Figure 2.10: The weighting field for the strip with an interaction has been calculated for a detector with a strip pitch to thickness ratio of 1 to 6. The shape of the real charge induced is dependent on the depth of the interaction position. The inducing electrode is placed at depth = 0.

2.6.2 Transient charge signals

As mentioned before, the Coulomb field extends throughout the complete volume of the detector. Therefore the adjacent and the next-to-adjacent strip from the one with the real charge in will show the effect of the interaction (point 2 in figure 2.8). The signals induced in these strips are called transient charges, also known as mirror or image charges.

The shape of the weighting field through depth in the adjacent strips is more complex than the weighting field of the strip with a real charge induced. The shape is dependent on

depth and the amplitude on the lateral position within the strip.

There are three classifications of transient charges: positive, negative and bipolar. To explain the three shapes, it is necessary to look at different regions in depth and the currents induced in these regions.

When the Poisson equation is solved to visualise the weighting potential, the region close to neighbouring opposite strips is 0. The weighting potential is higher in between these two extreme cases. Figure 2.11 [Spi01] shows an example of a weighting field of an adjacent strip.

The charge induced is the difference in weighting potential between two points as equation 2.16 describes. When the two types of charge carriers have been collected, the total difference in weighting potential is zero and hence the transient charge signal will not have any charge induced.

It has been pointed out where each of the three types of transient charges are happening. The shapes are explained along with charge carriers 1 and 2 in the figure 2.11. In the figure, the electrode is placed at depth equal 0 mm. Charge carrier 1 is moving towards the electrode. Charge carrier 2 is moving away from it.

- Positive transient charges: occurs when an interaction is happening inside the region with the negative slope of the weighting field. Charge carriers 1 and 2 will first produce a positive current which is reversed after charge carrier 1 has passed the maximum. This brings the transient charge back to the baseline.
- Negative transient charges: occurs when an interaction is happening inside the region with the positive slope of the weighting field. Here both types of charge carrier produce a large negative current first which is gradually compensated by the positive current after the maximum. If the interaction happens on the negative side of the maximum (i.e. ± 0.15 away from the electrode), the negative current is reduced by a certain amount because charge carrier 2 are inducing a small positive current. This affects the height of negative transient charge.
- Bipolar transient charges: occurs when an interaction is happening after the maximum. Both types of charge carriers will first produce a positive current initially. After charge carriers 1 have passed the maximum these will produce a much larger negative

current due to the larger gradient. After charge carriers 1 have been collected, charge carriers 2 are still producing a small positive current. The small current will bring the transient charge back to the baseline.

The explanation given is valid when the assumption is made that both charge carriers have the same mobility. This is, however, not entirely correct. If the difference in mobility is included, both position and type of charge carrier become important and hence will vary this model slightly.

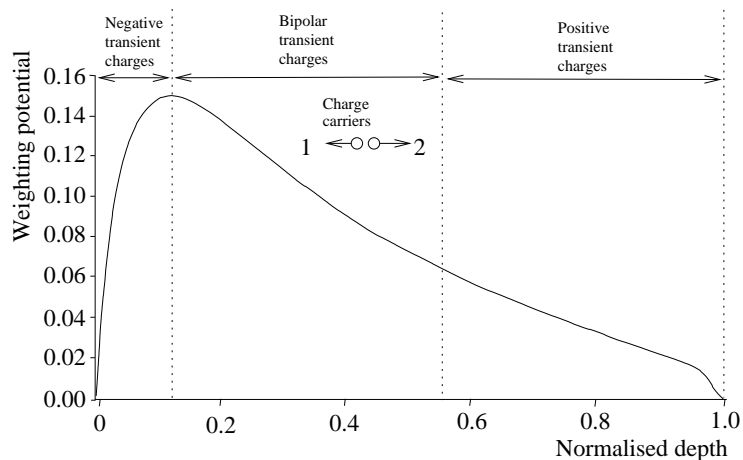


Figure 2.11: The weighting potential for the adjacent strip has been calculated for a detector with a strip pitch to thickness ratio of 1 to 6. Three regions have been pointed out. These regions represent the regions where the positive, bipolar and negative transient charges occur.

2.6.3 Preamplifier response

The preamplifier is present to extract the signal from the detector with a good signal to noise ratio. Germanium detectors are mainly equipped with charge sensitive preamplifiers which provide a good gain stability and a low noise level. The low noise level is achieved by using a Field-Effect Transistor (FET). In conventional germanium detectors, the FETs are placed inside the cryostat (cold FETs) which provide a low noise level and a low level of crosstalk. With segmented germanium detector however, they are normally placed outside the cryostat (warm FETs) because of practical issues. A simplified electronic circuit diagram is shown in figure 2.12. The time constant (τ) of the diagram is equal to $R_f \cdot C_f$. This is

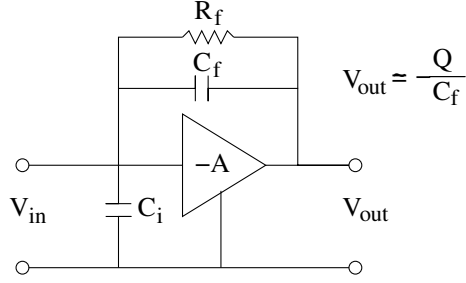


Figure 2.12: A simplified circuit diagram of a charge sensitive preamplifier. [Kno00a]

also known as the decay constant of the preamplifier.

2.7 Detector operational characteristics

The performance of a detector system is related to quality factors. These are the energy resolution, the efficiency and the signal-to-noise ratio. These three can be looked at using either analogue or digital electronics.

2.7.1 Energy resolution

The energy resolution is a measure of the resolving power between two different energies and is normally expressed in the full width at half the maximum height of the photo peak (FWHM). Germanium detectors have the advantage of their excellent energy resolution of $\sim 0.2\%$ FWHM of the photo peak energy. There are three factors of influence on the intrinsic energy resolution which can be added together in quadrature [Kno00b]:

$$\Delta E_{int} = (\Delta E_D)^2 + (\Delta E_X)^2 + (\Delta E_E)^2 \quad (2.17)$$

1. In the ionisation process there is a fluctuation in the number of charge carriers and hence in the energy. The contribution of the fluctuation (ΔE_D) can be described as:

$$\Delta E_D = (2.35)^2 F \epsilon_{pair} E_\gamma \quad (2.18)$$

For an energy of 662 keV the intrinsic fluctuation contributes 0.84 keV to the energy resolution for HPGe detectors.

2. Once the free electrons and holes are created, they are starting to drift towards the contacts. Due the drift process, some of the holes recombine with free electrons, which means that not all the energy is induced. ΔE_X is the broadening which occurs due to incomplete charge collection. This happens mainly in large volume detectors or low electric field regions.
3. ΔE_E is the electronic noise of the detector. The electric noise contribution can be defined as:

$$\Delta E_E = 2.35 \frac{E}{V_{pulse}} V_{rms} \quad (2.19)$$

where E is the energy deposited, V_{pulse} is the pulse amplitude of the output signal and V_{rms} is the root-mean-square of the output signal. [Ort]

2.7.2 Efficiency

The absorption of γ -radiation varies for different materials. The detector efficiency can be quoted in three different ways: absolute, relative, intrinsic and photo peak efficiency [Kno00c].

1. The absolute efficiency is defined as

$$\epsilon_{abs} = \frac{\text{number of detected photons}}{\text{number of emitted photons}} \quad (2.20)$$

The absolute efficiency is dependent on the detector material, detector geometry and distance between detector and source.

2. The relative efficiency is the absolute efficiency compared to a NaI(Tl) detector with a crystal of 76 mm diameter and 76 mm length. The source to detector distance is 25 cm. The relative efficiency is normally measured for an energy of 1.33 MeV.
3. The intrinsic efficiency takes into account the geometry of the detector. It is defined as

$$\epsilon_{int} = \frac{\text{number of detected photons}}{\text{number of photons incident on the detector}} \quad (2.21)$$

4. The photo peak efficiency gives a number which is related to the origin of the detected event. It is defined as:

$$\epsilon_{ph} = PT \times \epsilon_{abs} \quad (2.22)$$

where PT can be found by looking at the energy spectrum. It is the ratio between the number of counts in the photo peak compared with the total number of counts. This efficiency is of importance when a lot of Compton scattering and pair production is present.

Chapter 3

Experimental setup

In order to utilise the SmartPET detectors for imaging, the best possible position resolution inside the detector is looked for. To improve the initial position resolution, a detailed understanding of the performance characteristics is required. To get a better understanding of the detector response measurements have been done. The apparatus and methods for the characterisation are outlined in this chapter including the detector, scanning setup, digital acquisition system and the measurements done.

3.1 The 1st SmartPET detector

This work presents the characterisation of the first SmartPET detector (figure 3.1). It was manufactured by Ametek (Ortec) and delivered in February 2005 to the University of Liverpool.

The SmartPET detector is a double sided germanium strip detector (DSGSD) detector. It has a HPGe crystal of $74 \times 74 \times 20$ mm with an active volume of $60 \times 60 \times 20$ mm. The extra germanium surrounding the active area acts as a guard ring which is present to make the electric field more uniform near the edge of the crystal.

The impurity concentration of the crystal is 5×10^9 atom/cm³. The crystal is grown along the $\langle 100 \rangle$ depth axis which has therefore a $\sim 5\%$ variation in impurity concentration along this axis. The $\langle 100 \rangle$ axis of the crystal lattice is parallel to the short axis of the crystal.

The crystal is electrically segmented into 2 sets of 12 orthogonal strips (see figure 3.2).

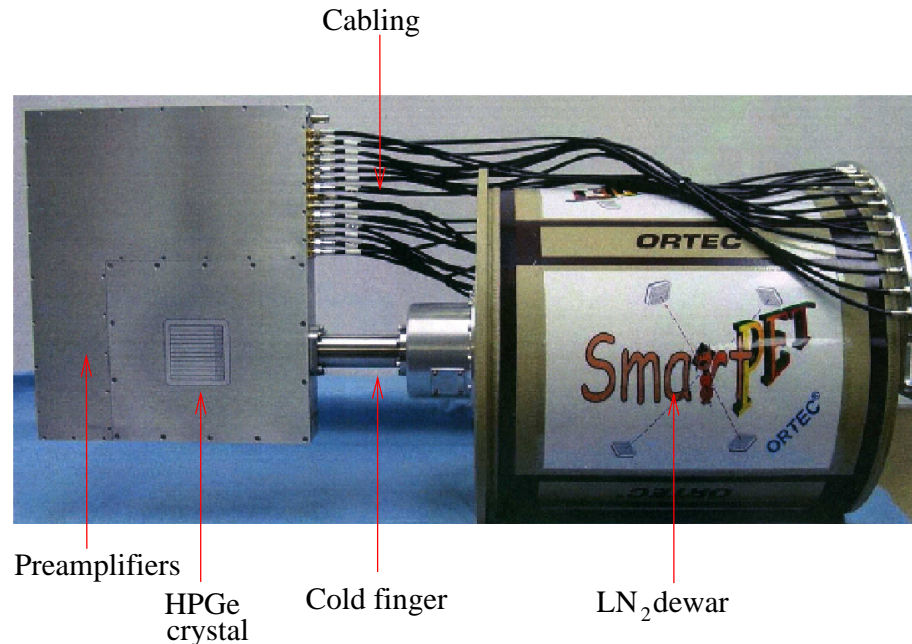


Figure 3.1: The first SmartPET planar germanium detector

Both sides have a strip pitch of 5 mm with an inter strip gap on the AC contact of $180\ \mu\text{m}$ and on the DC contact of $300\ \mu\text{m}$. The depletion voltage of the crystal is $-1300\ \text{V}$. The operational voltage is $-1800\ \text{V}$ and is applied to the AC side. The DC side is grounded. The implanted contacts have a thickness of $0.3\ \mu\text{m}$ and $50\ \mu\text{m}$ on the AC and DC side respectively. The material of contacts is unknown. The AC contacts are implanted blocking contacts. The contacts on the DC-side are labelled DC01 - DC12, on the AC-side AC01 - AC12.

The detector is equipped with a 12 litre LN_2 dewar which keeps the detector cold for 72 hours. It takes ~ 8 hours to cool down or warm up the detector. Every contact is connected to a charge sensitive preamplifier to amplify the signal suitable for further handling. The gain of the preamplifiers is $300\ \text{mV/MeV}$. The rise time of the preamplifier is 30 ns defined from 10% to 90% of the pulse magnitude.

3.2 Scanning setup

In order to achieve a good understanding of the detector response for interactions at different positions. A collimated source of known energy which can be moved along the crystal is

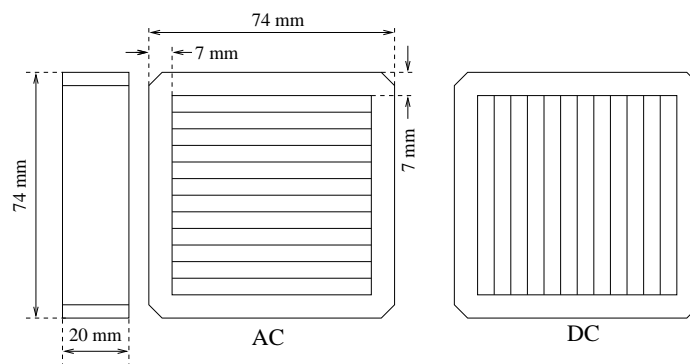


Figure 3.2: The dimension of the HPGe crystal showing the orthogonal segmentation on both sides of the detector

required. For this purpose, a scanning apparatus shown in figure 3.3a has been assembled. The radioactive source is placed in the middle of a lead assembly. To ensure the detector is shielded sufficiently from the source, 17 cm of lead has been placed in between the detector and the source. The lead, source and collimator are sitting on top of a x-y positioning table. The positioning table is driven by two stepper motors which positions the table with an precision of $100\ \mu\text{m}$. The response of the detector has to be investigated for 662 keV γ -rays. The source used for the main measurements is a 70.2 MBq ^{137}Cs source. The full energy count rate out of the collimator is measured with a NaI to be 35 cps.

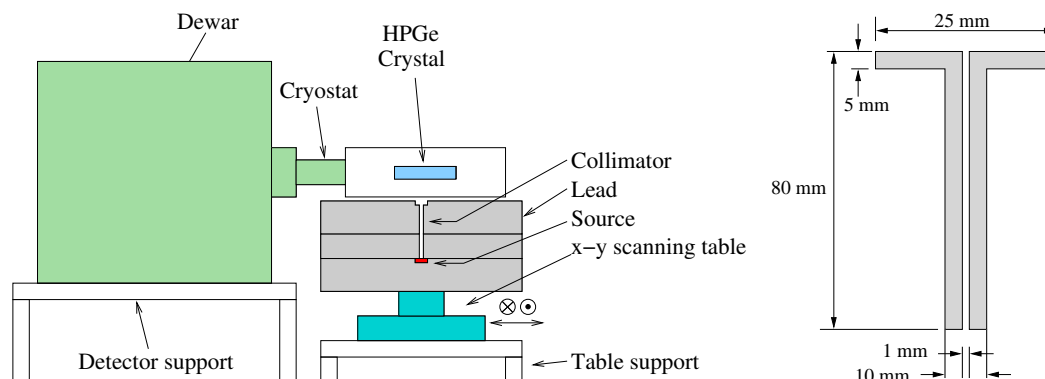


Figure 3.3: The scanning setup with the detector positioned for the front face scan (left). The 1 mm diameter Tungsten collimator is drawn schematically on the right. The collimator is mounted inside the lead.

3.3 Data acquisition system

The requirement to analyse the shape of the pulses produced by the charge sensitive preamplifiers in combination with the high count rate requires the use of a digital electronic system. The DAQ system is based on 7 VME GRT4 modules manufactured by Daresbury Laboratory [Laz04]. These cards have a sampling rate of 80 MHz over a 14 bit dynamic range. Each card has 4 channels, with one FPGA for each channel. Eventually these can be programmed with different algorithms which can provide the x, y and z coordinates of the interaction position in real time. The GRT4 modules are currently programmed with the moving window deconvolution (MWD) algorithm [Geo93] to provide a measurement of energy with good resolution to provide an improved energy resolution (see appendix A).

3.4 Trigger

The GRT4 cards are triggered externally using the DC signals. Figure 3.4 shows the electronic setup providing the trigger:

1. The AC-side signals are going straight from the detector into the GRT4 cards.
2. The DC-side signals get split; one side is going into the GRT4 cards, the other side is fed into the input of the timing filter amplifiers (TFA). The TFA's will amplify the signal preserving the fast leading edge of the signal.
3. After the TFA, the signals are fed into the constant fraction discriminators (CFD). The CFD's have a 20 ns constant fraction delay. The CFD threshold is set to ~ 50 keV. These provide a logic output signal whenever this threshold is exceeded.
4. The outputs of the CFD's provide 12 logical signals. The system triggers when at least one of the CFD's fires (i.e. one of the DC signals has an energy over ~ 50 keV). The presence of at least one of the CFD trigger is checked in a logical *OR* unit.
5. The read out of the system takes a finite amount of time. During this time, the system should not receive any triggers. If the system is busy with the data read out, the inhibit or busy signal present on the GRT4 cards is set. If there has been an event in the system and the *OR* unit provides a signal, a check is carried out to see if

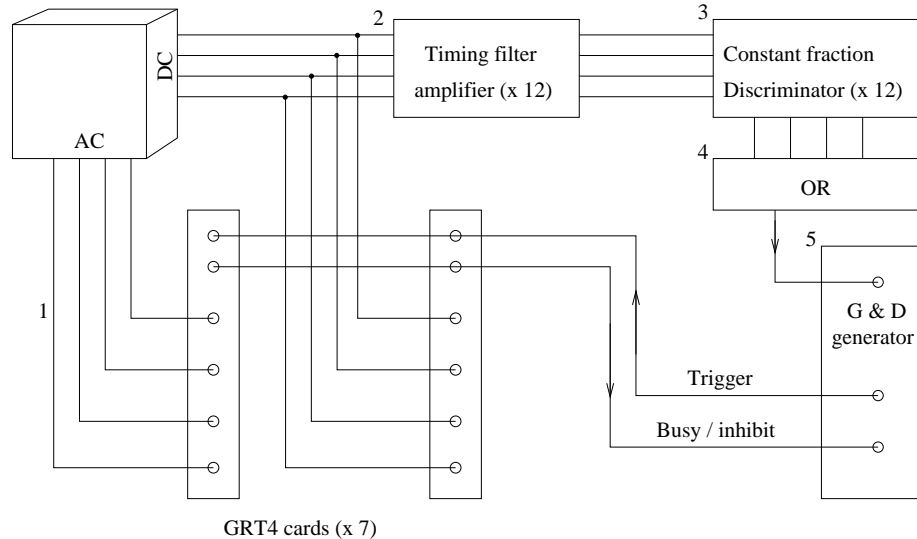


Figure 3.4: The DC signal is used as the trigger of the data acquisition. The system gets triggered if an energy deposition of > 50 keV is measured.

the system is ready for data collection. If the system is ready to collect the data, the gate-and-delay unit provides the trigger of the setup. Whenever the GRT4 cards are triggered the inhibit signal is set until the system is finished with the read out.

Once the system is triggered, all 24 strips and the guard ring are read out and stored to SDLT tape. Each signal consists of $3.2 \mu\text{s}$ (256 samples) of data starting $\sim 1.6 \mu\text{s}$ before the start of the pulse.

3.5 Scanning methods

The initial position resolution using the strip width and detector depth is $5 \times 5 \times 20$ mm. To attain the best possible position resolution, it has to be improved in all three dimensions (i.e. two lateral and one depth). The measurements are taken so all dimensions can be improved. The detector signal should be characterised for different interaction positions which is defined by the 1 mm collimator. The collimated beam of γ -rays can be injected into the crystal either from the front face or from the side. A front face characterisation provide the response in two lateral positions and no depth information. The side scan provides the lateral position on the AC side and depth response. By combining the two

scans, the detector can be characterised in 3 dimensions.

The following parameters are used for the scans:

1. The collimator is 3 mm away from aluminium can in the side scan setup which makes it 65 mm away from the edge of the crystal. The collimator used is a 1 mm diameter tungsten collimator with a length of 8 cm (see figure 3.3b). MCNP simulations [MCN] of the germanium crystal have been done to characterise the divergence of the injected beam of photons. The photons are injected through the side of the crystal. The diameter is ~ 1.3 mm in the middle of the crystal. The scan is done over an area of 63×30 mm starting outside of the active area of the crystal. The step size has been chosen to be 1 mm. The table stopped at each position for 120 seconds. A total data was 394 Gb.
2. The front face scan is used to get the lateral response of the detector. The collimator is moving across the front face of the crystal. The distance between collimator and aluminium can is 3 mm. The distance to the crystal is ~ 16 mm. The divergence over this distance is neglectable. The scan is done over an area of 61×62 mm. The step size is 1 mm. The system was collecting data for 120 seconds at each position. The total data set was 920 Gb.

The results presented in this work are from both scans. In these scans, there is a difference made between the AC and DC signals used. For clarity most of the figures have been equipped with one of five different schematics. These drawings represent the type of scan used (i.e. side scan or front face scan) and the signals (AC / DC or both sides) used for the graph. In table 3.1 all the different figures are explained.

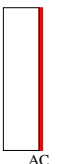

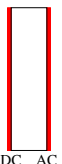
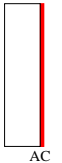

Side scan AC side	Side scan DC side	Side scan Both sides
<p>Collimated Source ○</p>  <p>AC signals</p>	<p>Collimated Source ○</p>  <p>DC signals</p>	<p>Collimated Source ○</p>  <p>DC AC signals</p>
Front face scan AC side	Front face scan DC side	
<p>Collimated Source ○</p>  <p>AC signals</p>	<p>Collimated Source ○</p>  <p>DC signals</p>	

Table 3.1: The different symbols used as a description for the various scans of the detector described later.

Chapter 4

Basic detector characteristics

The detector analysis is split up into two parts: a general analysis and the pulse shape analysis. The general analysis, presented in this chapter, involves a basic noise evaluation, preamplifier response, full energy sensitivity, simple scattering behaviour of 662 keV γ -rays, energy resolution and cross-talk.

The improvement of the position resolution using pulse shape analysis will be presented in chapter 5.

4.1 Signal characterisation

The basic signal characteristics are defined by 4 parameters: baseline offset, noise level, amplification and preamplifiers response. These parameters are important to be able to extract the detector response as well as possible.

4.1.1 Baseline offset and noise level

The baseline offsets are measured for all the strips. The detector signals are measured on a *HP Infinium* oscilloscope with a 1 M Ω input impedance. The baseline offsets are shown in table 4.1. DC11 shows a particular low DC offset of 5.0 mV. The average offsets on the AC and DC side are 38.3 mV and 15.3 mV respectively.

The peak-to-peak noise level for each channel is identified and included in table 4.1. None of the strips show a major variation from the others. The average noise level is 7.1 mV (6.8 - 7.5 mV) for the AC-side and 6.7 mV (6.2 - 7.3 mV) for the DC-side.

Strip	Offset (mV)	Noise level (mV)	Strip	Offset (mV)	Noise level (mV)
DC01	13.7	6.9	AC01	33.0	7.3
DC02	30.1	6.5	AC02	46.7	7.0
DC03	12.1	6.2	AC03	39.4	7.2
DC04	17.5	6.3	AC04	35.4	6.8
DC05	20.1	7.2	AC05	37.6	6.9
DC06	16.0	6.8	AC06	33.5	6.9
DC07	10.8	6.6	AC07	45.0	7.0
DC08	16.4	6.3	AC08	41.8	7.2
DC09	14.6	6.6	AC09	28.9	7.0
DC10	14.1	7.3	AC10	33.0	7.5
DC11	5.0	7.0	AC11	45.0	7.2
DC12	13.1	6.4	AC12	40.1	7.1

Table 4.1: The preamplifier baseline offset and peak-to-peak noise level for each of the strips

4.1.2 Preamplifiers

The detector is equipped with 24 preamplifiers. The response of the preamplifiers is convolved within the output signals. There are two test inputs present to test the preamplifier response. The two test inputs are connected to the preamplifiers of DC06 and AC07. Both preamplifiers are tested by using a step function generated by a pulse generator. The rise time (i.e. the time between 10% - 90% of the pulse magnitude) of the step function is 5.0 ns with an amplitude of 100 mV. The rise time of the detector output is measured to be 69.2 ns for the DC side and 67.2 ns for the AC side. The decay constant is measured to be 43 μ s for both sides of the detector.

4.2 Intensity map

Two scans are performed to investigate the detector response to single interactions for different positions (see section 3.2). The following gates are used on the data:

1. the energy falls in between 650 and 670 keV measured on both sides of the detector

2. the number of real charges, i.e. multiplicity, for each side is 1. The multiplicity of an event is defined as the number of real charge with an energy of over 25 keV recorded. This threshold is set in the software.

The two surface scans are investigated with these gates. The number of valid events per position are incremented in an intensity map (see figure 4.1 and 4.2).

4.2.1 The side scan

The active area of the crystal is identified by the increased number of accepted events in figure 4.1. The background counts outside the active area are mainly due to insufficient lead shielding. The background counts compared to the counts in the active area has the ratio $\sim 1:6$. The average number of counts per depth is between ~ 2000 near the edges and ~ 7000 counts in the middle of the crystal.

The crystal is positioned so that the DC contacts are at the bottom of the active area and the AC contacts at the top of the active area. There is an offset in both x and y position before the crystal active area is reached. For the rest of the work, a relative coordinate system is used starting at the coordinates (3,1). Any depth (i.e. increasing y position) is measured relative to this point so that the DC contacts are at depth 0 mm and the AC contact at depth 20 mm.

The AC strips are clearly visible due to the lower intensity in between the strips. There are two reasons for the lower intensity, which will split the energy between two strips.

- Charge sharing due to the finite size of the electron cloud. Whenever a γ -ray interacts close to the boundary, the created electron cloud is likely to overlap into the adjacent strip. This causes two strips to share the energy. For more information about charge sharing see [Kro99].
- Compton scattering into the next strip. When the γ -ray interacts with a Compton scatter, it can scatter towards the adjacent strip. Whether the secondary γ -ray interacts within the strip where the first interaction took place or in the adjacent strip is dependent on the distance between the first interaction and the strips boundary.

In both cases, the gates for a valid event are not met and hence these events will be excluded for the intensity maps. The intensity in between each of the strips is $\sim 30\%$ of the intensity

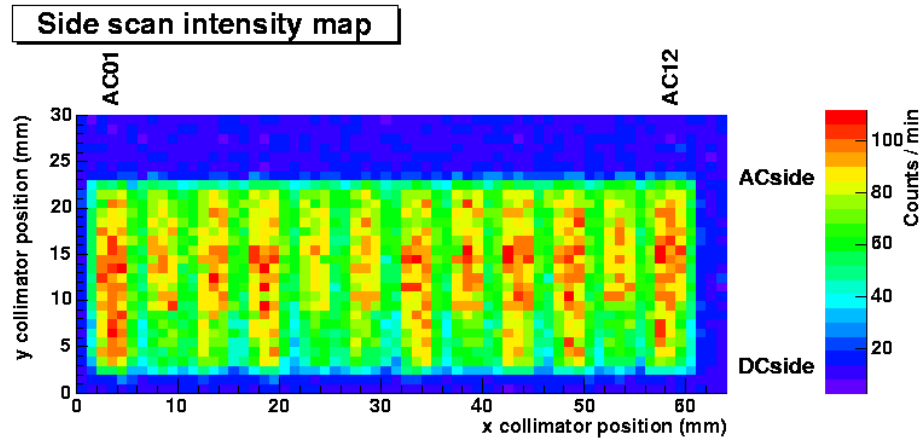


Figure 4.1: An intensity map has been made using the side scan data. The design of the detector only allows the AC strips to be visible.

region inside each strip. Both effects together cause a region of 2 mm (i.e. two line in the scan) with lower intensity in between two strips.

The DC strips are not visible in the intensity map of the side scan due to the crystal orientation. The DC strip boundaries are perpendicular to the collimated beam.

4.2.2 The front face scan

The front face scan data is used to create another intensity map (figure 4.2) in the same way as the side scan. The ratio of background to active area is the similar to the side scan ($\sim 1:6$). The geometrical orientation of the crystal allows the investigation of both AC and DC strips: AC strips are orientated vertically, DC strips are orientated horizontally. The lower intensity at the top of the active area (crossing of AC09 and DC01) is caused accidentally by a temporarily disabled channel (AC09) in the data acquisition system during the measurement.

Four different regions of intensities can be identified within the active area:

1. The full intensity where the collimator is underneath the middle region of two crossing strips.
2. Single energy splitting between two strips (a decrease of $\sim 30\%$ of the full number of counts)

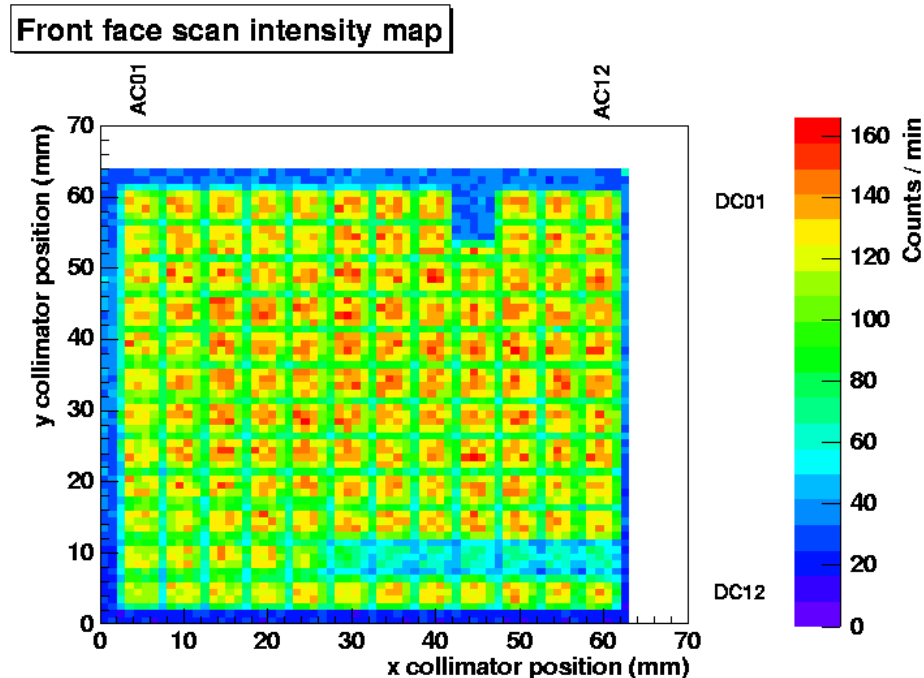


Figure 4.2: An intensity map has been made using the front face scan data. Both AC and DC strips are clearly visible.

3. Double energy splitting at the crossings between four strips (a decrease of $\sim 50\%$ of the full number of counts)
4. An intensity gradient across DC11 is observed due to charge sharing.¹ This will be discussed later on in this chapter.

4.3 Multiplicity for 662 keV γ -rays

The data of interest defined by the gates have only 1 real charge on each side of the detector. Figure 4.3 shows the multiplicity for the side scan configuration. The data is analysed with the previous declared energy gate. For interactions in more than one strip, the energy is added together. The AC and DC side are investigated independently.

The most probable multiplicity for both sides is 2. By only using multiplicity 1 data

¹Note the difference in definition of charge sharing. The charge sharing previous discussed is due to the size of the electron cloud where DC11 is suffering from a defect in the contact.

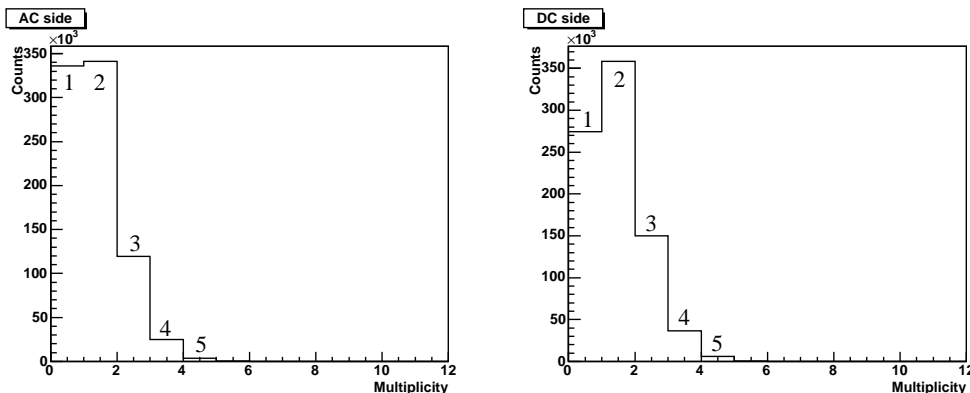


Figure 4.3: The multiplicity has been investigated for both the AC and DC sides separately. A total energy deposition of 662 keV was required defined by an energy gate of 650-670 keV.

40.1 % of the AC side and 33.2 % of the DC side data is useful. The difference in multiplicity between the AC and DC side can be explained by the charge sharing of DC11.

It is ~ 30 times more likely for an 662 keV γ -ray to interact with a Compton scatter than it is being photoelectric absorbed (see figure 2.1). Although the figures show a difference between multiplicity 1 and 2 interactions, the difference is not as large as expected. If a Compton scattering happens, there is a relatively large chance it gets absorbed within the same pixel. This causes the multiplicity to be 1 where there are two scatters present. The difference between these two events can not be distinguished and hence will be classified as a M1 event. These types of events will be referred to as multiple interaction events.

4.4 Energy resolution and charge collection

The FWHM of the 122 keV photo peak is measured for each of the strips using analogue electronics. The results are shown in figure 4.4. The energy resolution of the edge strips is suffering from the weaker electric field near the edge of the crystal. DC11 has an exceptional bad energy resolution (4.1 keV) compared with the rest of the strips due to charge sharing. The average energy resolution, excluding the edge strips and DC11, is 1.4 keV for the AC side and 1.3 keV for the DC side.

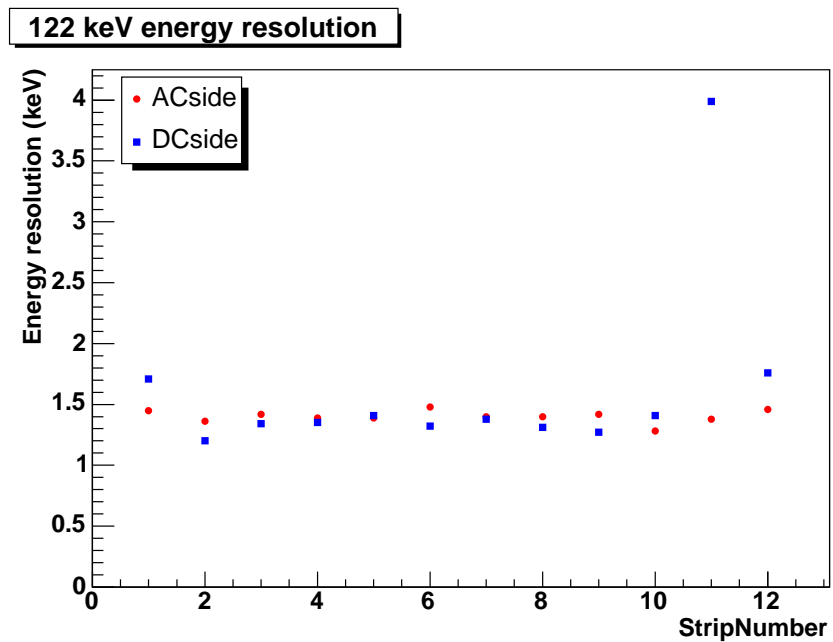


Figure 4.4: The energy resolutions for the strips on the AC and DC side measured with conventional analogue electronics. The shaping time was set to $6 \mu\text{s}$.

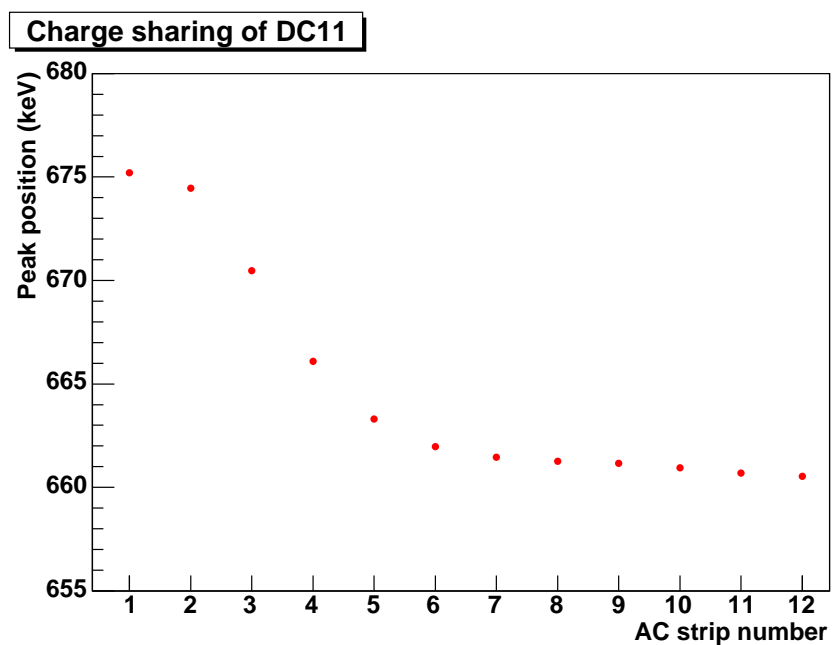


Figure 4.5: The charge sharing of DC11 has been investigated. The photo peak energy of DC11 varies when an interaction is required in one of the AC strips.

4.4.1 The charge sharing of DC11

The energy of the photo peak of DC11 has been investigated for different parts across the strip. This is done by gating on each of the 12 AC strips using the front face scan so that the interactions are happening in different parts across DC11. The peak position for different AC strips shows an energy shift (figure 4.5). The charge sharing is becoming worse from one side to the other side of the strip.

When the energy calibration was done, the peak was taken with the most charge shared with the neighbouring strips (i.e. the peak with the highest intensity). However, the actual full energy with the least amount of charge sharing has ~ 15 keV more than the calibrated energy.

DC11 is excluded from any analysis in the rest of this work.

4.4.2 Depth depending charge collection

The energy resolution is investigated through the depth of the crystal using the side scan data. The moving window deconvolution method is used to extract the energy from the signals. The FWHM and the full energy peak position are shown in figure 4.6 for AC06 and DC06. The comparison between the two sides should be concentrated on the trend rather than the absolute energy which is related to the energy calibration.

The energy resolution is degrading for both sides with an increase of depth. The AC side is increases by ~ 0.75 keV and the DC side by ~ 1.75 keV. The energy resolution of the DC signal becomes particularly bad ~ 4 mm away from the opposite, AC, contact. This behaviour appears together with a decrease of the total energy collection / peak position. Although the energy resolution shows an increase of resolution from this point, the peak position shows more detail about the trend for different depths. Hence the peak position is discussed rather than the energy resolution.

The behaviour of the peak position can be divided into three different regions:

- Close to the DC contact (1 - 4 mm): both AC and DC signal show a similar trend in this region.
- The middle part of the detector (4 - 14.5 mm): both the AC and DC signals show a similar energy loss through depth. The AC signal shows a slight increase after 13 mm.

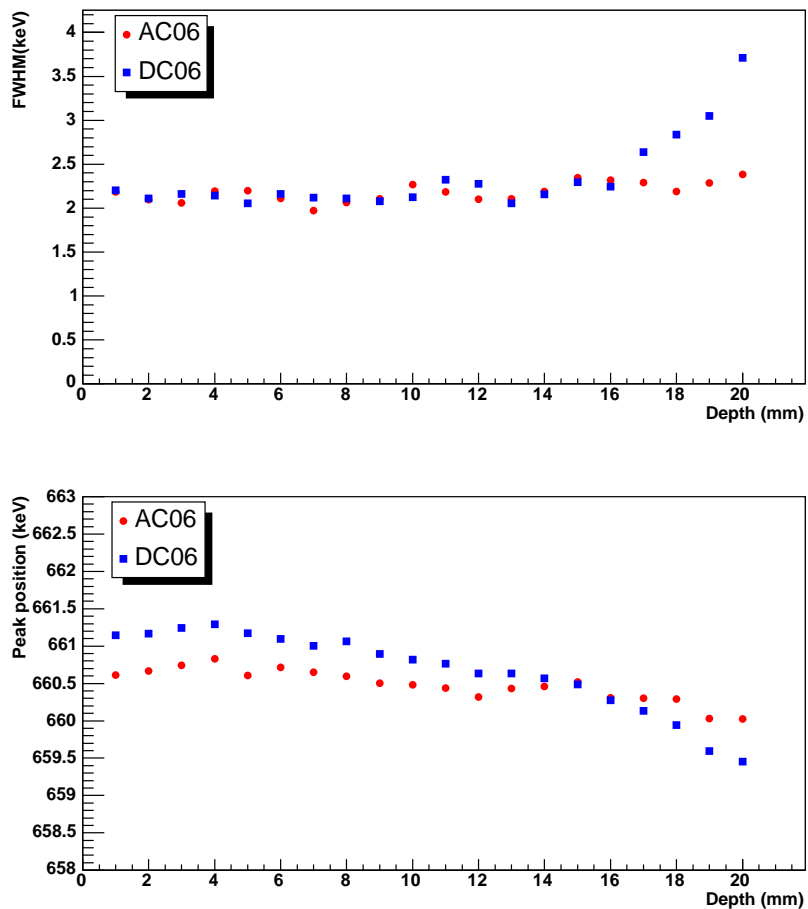


Figure 4.6: The energy resolution of the DC signals is degrading ~ 4 mm from the AC contacts (top). From this point the collected energy, expressed as the peak position, shows a stronger decrease. The AC signals do not show a significant change in position or resolution.

- Close to the AC contact (14.5 - 20 mm): after the energy is increased on the AC side, the energy continues with the same downward trend as in the middle part of the detector. The collected energy of the DC signal in this part is decreasing. It is this region where the resolution is getting worse as well.

The reason for this behaviour is unknown. It could be explained by one or a combination of the following reasons:

- The impurity concentration varies $\lesssim 5\%$ with depth. This could cause a region which is less overdepleted towards one side of the detector. The drift velocities could be affected by this and hence will have an effect on the induced charge.
- Although hyper pure germanium does not suffer a lot from hole trapping, it is still possible that holes are being trapped inside the crystal lattice. The energy resolution and the total energy induced will be affected. This would explain the downward trend towards the AC contact for both signals.
- The sudden energy loss toward one side of the detector could be related to the small electrode effect. In section 2.6 has been explained how the induced current/charge varies with depth. The contribution of the electrons 15 mm away from the contact is possibly not significant enough to induce charge. Due to the difference in interstrip gapsize, the DC side ($300\ \mu\text{m}$) should be suffering more than the AC side ($180\ \mu\text{m}$).

4.5 Efficiency

The efficiency of the detector has been measured. A $0.034\ \text{MBq}\ ^{133}\text{Ba}$ was placed at 25 cm distance from the front face of the detector. The measurement has been done separately for each side of the detector. In the both measurements, the source was placed on the measured side so the efficiency does not get affected due to the differences in charge collection. The measurement was done in ~ 5 hours for the AC side and ~ 15 hours for the DC side.

The results are shown in figure 4.7. The efficiency curve shows a different behaviour between the AC and the DC side. The efficiency of the AC side drops considerably at low energy to $1 \times 10^{-3}\%$ where the DC side stays at an efficiency of $5 \times 10^{-2}\%$.

The reason for the different behaviour can be explained by the contact thickness of each

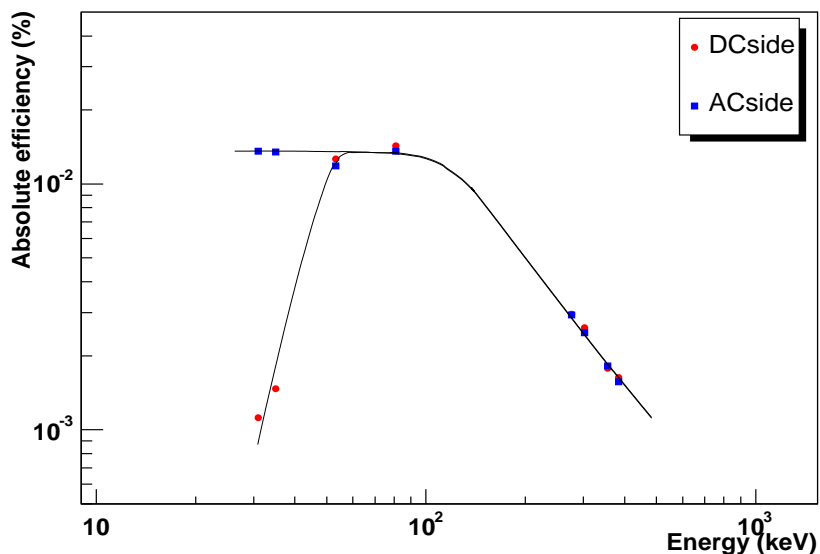


Figure 4.7: The absolute efficiency for the two different size contacts (AC: $0.3 \mu\text{m}$ thick, DC: $50 \mu\text{m}$ thick). The lines drawn are indicating the trend of the efficiency for each side.

side. The AC side has a contact thickness of the $0.3 \mu\text{m}$ which will have less low energy absorption inside the contact. The DC side has a contact thickness of $50 \mu\text{m}$ which will show more low energy absorption. Hence the position of the source will affect the efficiency as the results show.

4.6 Cross-talk

Cross-talk is the undesired coupling between two or more electronic circuits. In HPGe detectors, the main cross-talk is between pairs of the electrodes. Cross-talk between strips becomes apparent when the energy of two or more strips is added together: an add back spectrum. By adding together the separate energies for M2 and M3 events, the full energy photo peak can be reconstructed. In an add back spectrum from a detector suffering from cross-talk, the photo peak occurs at a higher energy than the single interaction (M1) energy. The shift in peak position for the AC and DC side is clearly shown in the two spectra on the left of figure 4.8. The shift in the peak position effects the AC side by $\sim 6 \text{ keV}$ ($\sim 0.9 \%$) and the DC side by $\sim 1 \text{ keV}$ ($\sim 0.2 \%$).

The adjacent strips are investigated for M1 events. Although these strips should not have any energy, there is always a baseline shift present after the transient charge. It is more pronounced for the AC side than for the DC side. The loss in energy due to cross-talk appears in the adjacent strips.

By summing the separate energies using higher multiplicity events (M2 and M3), the peak shifts further away from the M1 peak position in the add back spectrum. This indicates that the number of scatters is affecting the amount of cross-talk. In case of a single multiplicity, there is only one strip with a relatively high energy in it. When one of the higher multiplicity is considered, the energy is split between two or more strips. The distance between the scatters becomes smaller due to the lower energy of each component. Therefore it is likely for a higher multiplicity to have two real charges in adjacent strips. If the cross-talk is assumed to happen between two adjacent strips, higher multiplicity should not be affected by it as much as M1 events. The cross-talk would not be noticed because it is automatically included on top of the major energy deposition in the adjacent strip. In other words, the higher the multiplicity, the less the energy gets affected by the cross-talk. This is consistent with the peak positions in the figures.

The photo peak of M2 (and M3 photo peak to some extent) interaction shows a double peak indicated by the arrows. The peak with more energy is due to interactions happening in adjacent strips, so less energy is lost. The lower (less intense peak) represents the interactions two strips away from each other. In these events, the crosstalk present in the middle of the two strips and not automatically be compensated.

The correction for cross-talk can be done by adding back all the energies including the energies in the adjacent strip. When this is done for multiplicity 1, 2 and 3, the corrected spectra on the left side of figure 4.8 were found. The spread of the maximum channel of the full energy peaks for different multiplicities is within 1 keV for the AC side and within 0.4 keV for the DC side.

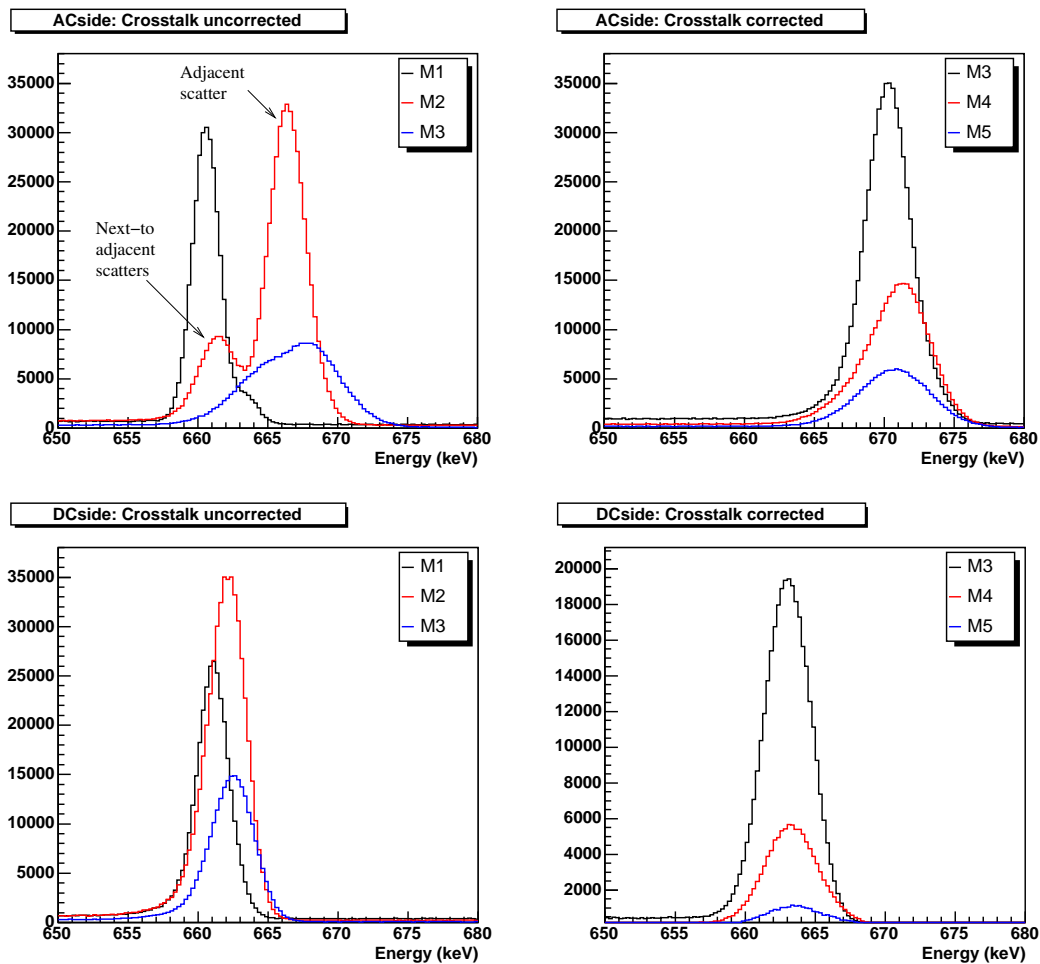


Figure 4.8: The cross-talk behaviour for the AC and DC side. The cross talk can be corrected by adding back the much smaller (~ 5 keV) baseline difference from the adjacent strips. The different lines represent different multiplicity events (i.e. M1 equals multiplicity 1, etc)

Chapter 5

The signal analysis of the SmartPET detector

This chapter contains the investigation and discussion of the signal response of the detector. The analysis of the response leads to a better understanding of the detector. Once a better understanding is obtained, this then can be applied to improve the position resolution.

This chapter has been set up in a way that every step of the process is discussed. The chapter starts by showing the six signals of an event as an example.

To extract the information from the signals, a parameterisation method is developed for the different types of signals. The chosen parameterisation is applied to the data, which gives several different distributions. These distributions can be split up into different responses in the 3 dimensions of the crystal using different scans. After a rough presentation of the response, a calibration has been investigated in these 3 dimensions. This calibration is then applied to the data to determine the performance of the system.

Each of these steps is split up into two parts for the two types of signals. These will be discussed in parallel.

5.1 The concept of Pulse Shape Analysis

The improvement in the position resolution of the detector is based on a technique called pulse shape analysis (PSA). The technique uses two different types of signals: real charge and transient charge signals. Both types of signal hold information about the interaction

position in their shape. PSA is used to determine the differences in detector response for each position throughout the detector.

5.1.1 The parameterisation of real charges

The data acquisition system samples the signal at a frequency of 80 MHz. The rising edge has a typical range in rise time of ~ 100 -300 ns which is covered by 8-24 samples. To increase the number of samples and hence the depth accuracy, the data have been linearly interpolated by 4 points and smoothed by a 5 point running average. An example of a 662 keV M11 event is shown in the real charges of figure 5.1. The red dots represent the raw data sampled at time intervals of 12.5 ns. The blue dots are 4 point interpolation points between these data points. The interpolated pulse shape has one sample every 2.5 ns which provides a more accurate rise time and hence depth extraction.

The AC real charge in the figure shows a number of ways to extract the rise time of the pulse shape. In the notation $T_{a,b}$, (a) is the starting point and (b) is the end point of the rise time. Several combinations of beginning and end points can be chosen. The time it takes for a pulse shape to get from 10 % to 30 %, 60 % and 90 % of the final magnitude will be written as $T_{10,30}$, $T_{10,60}$ and $T_{10,90}$ to define the range over which they are measured.

5.1.2 The parameterisation of transient charge

The example in figure 5.1 includes four transient charges associated with their two real charges. The parameter used for the transient charges is the net area which is indicated as the red area in the figures. This provides a range of values from positive to negative where positive is defined as the area above the baseline and negative below the baseline. The advantage of using the area is a smoother depth dependence and smaller fluctuations due to the larger number of samples being used.

5.2 The detector response - rise time, transient charge area

The data set of the side scan is used to investigate the general response of the detector using the method described in the previous section. The use of the rise time of the real charge is initially investigated for depth dependence. Once this is known the depth dependence of

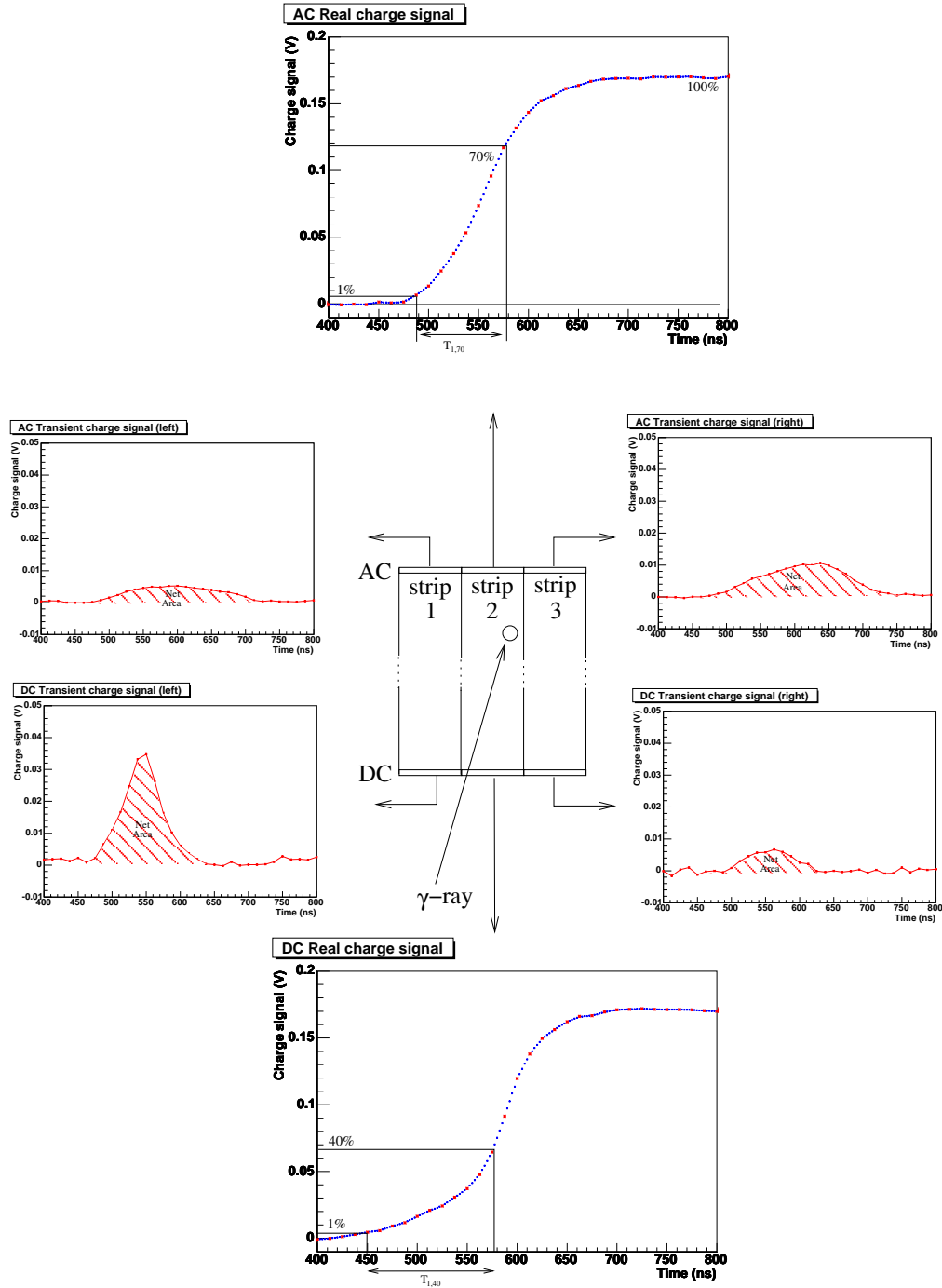


Figure 5.1: An example of a 662 keV M11 event is shown. 6 signals are of interest: 2 real charges and 4 image charges. The DC contacts are rotated for schematic purposes. The figures of the real charges include the three risetime parameterisation of the pulse shape: $T_{10,30}$, $T_{10,60}$ and $T_{10,90}$. The proposed parameterisation of the transient charges is shown by the shaded area underneath the 4 signals.

the transient charge shape is discussed.

5.2.1 Rise time plots

A common way of describing the rise time of a 662 keV pulse shape is by using the $T_{10,30}$, $T_{10,60}$ and $T_{10,90}$ parameter. The rise time distributions for the DC and AC side are shown in figure 5.2.

The range of the $T_{10,90}$ rise time distributions on the AC side is spread out between ~ 100 and 240 ns. The DC side shows a faster response which is in between ~ 100 and 150 ns. All distributions show a peak at the higher and lower end of the distribution as the arrows indicate. The peaks on the higher end in the DC signals are not as pronounced. The peak at the lower end is generally narrower than the one at the higher end. The cause of these peaks will be discussed later.

5.2.2 Transient charge areas

The transient charges can be used to define the lateral interaction position within the strip. The method investigated uses the difference between the two transient charges either side of the real charge. The transient charge areas of the two neighbouring strips are therefore investigated in relation to each other. Two graphs in figure 5.3 show the transient response of the AC and DC sides. There are two lines drawn within the plot: one is the polarity axis and the other one is the asymmetry axis. The polarity axis is drawn at the position where the transient charges have no net area (i.e. bipolar region).

The total number of counts on the right side of the polarity axis is much larger than on the left side indicating a larger number of positive transient charges. The AC side has a much larger overall asymmetry than the DC side. The asymmetry is the largest for positive transient charge with a large area. The number of counts, indicated by the colour scale, is much more spread out for the DC side where as the AC side is more localised.

5.3 Filtering method

The evaluation of the rise time as a function of depth requires an average pulse shape to find the best parameterisation. When the average pulse shape is calculated over the complete

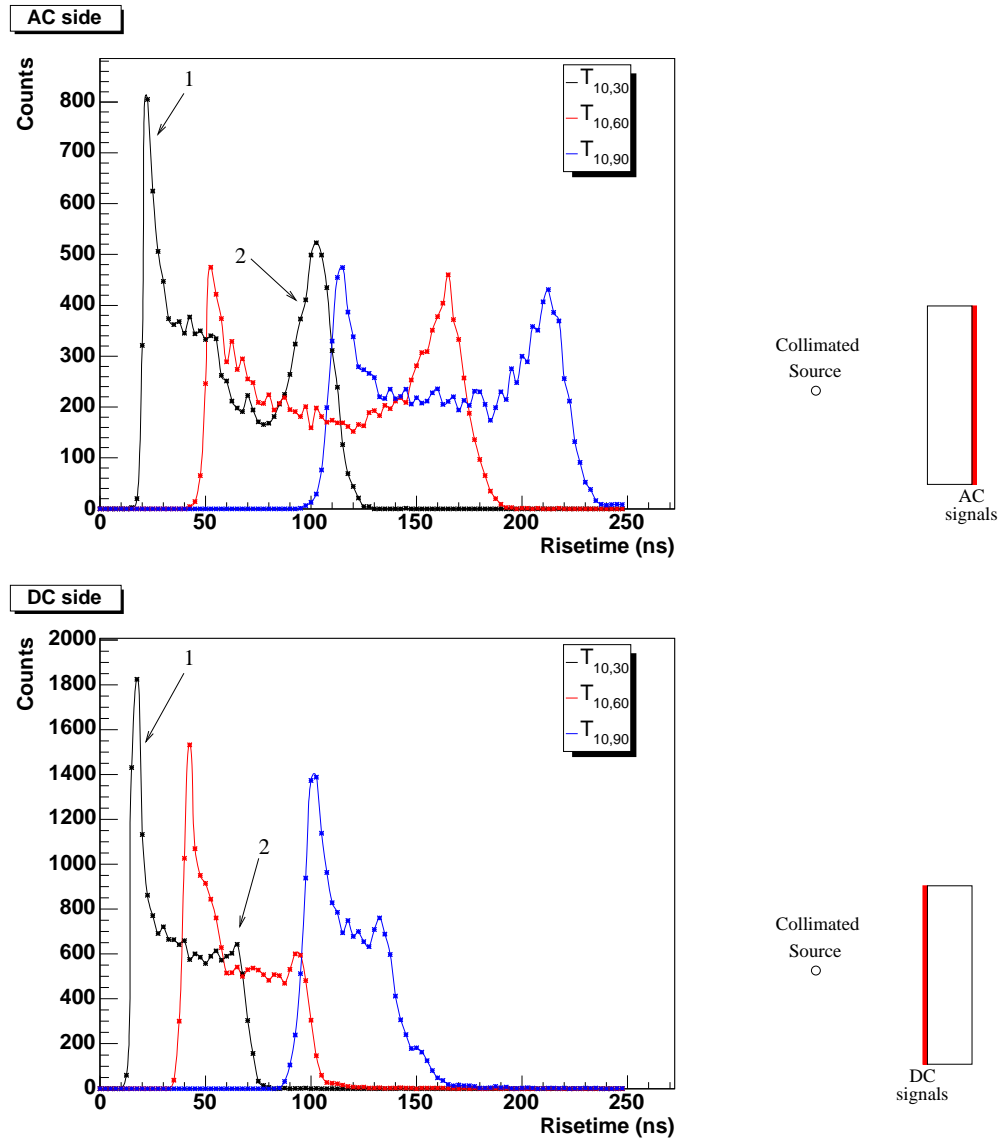


Figure 5.2: Rise time distribution for the AC and DC side. The arrows are indicating the peaks at the start and end of the $T_{10,30}$ distributions. The peaks are an indication of a non-linear behaviour towards the edges of the detector discussed in section 5.4.1. The fastest peak (1) is due to only one charge carrier inducing the charge inside the detector. The slower peak (2) is caused by the starting point (T_{10}) of the risetime parameter.

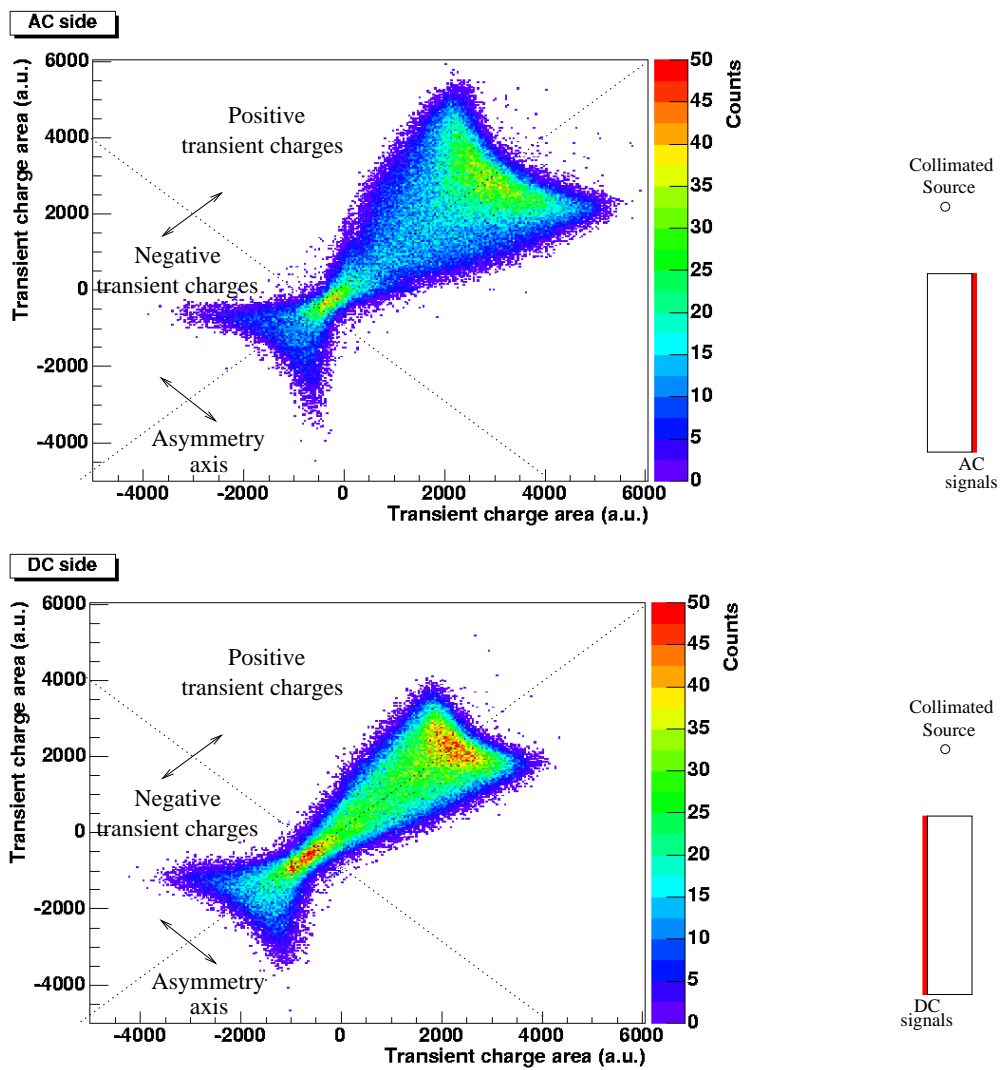


Figure 5.3: The area of the transient charges from either side of the real charge are plotted against each other for both sides. Two lines are drawn in the figures which show the asymmetry and the polarity of the transient charges.

data set, it is built out of 3 types of interactions event:

1. Single (PE) interactions: these are the interactions of interest and are the pulse shapes of interest to provide the response for each depth.
2. Multiple (CS) interactions: these interactions are the most difficult to separate from the single interactions. The place of the interaction and the energy involved vary for each of the scatters. Each of these parameters can be small which makes the detector response similar to a single interaction. Using 662 keV γ -rays, most of the multiple interactions will scatter forwards ($\theta \lesssim 45^\circ$, see figure 2.3) and therefore using the side scan setup, the second interaction point will not vary much in depth and hence the pulse shape will not be affected much.
3. Random interactions: these interactions are caused by γ -rays penetrating the lead shielding and interacting at random positions within the detector. These types of interactions are known as background events have nothing in common with the single interactions.

The proportion falling in these categories is important. A 662 keV γ -ray is more likely to have a Compton scatter event rather than a photoelectric event. MCNP simulations of the side scan setup have been carried out to study the behaviour of the γ -ray within a single pixel (i.e. strip crossing). Special interest went out to the scattering distance. The results of the simulations show that out of all full energy events within a single pixel, 80% are CS events. The pulse shapes produced by CS events are convolved shapes from the each individual interaction. The separation of these pulse shapes will not be included in this work. It is sufficient to know that CS events generate signals which are based on the energy deposited at each position, scattering distance and scattering angle between each of the scatters. The convolved pulse shape will differ from the single interaction for most of the CS events.

To get a feeling for the number of random events in the data, the intensity maps can be used. As mentioned before, the ratio between random (background) and collimated events is $\sim 1:6$ (see section 4.2). This ratio describes the difference between the random interactions and the single interactions.

The first step in the characterisation is to reduce the effect of the two unwanted inter-

action types (2 and 3). Normally this is done by using a coincidence technique between the germanium detector and the NaI detector [Mil05]. Although the data acquired with this technique is of high quality, this method takes a very long time to get good enough statistics to produce a good average. For this work another approach has been made using the data from the side scan.

A filtering method has been developed to extract the most probable pulse shape for each depth of the side scan which corresponds to the single interaction. The data have been selected by the gates stated in section 4.2. The working of the method is explained along the schematic in figure 5.4:

1. Factors which adversely influence on the total pulse shape should be eliminated before the filtering method. Therefore each individual pulse shape should be lined up at one point (i.e 10 % of the final amplitude) for any time misalignment. For a good alignment it is necessary to use the interpolated pulse shapes. The pulse shapes should all have the same height. Although the selected pulses have the full energy, there is still an energy spread due to the resolution ($\text{FWHM} \simeq 2 \text{ keV}$) which makes the pulse shape have a different shape. To eliminate the difference, the pulses are all stretched to the same height. In this case the heights of the pulse shapes are normalised to a 1000.
2. The average pulse shape is calculated by averaging a number of individual pulse shapes. Depending on the depth, the initial number of pulse shapes used varies between 2000 and 7000.
3. Each individual pulse shape is then compared with the average pulse shape. The deviation calculated by using the sum of squares. The pulse shape with the highest sum of squares will be very different from the average pulse shape.
4. The average pulse shape is calculated again excluding the pulse shape with the highest sum of squares.
5. This procedure is continued until 50 pulse shapes are remaining. This number is chosen to conserve a low noise level for a good determination of the rise time. The average is taken of these pulse shapes. This represents the most probable pulse shapes in the data set.

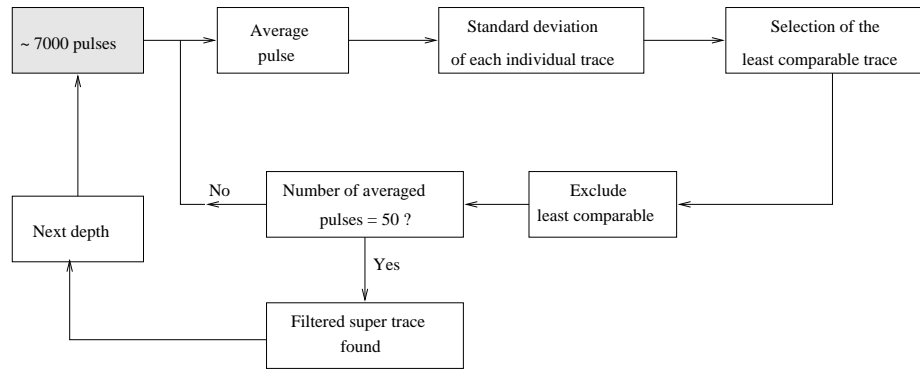


Figure 5.4: The filtering method to achieve the most probable pulse shape

In the filtering process, the sum of square value of the excluded pulse shape is decreasing as the process proceeds. The way the value is decreasing, is shown in figure 5.5 for the AC side. Due to the different number of pulses in the average, the sum of squares is plotted as a percentage of the total number of the pulses. The blue lines represent the depths close to the DC side (1 - 10 mm), where the red lines are close to the AC side (11 - 20 mm). The two lines with the lowest sum of squares values (in the first 20 % excluded pulses) are representing the depths 11 and 12 mm.

Together with the data sets for the different depths, the filtering method has been applied to filter a set of 1000 background events. The black line is representing these events. These can be considered as being random interactions throughout the detector. The background events are converging in the analysis process a lot later than the other depths. The first ~15% excluded pulse shapes have a relatively large sum of squares values independent of depth.

The lines representing the sum of squares are paired (e.g. 11 & 12, 10 & 13, etc.) corresponding to distance from the contact. The background data set has also a high sum of squares value initially. It can be seen that the depths close to the contacts are more susceptible to random events because they have a higher initial sum of square value.

After most of the random interactions are excluded, the value decreases much slower towards a final value of ~ 0.5 . In this process, the multiple interaction pulses are now being excluded.

The average pulse shape calculated will give a better representation of the response for

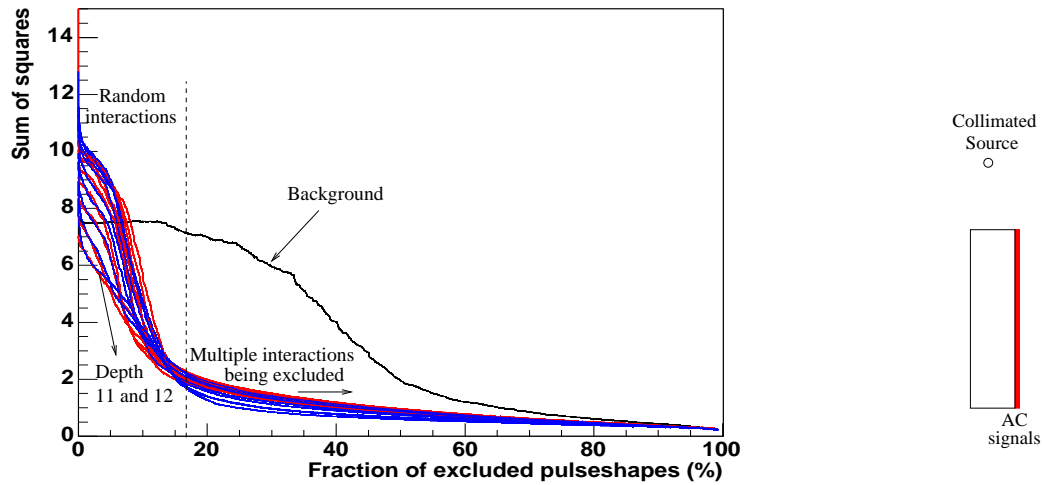


Figure 5.5: The sum of squares vs number of excluded pulse shapes (AC side). The lines in red represents depths close to the DC side (1 - 10 mm). The lines in blue represents depths close to the AC side. (11 - 20 mm). The black line represents a dataset of background events.

a particular depth.

5.4 Depth information from the pulse shape

The filtering method is used to create a database of pulse shapes for each depth in the side scan. Figure 5.6 shows the average pulse shapes for different depths by looking at the AC and DC signals. The interactions close to the DC contact are indicated by the red pulse shapes, the blue pulse shapes represents the response close to the AC contact.

The AC signals are slower than the DC signals. Apart from being slower, they also have a larger spread from one side to the other side of the detector. The response of the DC signals close to the contacts (red lines) are closer together than far away from the contact (blue lines). This indicates a non-linear behaviour. Both the AC and DC side are showing an effect which makes the pulse shape reverse in trend after 17 mm away from the contact. The reason for this effect will be given in the next section.

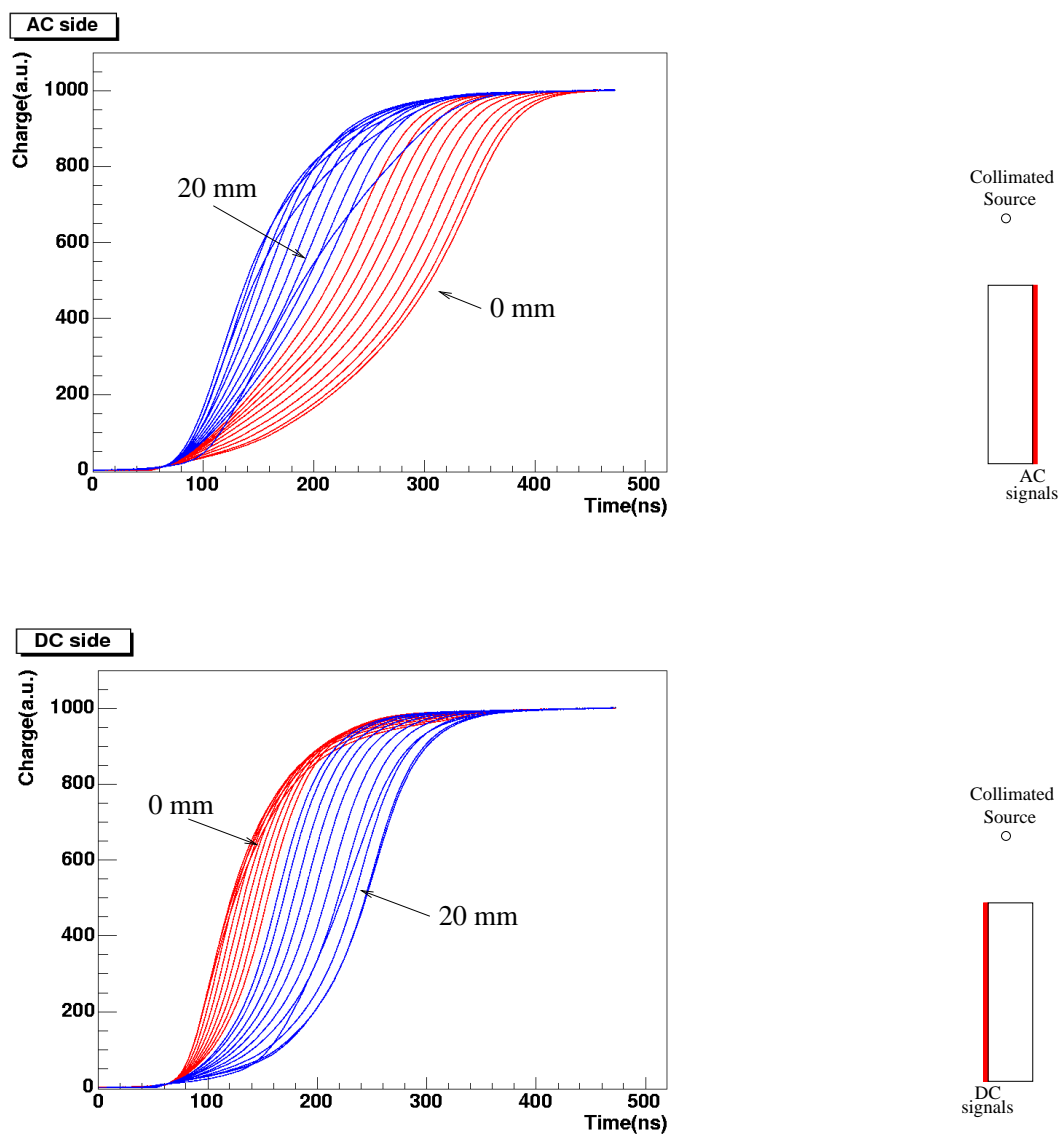


Figure 5.6: Pulse shapes varying with depth. The AC signals are shown in the top graph. The DC signals are shown in the bottom graph. The colour scheme is the same for both graph: the lines in red represents depths close to the DC side (1 - 10 mm), the lines in blue represents depths close to the AC side. (11 - 20 mm)

5.4.1 Considerations of the parameterisation for the depth

The different pulse shapes shown have a clearly different response throughout depth. To characterise the detector along the depth axis, a suitable parameter is required to describe each depth. Two factors have been taken into account:

- The starting point of the rise time should be chosen as close to the starting point of the pulse shape as possible. Ideally this is T_0 but due to the peak-to-peak noise level of 0.7% of the interpolated pulse, the T_1 is more practical and achievable. If the starting point is chosen any higher (e.g. T_{10}) the charge carriers have to travel a longer distance to induce enough current to reach this point. Within this distance, the parameter chosen will not have any sensitivity to any changes in pulse shape. This effect is particularly important for interactions far away from the contact. The weighting field is very weak and hence the charge carriers have to travel a much longer way before reaching the starting point of the rise time parameter.
- For interactions close to the contact, one type of charge carrier is collected very fast. As soon as this has happened, the induced current is decreased considerably because only half of the initial number of charge carriers are inducing the signal. The rise time will therefore be a lot slower for interactions in these regions. This effect becomes especially apparent for interactions in the high weighting field region near the contact. It makes the pulse shape curves back in as seen in figure 5.6. It has not got much effect on the pulse shape far away from the contact.

The peaks in indicated in figure 5.2 are pointing out the effects of these two consideration.

5.4.2 The choice of parameterisation of the pulse shapes

The consideration for parameterisation of the real charge signal leads to the conclusion that the starting point should be set to be T_1 . The choice for the end point of the rise time is chosen by looking at the different responses through depth. Nine different end points are chosen and shown in figure 5.7 for both the AC and DC side. There are a few differences noticeable:

- The general trend for both sides is a longer rise time.

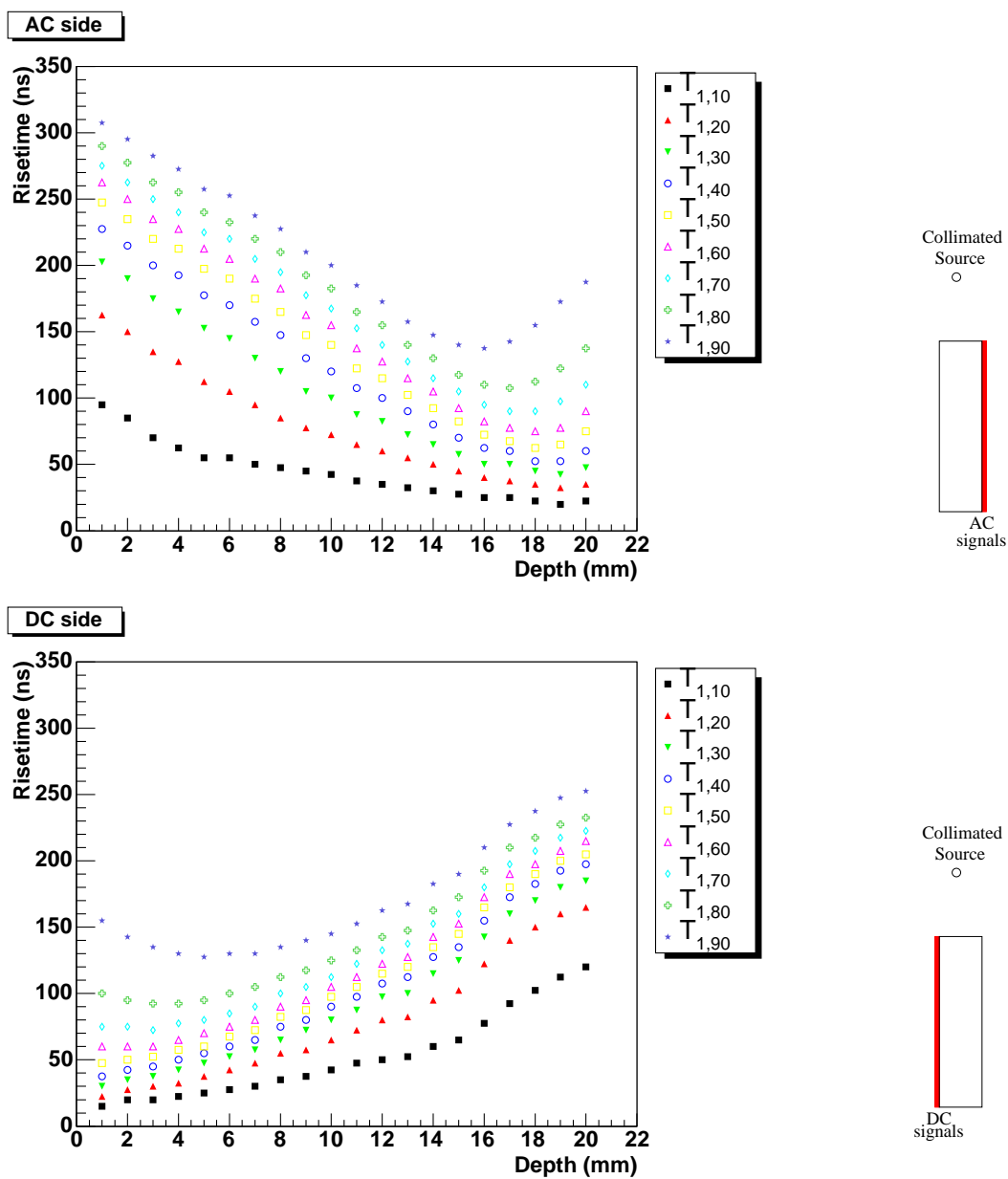


Figure 5.7: Nine different responses are shown with varying end-points for the rise time measurement. The starting point is set to T_1 . The responses of the AC and DC side are shown.

- It becomes clear that the general rise time for the DC side is faster than for the AC side. The differences between the AC and DC side can not be explained by the difference in mobility of charge carriers.
- Both sides seem to suffer from the second consideration (see 5.4.1) of a single type of charge carrier being present. All of the AC side rise times are showing an increase in rise time towards the contact. The response of the DC side only shows this in the rise times $T_{1,60} - T_{1,90}$.
- The $T_{1,10} - T_{1,30}$ rise times for both sides show an increase ~ 5 mm away from the contacts. The sharp change in gradient of $T_{1,10}$ indicates, it is possibly caused by the second factor (5.4.1) described. Here it has a much larger effect because the weighting field is very weak. If in this region one type of charge carriers is missing due to the collection, the risetime is extra long. This effect is only visible in the lower rise times because the charge induced to get the end point is relative small compared with the higher rise times.
- Apart from the regions near the AC contacts, the AC side response is much more linear than for the DC side.

From all the rise times on the AC side, the $T_{1,70}$ is spread out over the largest range. On DC side, the $T_{1,40}$ is spread out the most.

5.5 Depth dependence of the transient charges

The side scan is used to look at the transient charge response corresponding to each depth. The aim of this analysis is to find a parameter and compare it with the position resolution from the rise time analysis of the real charge.

5.5.1 Parameterisation of the transient charge

The transient charge area changes with the lateral position. This is used later on to determine the position in this direction. When investigating the transient charge response of the detector through depth however, it is important to have a uniform response in lateral direction. The shape of the distribution shown in figure 5.3 implies that the sum of the area

of the transient charge from both sides of the real charge is constant for each depth. The side scan data is corrected for the lateral direction by adding the transient charge area of the strips either side of the real charge together. This method provides a uniform distribution throughout the detector as figure 5.8 shows for the AC and DC side. The edge strips have only a single transient charge and hence these will be excluded from the analysis. The transient charges in DC11 are ignored because of the large energy deposition in the adjacent strips due to the charge sharing.

For a collimator position close to the DC contacts (y collimator position = 0 mm), the transient charges are positive for the AC signals and negative for the DC signals. The opposite response is observed for interactions close to the AC side. To find a good parameter the average signal response is calculated for each depth using a similar database approach as with the real charges.

5.5.2 Average transient charge database

A database of average transient charge has been created. To make all the transient charges comparable with each other, they are stretched and time aligned the same amount as the corresponding real charge. Four sets of average transient charges are created and shown in figure 5.9 and 5.10: the adjacent transient charges on the AC side, the next-to-adjacent transient charges on the AC side, the adjacent transient charges on the DC side and the next-to-adjacent transient charges¹ on the DC side. The colour scheme is the same as the real charges: the transient charges shown in red are corresponding to 1 - 10 mm, the blue transient charge are representing depth 11 - 20 mm.

The reference database for the transient charge shows the polarity gradually changing through depth for all four sets. The magnitude of the adjacent transient charges ranges from +15 % to -10 % of the real charge magnitude for both sides. For the next-to-adjacent transient charges, this range is +6 % to -5 % of the real charge magnitude.

The number of positive and negative transient charges through depth is different for all sets of average pulse shapes. For the adjacent strips, there are not as many depths producing negative signals than there are positive signals. For the next-to-adjacent strip,

¹It should be noted that although the next-to-adjacent gives a distinct response for the depth, these can not be used as a depth determination on an event-by-event basis. The noise level of 0.7% is too high to do that. The average pulse shapes is presented to provide a better understanding of the detector response.

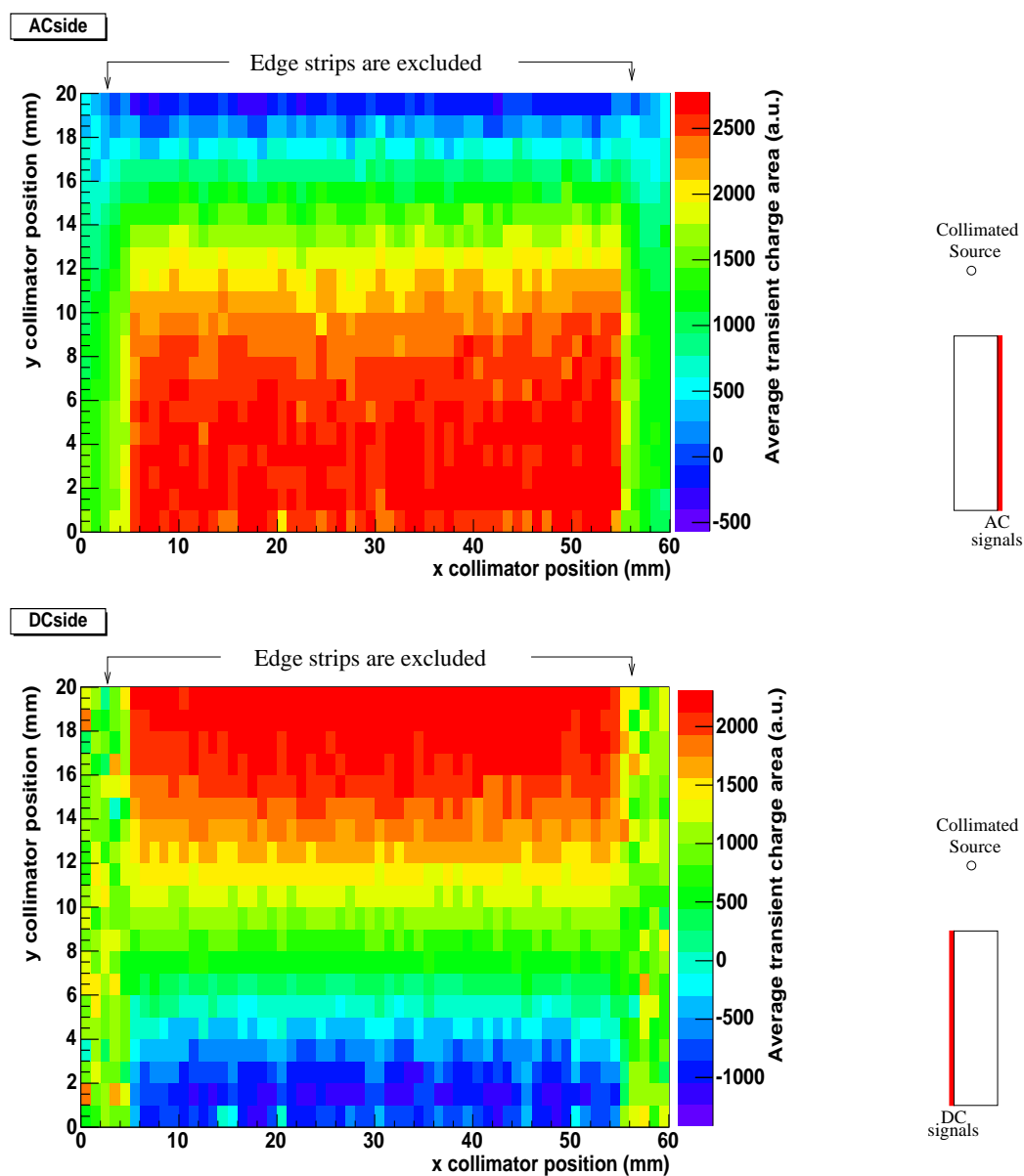


Figure 5.8: The transient charge area from the adjacent strips are added together to correct for the lateral dependence. A uniform lateral response is shown for the AC and DC side.

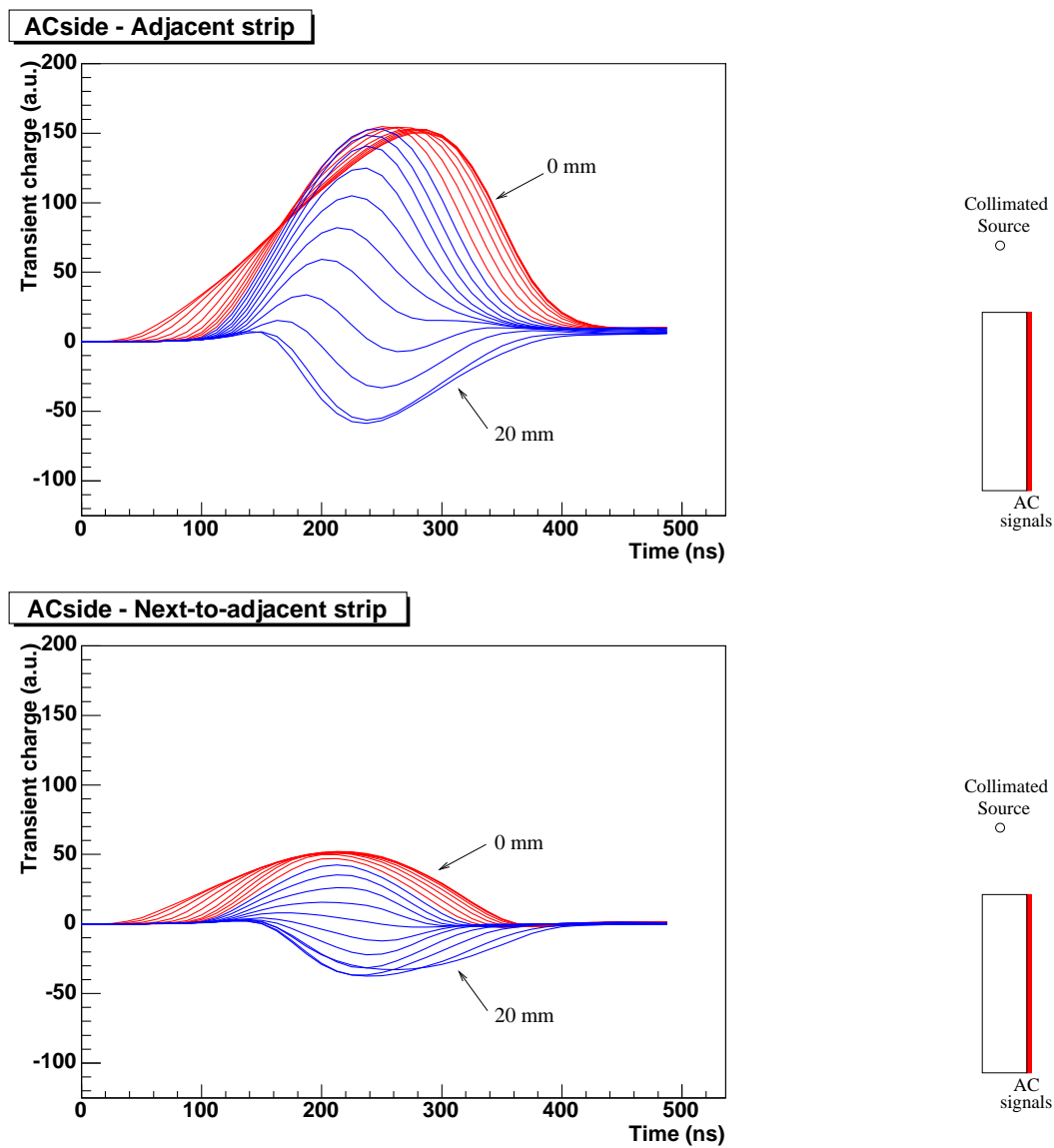


Figure 5.9: The average transient charge shape for different depths for the AC signals. The two different types of transient charges do vary in amplitude but also in shape. It can be seen that the number of negative transient charges is larger for the next-to-adjacent transient charges than for the adjacent transient charges.

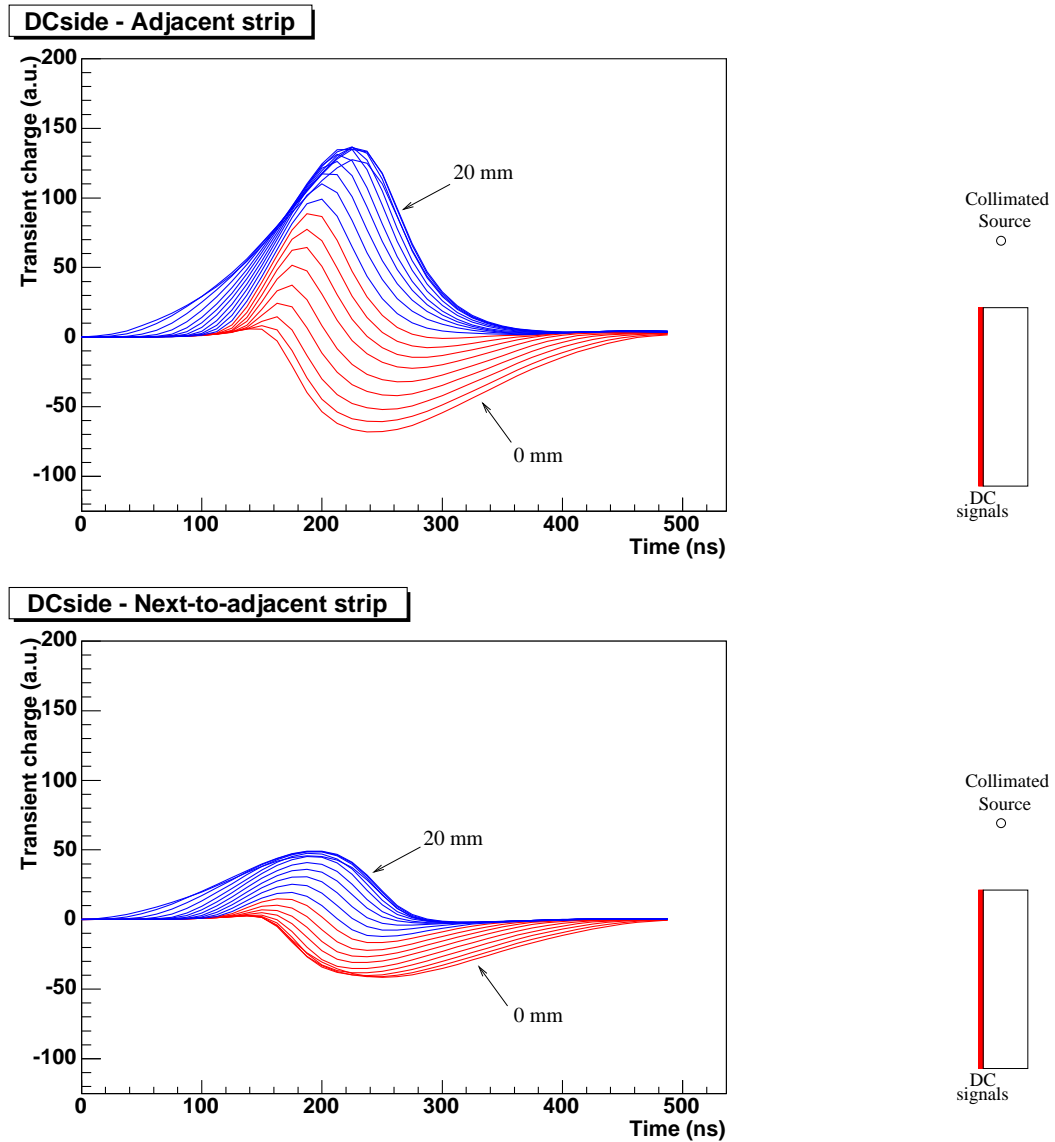


Figure 5.10: The average transient charges shapes for different depths for the DC signals. The same observations can be made as with the AC transient charges (see figure 5.9) the adjacent transient charges are larger in amplitude and there are less negative transient charges.

there is a similar amount of each polarity. The reason can be found in the shape of the weighting field which is discussed in Appendix B.

5.5.3 The transient charge value through depth

As seen in previous figures, the polarity changes through depth. By calculating the area using the database pulse shapes, a smooth difference can be observed through the different depths. These are presented in figure 5.11 for the adjacent and next-to-adjacent strips.

The adjacent areas are varying from -500 to 2500 for the AC side. The DC side range is (-1000 to 1500) smaller and are in general more negative. The next-to-adjacent signals are responding in a similar way except the ranges are a lot smaller (AC: -400 to 800, DC: -600 to 600). In the graphs it can be seen at which depth the transient charge area becomes negative. For the adjacent strips, this is ~ 2 mm away from the AC contact and ~ 6 mm from the DC contact. The next-to-adjacent transient charges are negative closer than ~ 10 mm for the DC side and ~ 5 mm for the AC signal away from the AC contacts.

To get extra depth information, the adjacent strips are of interest due to the good signal-to-noise ratio on an event-by-event basis. These can only be used in the parts of the detector close to the contacts due to the large gradient of the graph in this region (especially for the AC side). Far away from the contacts the area does not change very much and hence this will not provide a sensitive depth measure.

As seen in the rise time analysis, the depth can not be measured in the region close to the AC contacts using the $T_{1,70}$ parameter. This region can be characterised in depth with AC transient charge value.

5.6 The improvement in position resolution

The response of the detector through depth is outlined in the first part of the chapter. In the following part, the methods discussed are used to extract the position from the data. This provides a distribution of positions reconstructed using rise time and transient charge data for each collimator position of the scans.

The detector is considered in three directions separately: the depth, the lateral position parallel to the AC strips and the lateral position parallel to the DC strips. Each of them has to be characterised separately for the position resolution.

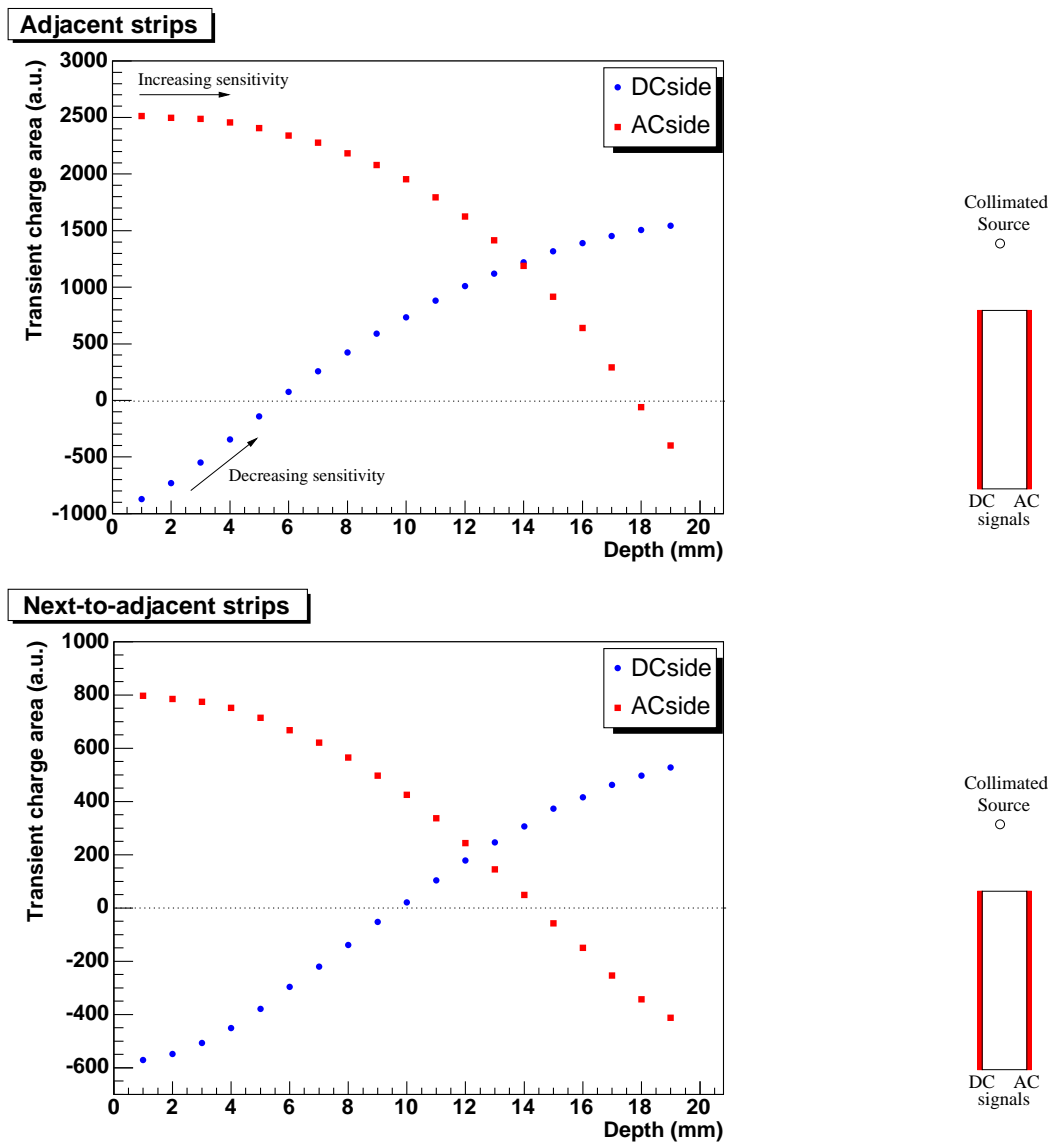


Figure 5.11: The area of the transient charge for each depth.

	AC	DC
$T_{1,70} / T_{1,40}$	105 ns	130 ns
Total adj. transient charge area	1188	1416
Reconstructed depth using:		
$T_{1,70} / T_{1,40}$	15.6 ± 0.2 mm (or 19.0 ± 0.2 mm)	14.5 ± 0.2 mm
Total adj. transient charge area	14.5 ± 0.2 mm	16.0 ± 0.5 mm

Table 5.1: The depth for the example event of figure 5.1 is determined using the four different methods. Note that according to figure 5.11 the adjacent transient charges on the DC side are not very sensitive. The AC side are more sensitive in this region.

5.6.1 Rayleigh criterion

The measure of position resolution has been chosen to be the Rayleigh criterion often used in the field of optics to describe the resolving power of two overlapping peaks or distributions. It states that two overlapping gaussian shaped peaks can be resolved, if the intensity between the two maxima drops with 26%. This amount of intensity drop corresponds to a peak separation of 2σ of the peak width.

5.6.2 Depth position

There are four different methods available to extract the depth. Table 5.1 shows the reconstruction of the depth for the example event from figure 5.1 using all four methods.

The method of choice should reconstructing the depth as well as possible and can be applicable over a wide range of depths. To determine this method, the position resolution of each of them is constructed. Table 5.2 and figure 5.12 shows the position resolution for each method.

For depths before ~ 12 mm, the position resolution is best determined by using the transient charge area of the DC side. For the remainder of the depth, the position resolution is best determined with the transient charges on the AC side. In figure 5.13, both methods are presented with the range their best to be used.

The determination of depth is important because it has an effect on the other two dimensions. To investigate the dependence of the position resolution through depth, the $T_{1,70}$ parameter has been used in combination with the AC transient charges. Although

Depth (mm)	$T_{1,70}$ AC (mm)	$T_{1,40}$ DC (mm)	Transient charge area AC (mm)	Transient charge area DC (mm)
1	1.82	-	-	1.15
2	1.77	-	-	1.11
3	1.80	-	-	1.09
4	2.09	-	-	1.13
5	2.06	-	-	1.27
6	1.99	-	-	1.32
7	2.06	-	-	1.44
8	2.01	-	-	1.51
9	1.98	4.96	3.22	1.76
10	2.09	4.11	2.69	1.86
11	2.08	3.75	2.21	2.20
12	1.99	3.37	2.17	2.34
13	1.94	3.28	1.82	2.92
14	1.75	3.00	1.93	3.14
15	1.68	3.37	1.92	4.39
16	1.92	3.21	1.56	-
17	2.18	3.24	1.88	-
18	4.59	3.38	1.69	-
19	3.61	3.14	1.41	-
20	-	2.58	0.92	-

Table 5.2: The position resolution expressed using the Rayleigh criterion for each depth. The two methods best suitable to reconstruct the depth are highlighted in bold.

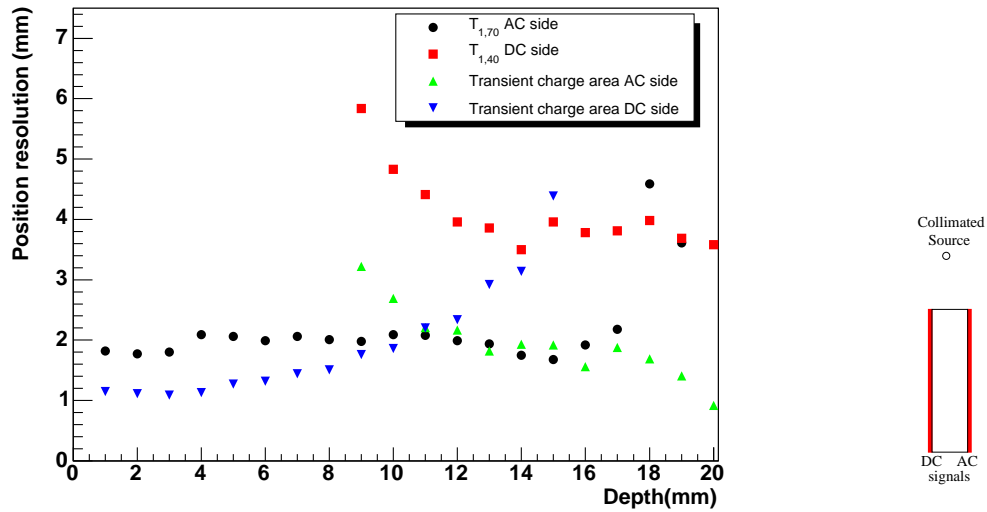


Figure 5.12: The position resolution has been measured using four different techniques. For depths without position resolution, the values were too large to put in the graph (see text for details).

this combination will not provide the optimum position resolution, it can reconstruct the depth. The lateral position will be investigated later on in section 5.6.3 individually for different depth selections.

By using both methods to reconstruct the depth of interaction, a comparison can be made with the collimator position (see figure 5.14). The figure shows a good agreement between the reconstructed position and the collimator position. The position resolution indicated by the error bars are worse for the rise time method as seen before.

5.6.3 Lateral position

The lateral position resolution is improved by the analysis of the transient charges from both sides of the real charge individually. The difference between the two transient charge areas (i.e. the asymmetry) gives an indication of the interaction position in this direction. The lateral position is split up in to 5×1 mm positions corresponding to the five collimator positions across each strip.

The lateral analysis is done using the side scan and the front face scan. The AC transient charge response can be calibrated directly from the side scan using the collimator position

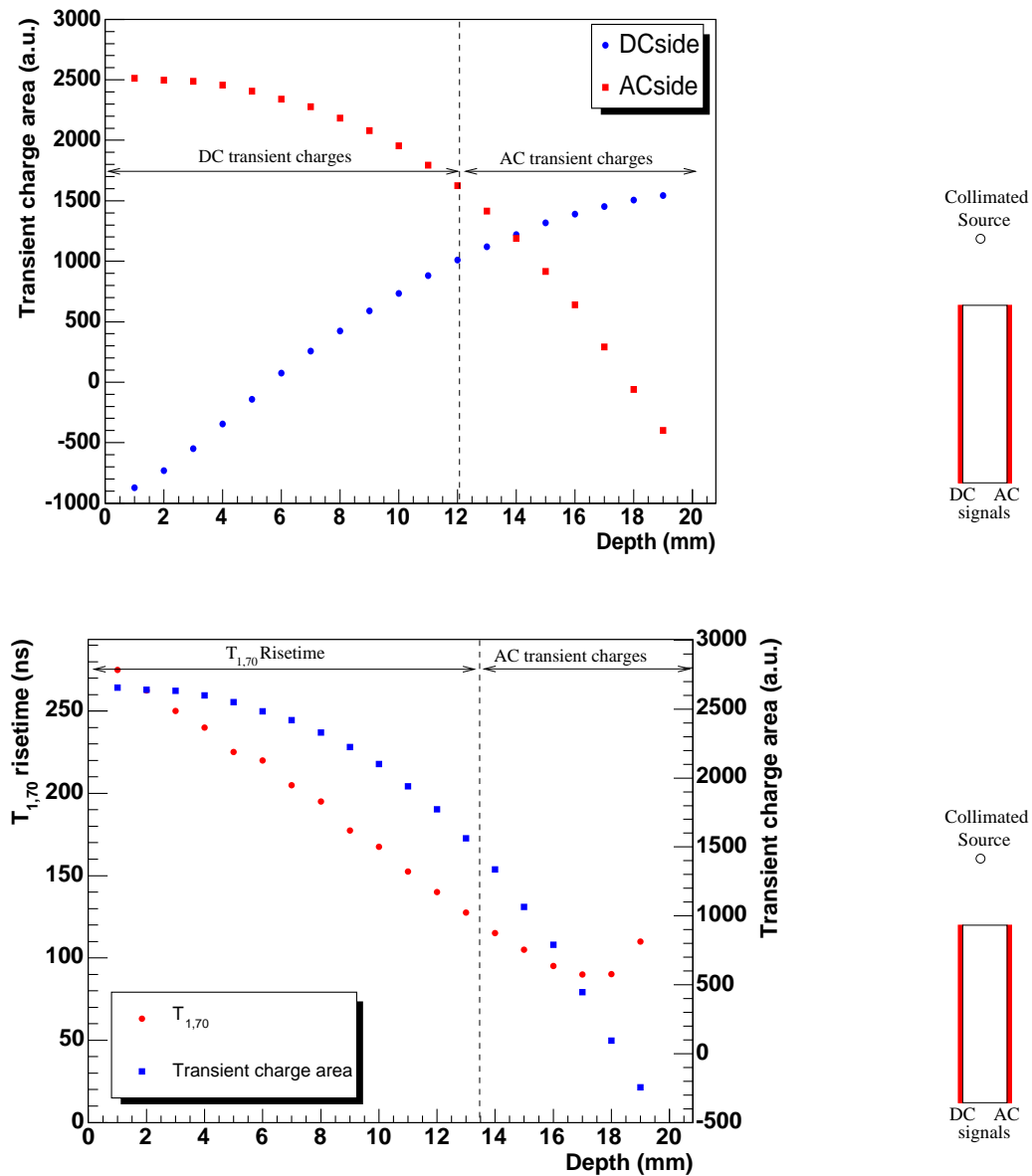


Figure 5.13: The first method (top) as a depth determination uses the adjacent transient charge area of the AC and DC side. The separation between the most sensitive region is set at 12 mm because the AC transient charges provide a better position resolution past this point (see figure 5.12). The combination of the $T_{1,70}$ rise time of the AC side and the transient charge area (bottom) are used as a comparison with the first method used. This method provides a slightly worse position resolution for the first part of the detector.

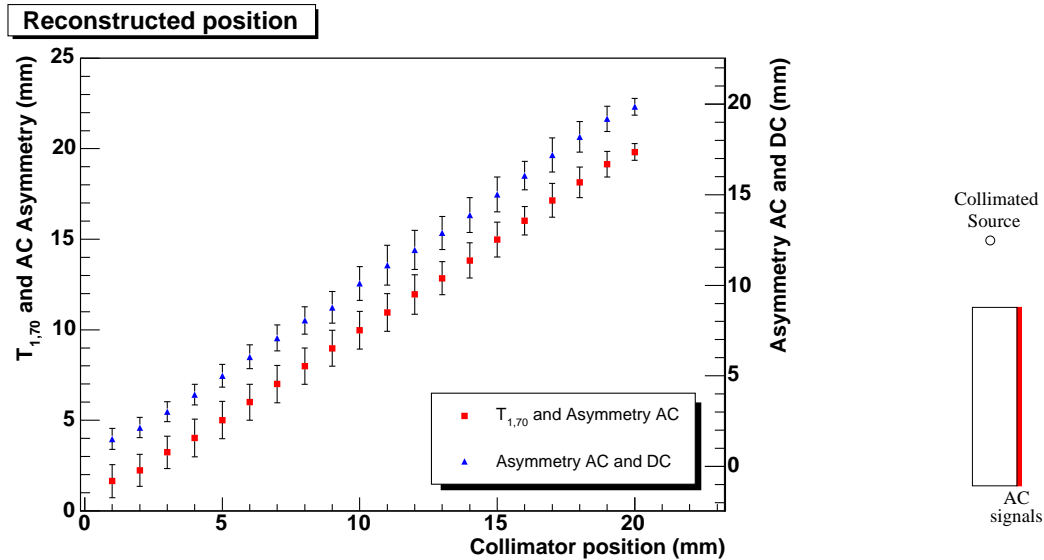


Figure 5.14: The reconstructed position has been calculated by using the combination of two methods. Both methods show good agreement with the collimator position. The error bars are indicating the position resolution. Note that the graphs are drawn on different axis.

for the depth. The DC side transient charges require the front face scan combined with the reconstructed depth determination. As a comparison for the DC side, the AC lateral position is also calculated using the front face scan.

Side scan analysis

The side scan data set has been used to investigate the position resolution in the AC lateral direction. The response of the AC side is shown in figure 5.15 using the collimator position for the depth. The figure is split up into five different lateral positions. Position 1 and 5 represent positions close to either side of the strip boundary.

The asymmetry is constant for the first ~ 12 mm for all lateral positions. After this region, the lateral asymmetry changes. Lateral position 3 (i.e along the middle of the strip) does not change polarity, but stays constant throughout all depths. The maximum asymmetry can be found at position 1 and 5 (i.e. close to the strip boundary) for regions close to the DC contact.

Each of the 5 subfigures contains 20 different distributions representing different depths. The width of the peaks in the distribution is extracted by a gaussian fit. This then is

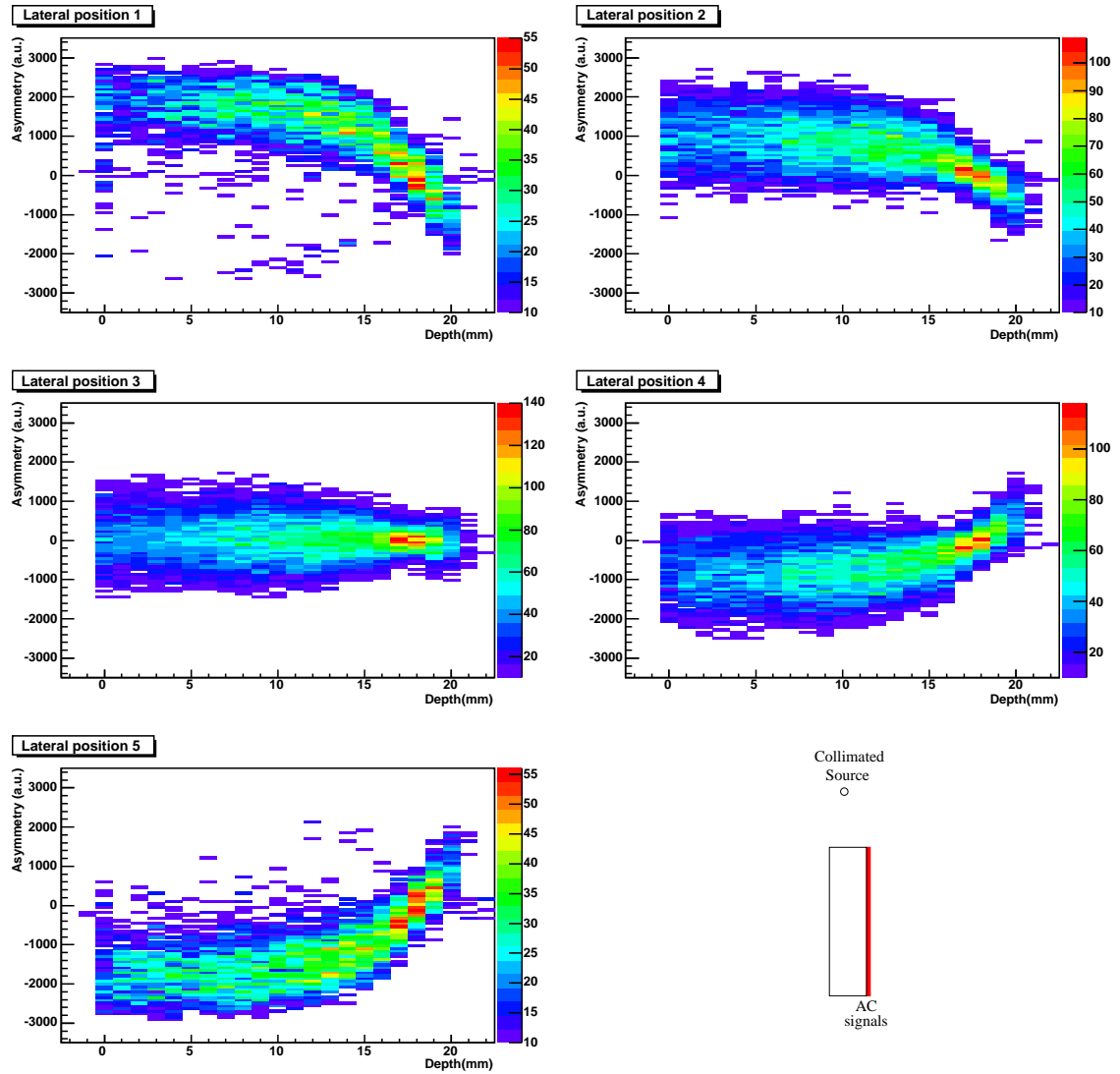


Figure 5.15: Asymmetry for the transient charge on AC side using the collimator position of the scanning table. Position 1 and 5 are close to the strip boundary. Position 3 is in the middle of the strip. The insensitive region is the region where the asymmetry changes polarity.

compared with the spread in the peak positions between each lateral position for that depth to get a calibration measure. The position resolutions for each of the distributions are included in table D.1 in the Appendix. A summarized version is included in table 5.3 showing the average position resolution for each depth. To investigate the influence of the depth position resolution on the lateral position resolution, there are four methods used to identify the depth: the collimator position (1), the transient charges of the DC side (2), the the transient charges of the AC side (3) and the risetime $T_{1,70}$ of the AC side (4). The methods 2, 3 and 4 are using the reconstructed depth (i.e. 2 - 4) and hence have got a region where it is insensitive (see section 5.6.2). These regions are indicated in italic. The regions where the optimum depth position resolution is available are highlighted in bold.

The following conclusions can be drawn from the position resolutions of the different methods:

- The general trend of the transient charge through depth is best seen in the data set using the collimator position (method 1) because it is independent from any reconstruction sensitivity. For the depths 1 - 12 mm, the position resolution is constant with an average value of 1.8 mm. After this region, the position resolution is decreasing.
- The transient charges of the DC side, provide a good sensitivity in the region 1 - 12 mm and hence result in a similar position resolution as the method 1. By having a larger position resolution in depth, the method is calculating the lateral position resolution over a larger depth region. For the region where the asymmetry is changing rapidly with depth (15 - 20 mm), this results in a larger lateral position resolution.
- The transient response of the AC side (method 3) is insensitive in depth in the region 1 - 12 mm. However, method 1 shows the asymmetry not changing in this region and hence the position resolution calculated using method 3 is not changing from method 1. In the depth region where this method is used (13 - 20 mm), this method shows an improved position resolution compared to method 1.
- The general response of the risetime (method 4) is comparable with the other methods in the region where the asymmetry does not change. The position resolution for the depths in the region 14 - 20 mm shows an increasing position resolution. Depth 17 has a good resolution because the $T_{1,70}$ risetime is reversed from this point onwards.

Depth (mm)	AC lateral position resolution (mm)			
	Collimator depth method 1	Transient charges DC depth method 2	Transient charges AC depth method 3	$T_{1,70}$ AC depth method 4
1	1.77	1.80	-	1.96
2	1.73	1.71	-	1.57
3	1.80	1.78	<i>1.89</i>	1.79
4	1.79	1.90	<i>1.64</i>	1.78
5	1.80	1.84	<i>1.80</i>	1.83
6	1.76	1.87	<i>1.70</i>	1.74
7	1.73	1.97	<i>2.00</i>	1.73
8	1.83	1.91	<i>1.83</i>	1.68
9	1.87	1.74	<i>1.85</i>	1.77
10	1.85	1.90	<i>1.83</i>	1.73
11	1.75	1.95	<i>1.86</i>	1.90
12	1.92	1.93	<i>1.93</i>	1.91
13	2.15	2.14	<i>2.36</i>	1.85
14	2.43	<i>2.48</i>	1.68	1.96
15	4.32	<i>3.14</i>	2.49	<i>2.64</i>
16	44.76	<i>4.45</i>	8.41	<i>7.57</i>
17	4.38	<i>7.01</i>	8.05	<i>0.99</i>
18	7.18	<i>15.1</i>	2.66	<i>5.73</i>
19	5.59	<i>19.1</i>	1.50	-
20	5.79	<i>12.3</i>	4.37	-

Table 5.3: Average lateral position resolution for the AC side scan using different methods for depth. The figures highlighted in bold are used to calibrate the AC side asymmetry. The italic figures are indicating the regions where the depth measure is not sensitive (see figure 5.12). The purpose of this table is to show the influence of the different methods of determining depth on the position resolution in lateral position. All figures are expressed as the Rayleigh criterion. Depths with a larger position resolution than 5 mm should be considered as insensitive throughout the strip width. The larger value is due to the method of calculating the position resolution.

Front face scan analysis

The front face scan is used to characterize the lateral response for both the AC and DC side. The AC transient charge characterization is done again as a comparison with the DC side. The depth is reconstructed using the transient charges of both sides (method 2 and 3 combined, see figure 5.13).

The transient charges on the DC side (figure 5.16) show a similar but opposite trend as the AC side (figure 5.15). Lateral position 1 of the front face measurements of the DC side is on the border of two strips and hence the response is a combination of the two strips. Due to the shared number of the counts the number in both peaks is not enough to be usable. This lateral position is therefore excluded from this part of the analysis and is done by only using the other four positions within each DC strip. The AC characterization has not got this problem and hence is done with the full 5 lateral position.

The average values for the AC and DC side are presented in table 5.4. There are three sets of values presented in the table. The first one is using the collimator position for the depth presented before in the side scan section. The second and third set are the AC and DC values using the reconstructed depth discussed in section 5.6.2 using the front face scan data.

Throughout most parts of the detector, the position resolution is constant. All sets of values are showing an increase in position resolution ~ 5 mm away from the contact of interest. By using the reconstruction algorithm it can be seen that this insensitive part is a very localized effect.

The insensitive region occurs where the bipolar transient charge are induced. A possible cause for the insensitivity is the quick change of the transient charge shape with depth and a collimator spread of 1.2 mm in diameter covering a wide range of bipolar shapes. It can therefore be concluded that with this collimator setup it is not possible to improve the position resolution beyond the strip width for this region using this analysis.

In figure 5.17, the average position resolutions for each lateral position are summarised. The insensitive regions have been given a position sensitivity of 5 mm. The benefits of the reconstruction algorithm becomes clear after the comparison of the two AC sets of values. The general difference in position resolution between the two sets is a factor ~ 1.5 in the sensitive region. When the DC side is compared with the (reconstructed) AC side, the DC

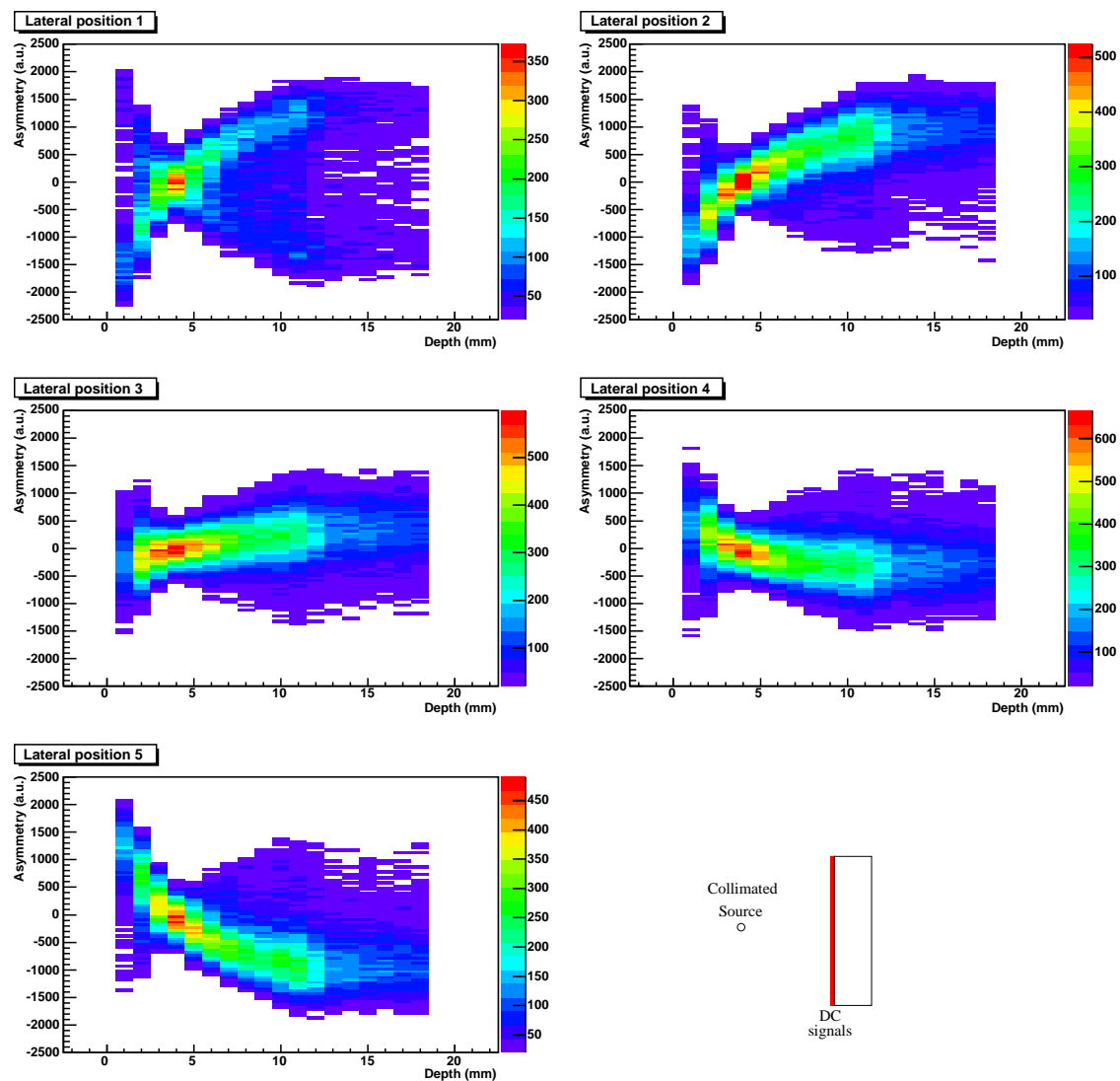


Figure 5.16: Asymmetry for the DC side using the AC and DC transient charges to reconstruct the depth position. A similar insensitivity can be seen using the DC transient charges. It is positioned on the opposite side of the detector, close to the DC contacts.

Depth (mm)	Collimator position (mm)	Lateral position resolution AC (mm)	Lateral position resolution DC (mm)
1	1.77	0.96	1.14
2	1.73	1.00	1.54
3	1.80	1.12	3.30
4	1.79	1.14	13.61
5	1.80	1.15	7.04
6	1.76	1.18	3.42
7	1.73	1.23	2.00
8	1.83	1.15	1.82
9	1.87	1.19	1.68
10	1.85	1.21	1.64
11	1.75	1.22	1.58
12	1.92	1.23	1.58
13	2.15	1.38	1.56
14	2.43	2.75	1.60
15	4.32	1.10	1.62
16	44.76	2.56	1.65
17	4.38	10.65	1.73
18	7.18	8.21	1.63
19	5.59	1.98	1.72
20	5.79	1.21	1.50

Table 5.4: The average lateral position resolution has been calculated using the front face data set for both the AC and DC side. The depth is reconstructed by using the AC and DC transient charges. The positions with a position resolution over 5 mm should be considered for the trend but not for an exact value.

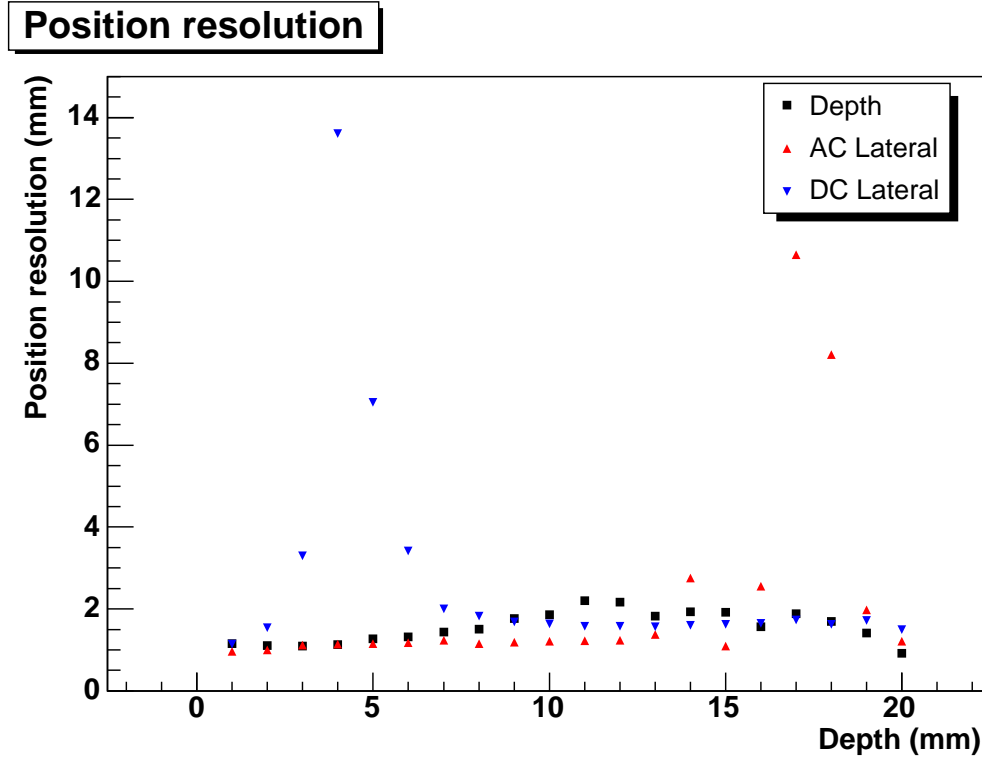


Figure 5.17: The position resolutions expressed as the Rayleigh criterion for all three dimensions.

side provides a better overall position resolution. This leads to the conclusion that the AC side transient charges provide a better lateral position resolution.

The overall improved position resolution in depth is ranging from 0.92 mm to 2.20 mm and is on average ~ 1.55 mm. The lateral position resolution parallel to the AC strip is ranging from 0.96 mm to 10.65 mm. The lateral position resolution parallel to the DC strip is ranging from 1.14 mm to 13.61 mm. It should be noticed that the value quoted above 5 mm position resolution can not be practical because of the strip size being 5 mm.

Chapter 6

Conclusion and discussion

6.1 Conclusion

The requirements for a method to determine the interaction position in germanium γ -rays detectors are presented. The use of a segmented germanium detector with pulse shape analysis offers the ability to reconstruct the interaction position beyond the initial segmentation and gives excellent energy resolution. The first SmartPET detector has been characterized in two stages. The first stage determined the general performance of the detector. The second determined the methods required to determine the interaction positions.

The energy resolution for all the strips, except DC11, is as expected (1.4 keV at 662 keV) with the edge strips having a slightly increased energy resolution. The energy resolution was found to vary at different depths. This effect is present for pulses taken from both sides of the detector although it is more pronounced on the DC-side. The energy resolution of DC11 is worse due to charge sharing following a manufacturing fault. The photo peak energy for different positions along this strip leads to the conclusion that the charge sharing is position dependent.

The efficiency of the detector shows a difference between the AC and DC side of the detector. The AC side has a much higher low energy efficiency than the DC side. Because the DC side has relatively thick contacts ($50\ \mu\text{m}$) compared to the AC side ($0.3\ \mu\text{m}$), more low energy γ -rays will be absorbed within the contact.

The detector is suffering from a small amount cross-talk of 0.9% (6 keV at 662 keV) on the AC-side. The cross-talk on the DC side is 0.15% (1 keV at 662 keV). A method has

been developed to reduce the cross-talk to 0.15% (1 keV at 662 keV) on the AC-side and to 0.06% (0.4 keV at 662 keV) on the DC-side.

The second part of the characterization has been performed with the purpose of improving the position resolution using pulse shape analysis. To be able to use pulse shape analysis in the appropriate way, a detailed study has been carried out of the signal generation in the detector. From this study it can be concluded that the concept of the weighting field is dominating the signal generation process which in turn leads to the position sensitivity of the detector.

A scanning setup has been used to identify the response of the detector. The response includes three different types of events: single, multiple and random interactions. The influence of each of the three types of events has been investigated using experimental techniques. The random interactions have the largest influence on the average response. The influence of the multiple interactions on the real charge has been identified, but by using an appropriate scanning method, this effect was minimized.

The detector has been characterized in three dimensions. The most important of these is the depth. The depth of interaction determines the shape of the all signals, where as the lateral position predominately changes the amplitude of the signals. Both the real and transient charges are parameterised. The parameterisation of the real charges is based on the study of the signal generation. Two sets of average responses have been created, one for the AC and one for DC side. The rise time starting point has to be chosen as soon as possible after the start of the signal to pick up the very first movement of the charge carriers. Due to noise level the starting point is chosen to be at 1% of the final magnitude of the pulse for both the AC and DC side. This point can be measured directly from the pulse. The end point is based on the largest spread in rise time values through depth and the best linear response. By looking at the average real charge response, the T_{70} and T_{40} have been concluded to be the best end points for the AC and DC side respectively. The transient charge has been characterized by using the area underneath the signal. This provides a smooth depth dependence and can be used on an event-by-event basis with a low noise level.

The position resolution is determined as a quality factor of the detector performance. By using different signals the position resolution is measured for each of the three different

dimensions. The first position resolution is determined for the depth. From the four ways investigated to determine the depth, a depth position resolution of 1.1 mm is obtained using the combination of transient charges areas from the AC and DC sides.

Unlike the depth, there is no choice in method to use for the lateral dimension. To improve the lateral position the depth should first be identified and then the asymmetry of the transient charge areas used to improve the determination of the lateral position. An average position resolution of 1.2 mm for the AC side and 1.7 mm for the DC side has been obtained. There is however an insensitive region about 4 mm away from each collecting contact. In this region, the position can not be improved using the transient charges.

By using the pulse shape analysis methods, the detector can be divided into voxels of $1.2 \times 1.7 \times 1.1$ mm corresponding to over 30000 voxels.

6.2 Discussion

To use germanium detector in a small animal PET system, the position resolution gained from this work is competitive with current small animal pet scanners. However the position resolution is not equal throughout the complete detector volume. In the regions where the transient charges have a bipolar shape, no lateral improvement can be obtained.

The position resolution of the detector has been investigated for full energy (662 keV) events. However this is a small fraction of the total data set due to scattering behaviour of the γ -rays. If these scattered events can be used in the reconstruction, the efficiency of the system could improved.

The influence of multiple events inside one strip on the signal generation is not well understood and needs further investigation. The effect of them could cause the position resolution to degrade. However the influence of this effect can only be seen when the results of this work are used to produce images.

The general differences between the response of the AC and DC sides can not be explained fully. The energy resolution for different depths is an example showing this difference in behaviour. The reasons are hard to determine and from this data set can only be speculative. Possible reasons for this behaviour could be the difference in impurity concentration with depth, hole trapping inside the detector or a weighting field effect. The differences between both sides are present in the pulse shape response of the detector. The overall

response of the DC side is a lot faster than the AC side. The reason for this is unknown but could be caused by the differences in electronic circuits between the AC and DC side.

6.3 Future work

The following suggestions should be carried out:

- The SmartPET electronics is able to run algorithms providing accurate position information. The algorithms used need to be able to run at a high speed. Therefore the simplest and most effective algorithm should be picked. The parameterisation of the signals is a partially defining the complexity of the algorithm. The transient charges are parameterised as the area underneath the signal. It is possible to parameterised the real charge in the same way (see the shaded area in figure 6.1). There are two main advantages by doing this. Firstly, the real charge could provide an improved position resolution for the using the real charges for the depth. Secondly, more importantly, this parameterisation allows combining the real and transient charge. The multiple events and events with interactions in the neighbouring strips are made out of a combination of the two signals (either real charge and real charge or real charge and transient charge). By matching the areas of all the signals on an event-by-event basis using an iterative routine, it may be possible to extract each individual interaction position.
- The matching procedure should include a well defined time alignment for all the signals. For both the real and transient charges, this can be done by finding the starting point of the signals. In the case of both signals, this involves developing an algorithm to find T_0 or improving the electronics so all signals are synchronised.
- The lateral position can not be improved beyond the segmentation size for the parts of the detector where the signals shapes change rapidly. It is therefore advisable to scan the detector with a narrow collimator of 0.5 mm and /or decrease the step size to 0.5 mm. This will give more information about the change of response in the insensitive region.

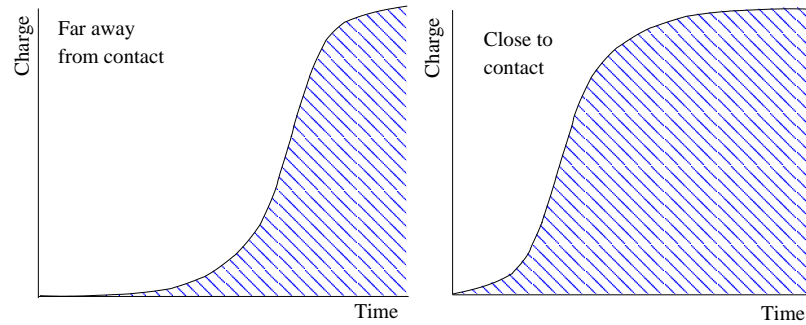


Figure 6.1: The parameterisation of the real charge should be changed so the complete signal is used. Shown are two different pulse shapes for an interaction close to and far away from a contact. The area underneath the signals are significant different. This should reduce the noise level on an event-by-event basis and could have potential to deconvolve multiple / convolved events.

- Pulse shape analysis provides the opportunity to divide the detector volume into a number of small voxels. For a more efficient system, a larger amount of germanium should be considered to provide more interactions. This can be achieved two detectors behind each other. This would also provide the opportunity to do single position emission reconstructed tomography (SPECT) and PET at the same time.
- The position resolution has been considerably improve using pulse shape analysis. The next step is to use the developed algorithms to produce the images in a PET system.

Appendix A

Energy measures

There are three possible methods used to extract the energy. They can be split into two categories: analogue electronics and digital electronics (baseline difference and moving window deconvolution).

The analogue resolutions were used with conventional analogue electronics setup with a $6\mu\text{s}$ shaping time.

The baseline difference is extracting the energy using the digital data. The difference in pulse height of the real charge is proportional energy. It is calculated over a set number of samples. The time window to average over is chosen to be $0.625\ \mu\text{s}$ starting $1.875\ \mu\text{s}$ after the start of the pulse. The difference is used as an energy measure.

The moving window deconvolution is similar to the baseline difference method. The method calculates the average over a number of samples after the start of the pulse. It varies from the baseline difference because it corrects for the preamplifier decay of $43\ \mu\text{s}$. After the correction the average is calculated over a flat part of the pulse rather than the slope introduced by the decay. The average will therefore have a smaller variance and hence an improved energy resolution is the result.

A schematic of the working of the moving window deconvolution method is shown in figure A.1 . The top part shows an schematic example of a pulse shape (black line) from which the energy is calculated from. The correction of preamplifier decay is made visible by the blue shaded area. The red square at the start of the pulse is the time window over which the average is calculated. The average is put into the second schematic drawn in red. The rising edge of the pulse shape is neglected for schematic purposes. The window has

been moved over the complete trace resulting in a trapezoid shape. At the end of the trace, a second trapezoid edge is formed due to the step back to the baseline. The average used for the energy is taken just before the start of the second trapezoid edge.

The algorithm has been programmed into the GRT4 modules. Several parameters are necessary to produce the optimum energy resolution. The used parameters of the MWD algorithm are shown in table A.1 and indicated in the schematic.

Shaping time	8.0 μs
Trapezoid width	5.5 μs
Peak separation	12.5 μs
Decay time constant	53.0 μs
Peak sample time	7.8 μs

Table A.1: MWD parameters used to improve the energy resolution

The improvement in energy resolution obtained by using the different energy measures are presented in table A.2. The moving window deconvolution provides an improved energy resolution compared with the baseline difference. However, the moving window can provide an energy resolution equal to the analogue energy resolution. This is due to a fault in the algorithm in the cards at the time of the measurements. Although the algorithm is not optimum, the energy resolution is still better than the baseline difference resolution.

	Analogue	MWD	Baseline
122 keV	1.78	1.77	3.61
968 keV	2.25	2.58	4.39
1408 keV	2.17	2.61	4.63

Table A.2: The energy resolution for strip AC06 measured with the three different methods. The three methods are ordered in worsened resolution.

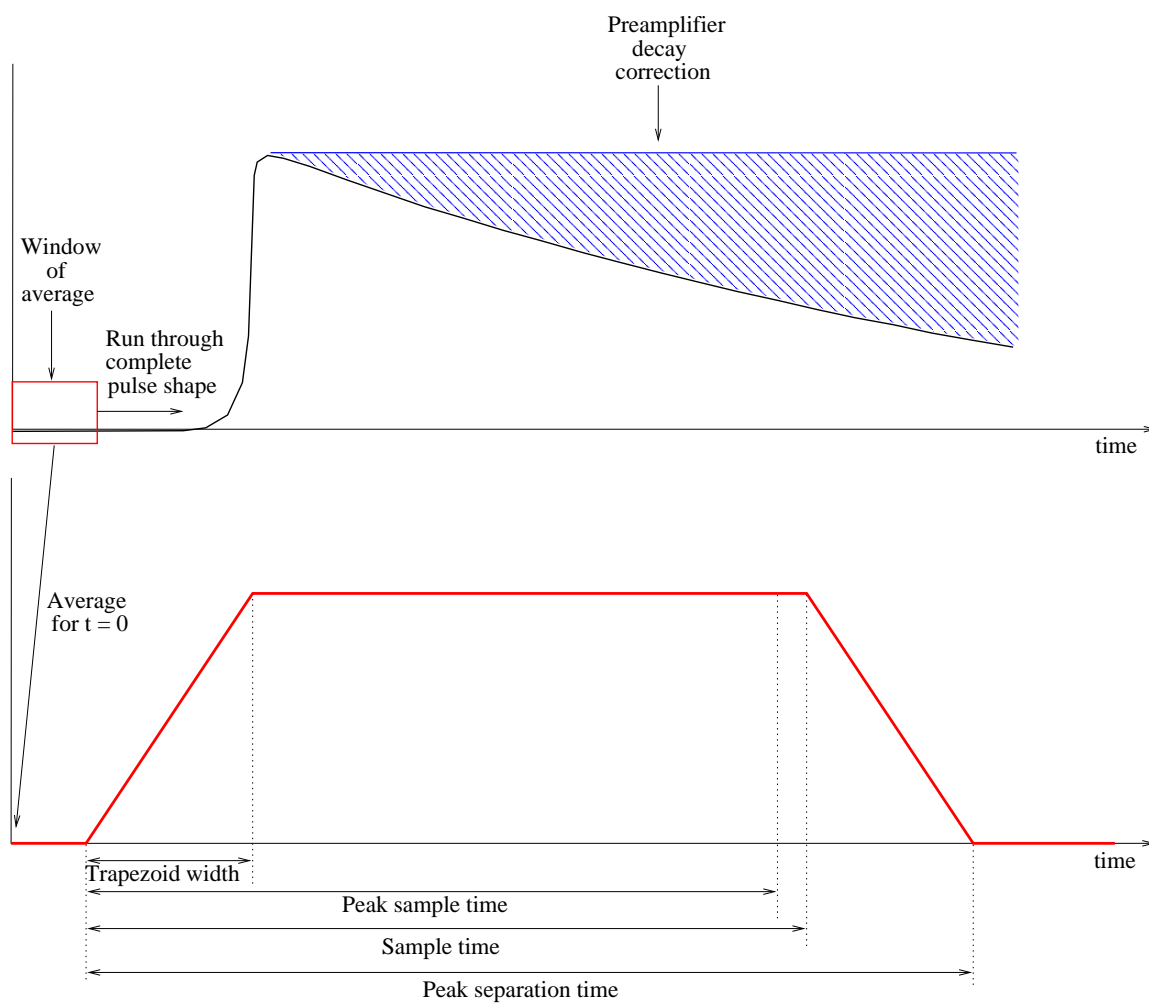


Figure A.1: The working of moving window deconvolution method is shown in this schematic. The trapezoid width equals twice the average window. The sample time is the length of the trace used for the decay correction. The peak sample time defines the position where the average is taken from. This should be chosen just before the sample time so no rise time effects interrupt the measure of the energy. The peak separation time is the time the complete process takes. This is important for baseline calculations.

Appendix B

Weighting field construction

In order to clarify the shape and magnitude of the signals, this appendix shows the concept of the induced signals. The concept only considers two dimensions (depth and 1 lateral). The third remaining dimension can be easily extrapolated from the other two.

It should be emphasized that this model should only be used as a guide towards a better understanding of the weighting field and the signal generation. It can also be used as an indicator of the trends. The calculations have been done ignoring any interstrip gaps and contact thickness.

B.1 A simple model

The induction of the current in the electrodes comes about from a variation in the Coulomb field due to the movement of the charge carriers. The movement of the charge carriers causes two parameters to change:

- The intensity of the Coulomb field increases if the charge carriers are closer to the electrode. This has an $1/r^2$ relationship with distance.
- The angle between the drift velocity and the electrode: the electrode of a width of 5 mm is split up into 500 parts for the calculations. The angle between each of the parts and the velocity vector defines the amount of change in Coulomb field the electrode will see. The change at an angle of 90° of the velocity equals 0 where the change at 0° is maximum.

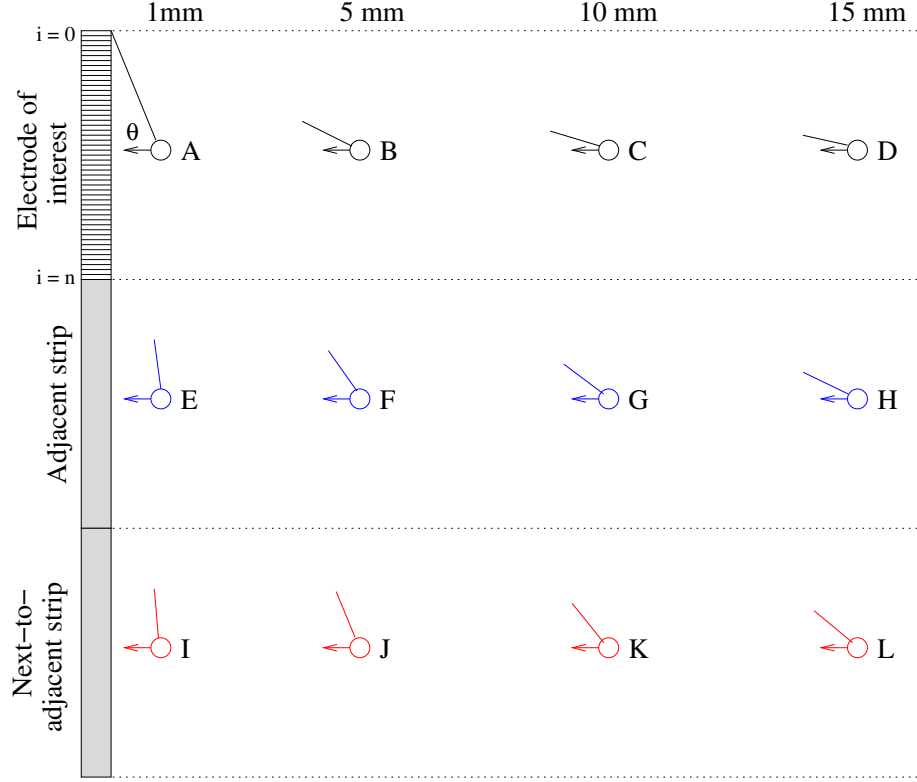


Figure B.1: Twelve points have been taken to show the concept of the weighting field. Four interaction depths are chosen within each strip. The lines drawn are indicating the coverage of the Coulomb field by the electrode.

As an example, the change in these two values is calculated for twelve points. A schematic of the three strips of interest is shown in figure B.1. The lines drawn are pointing out the angle. Twelve interaction positions for 4 real charges (A-D), 4 transient charge in the adjacent strip (E-H) and 4 transient charges in the next-to-adjacent strip (I-L). To calculate the weighting field for each point, the electrode of interest is split up into 500 parts. The weighting field for each position is here defined as:

$$E_w = \sum_{i=1}^n \frac{\cos(\theta_i)}{r_i^2} \quad (\text{B.1})$$

where n is the number of parts, θ_i is the angle between the drift velocity and each part of the electrode and r_i is the distance.

	A	B	C	D
Weighting field	118.6	46.3	24.5	16.5
	E	F	G	H
Weighting field	7.32	8.46	3.73	1.92
	I	J	K	L
Weighting field	0.62	2.09	1.91	1.33

Table B.1: The weighting field values for the twelve points chosen.

The weighting field for the real charges (A-D) is decreasing with depth: as the charge carriers are moving away from the contact, both $\cos(\theta)$ and intensity are decreasing throughout the complete depth. This means the current does not change polarity resulting in a real charge. The weighting field of real charges is considered to be uniform for each lateral position in the strip. In theory, it does change towards the strip boundary but the effect is considered to be neglectible on a event-by-event basis.

The weighting field for the (next-to-)adjacent strips is more complex. For the remaining eight points in the (next-to-)adjacent strips, the angle is decreasing moving away from the electrode which makes the $\cos(\theta)$ contribution increase. At the same time the distance is increasing which leads to decrease of this contribution. A maximum will occur due to the combination of these two contributions.

Figure B.2 shows an intensity map of the weighting field calculated for a fine grid of points. The complete weighting field has been made visible for the adjacent and the next-to-adjacent strip. Within the adjacent strip, the weighting field is changing a lot both in lateral and depth position. In the next-to-adjacent strip, the weighting field is changing less in both direction. The lines drawn are showing the different regions of the polarity of the transient charges. The line indicating the negative side of the bipolar region is placed at the maximum of the weighting field for each depth. The positive side of the bipolar regions is placed at half the distance between the negative side and the edge of the opposite contact. The transient charges become bipolar within these two lines. Although they are all bipolar, they do have different ratios between positive and negative areas.

The largest area in the adjacent strip is the region where positive transient charges are produced. This region is getting smaller further away from the strips. While this region is

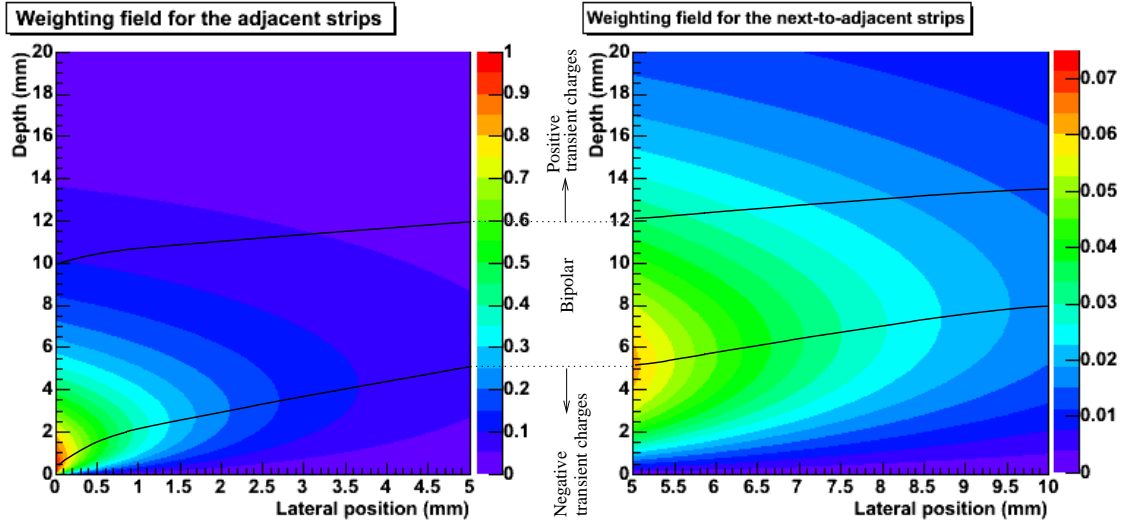


Figure B.2: The weighting field constructed out of the two parameters of coverage and distance. The graph is split up into three regions defining the shape of the transient charges.

decreasing in size the other regions are increasing. In the next-to-adjacent strips all three regions are very similar in size. This is consistent with the experimental results presented in chapter 5 where more positive transient charges are observed for the adjacent strips and an equal amount of positive and negative transient for the next-to-adjacent strips.

B.2 Comparison with experiments

Two slices are taken through the lateral positions 25 and 75 mm and are presented by the solid black line in figure B.3. The two positions are used to represent the response of the detector in the adjacent and next-to-adjacent strips. The graphs are normalised to a maximum of 1.

There is no induced current close to the contact (0 mm) because the angles are virtually all 90° . The weighting field reaches the maximum at a depth of 4 and 7 mm for 25 and 75 mm lateral position respectively. At the opposite side (20 mm), the weighting field is strongly reduced to 10% of the maximum for 25 mm and 35% for 75 mm. The weighting field shows a steep positive slope before the maximum. After the maximum, the slope becomes negative. The difference in gradient before and after the maximum is important

for the induced current and hence the polarity of the transient charges.

Having identified the weighting field of the (next-to-)adjacent strip, the transient charge response of the experimental measurements can be compared.

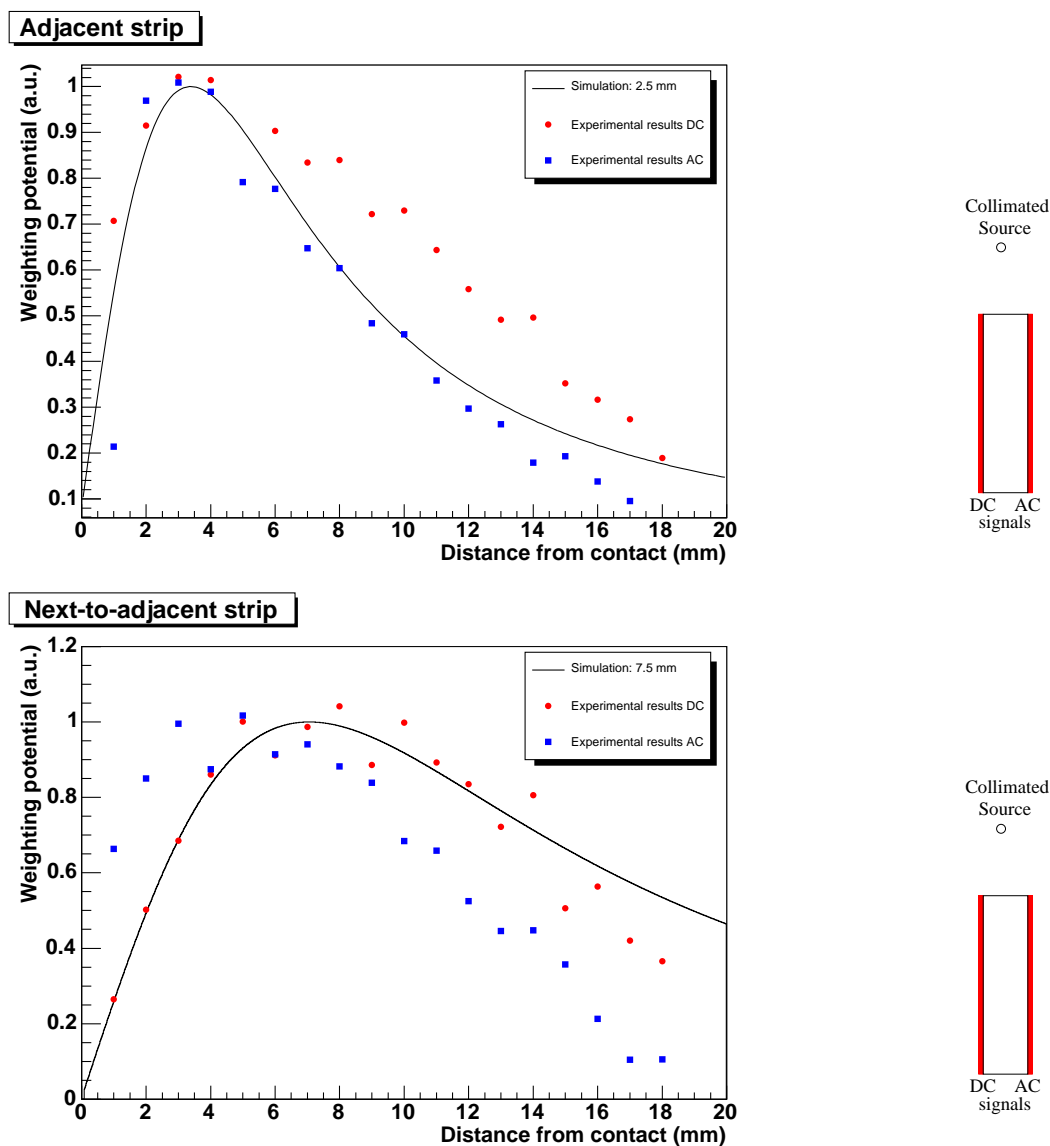


Figure B.3: The weighting field reconstructed compared with the data

A comparison has been made between the simulation and the experimental results. Before this can be done, the area has been studied for each depth (see figure 5.11). The values for the area of the transient charge represents the total charge induced over time. The

differential through depth is proportional to the induced current and hence the weighting field. The differential of both the AC and DC side is included in figure B.3. The simulation shows a good agreement with the experimental results for the AC side on the adjacent strip. The DC side does agree better for the next-to-adjacent strip. The difference between the AC and DC side is not as large as for the adjacent strip.

In most cases the weighting field is strongly reduced towards the opposite side of the strips. The reason for this is speculative but may be found in the electric field strength in these regions.

One parameter of influence on the induced current and which is not included in the model is the difference in mobility between the holes and electrons. Other factors which may explain the discrepancies are the interstrip gap and the contact thickness.

For a more precise method, the Poisson equation should be solved as described in chapter 2 using dedicated electric field simulations.

Appendix C

Average transient response within a strip

This appendix is used to show the transient response of strip AC05 and AC07. The side scan measurement is used. Only five lateral positions are used covering the AC06 strips which is where the real charge is present. Every average pulse shape is build out of ~ 800 pulse shapes. Only full energy events are used for the average. The transient charges are scaled the same amount as the associated real charge which has a height of 1000.

On the following pages, the 400 signals are drawn. They are split up into two main sections, the adjacent and the next-to-adjacent response. The sections are divided into 20 depths (1 - 20 mm) and 5 lateral positions (a - e). Each graphs have two signals in to differentiate the response of AC05 (blue lines) and AC07 (red lines).

The middle lateral position (c) corresponds to the middle of the strip. The response for the strips either side of this position is very similar throughout the complete depth for all the signals. The depth dependence is as expected similar to the average pulse shapes shown in figure 5.9.

Other lateral positions are showing the asymmetry effect. If the interaction are close to the border of AC05 (positions a), AC05 has a larger transient charge reponse in than AC07. For the position where the interactions are close to the AC06, the transient charge in AC06 is larger. In section 2.6, a similar shape has been assumed for each lateral position inside the strip. However, these signals shows a slight difference in shape for different lateral

positions. The difference is not enough to develop a different analysis method.

The improvement in the position resolution is done in chapter 5. The asymmetry value for the different lateral positions is used for that. A problem occurred for the region in the adjacent strips, where the transient charge is bipolar. From the responses shown, it can be concluded that there is a difference between the each lateral and depth position for this region. The amount of difference is not enough to use it for a measure of lateral position.

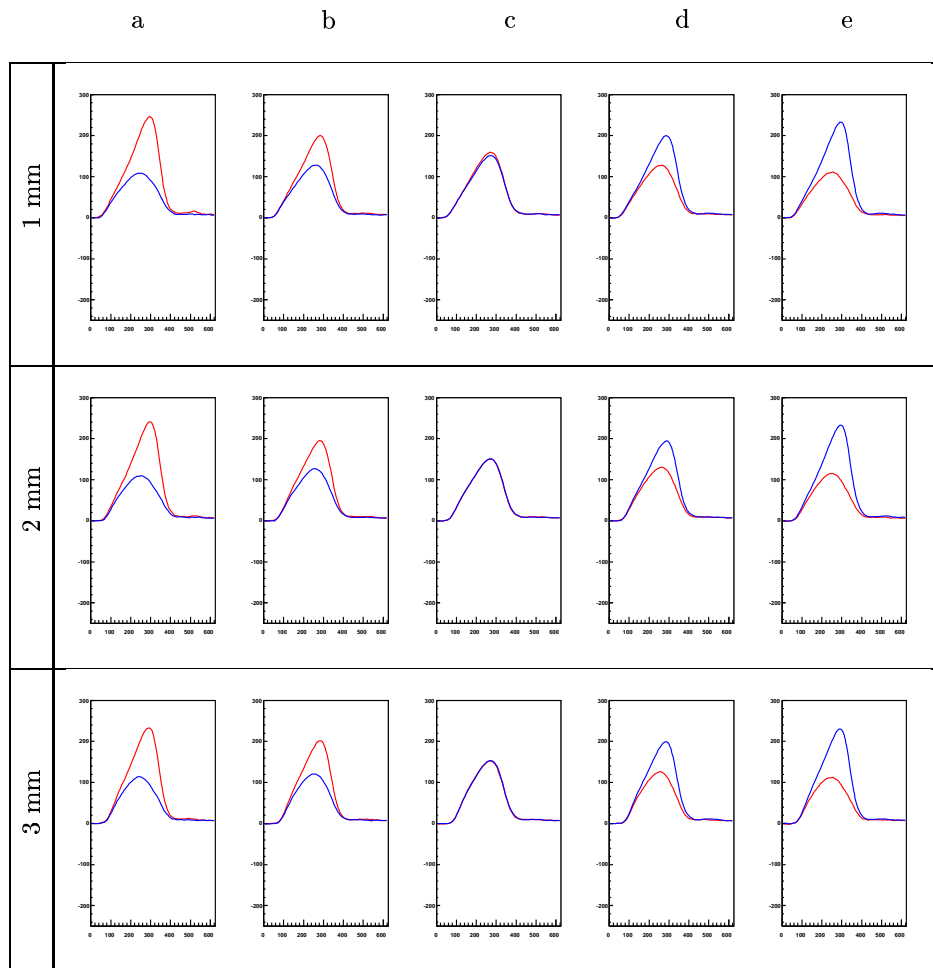


Table C.1: Adjacent transient charges for depths 1 - 3 mm

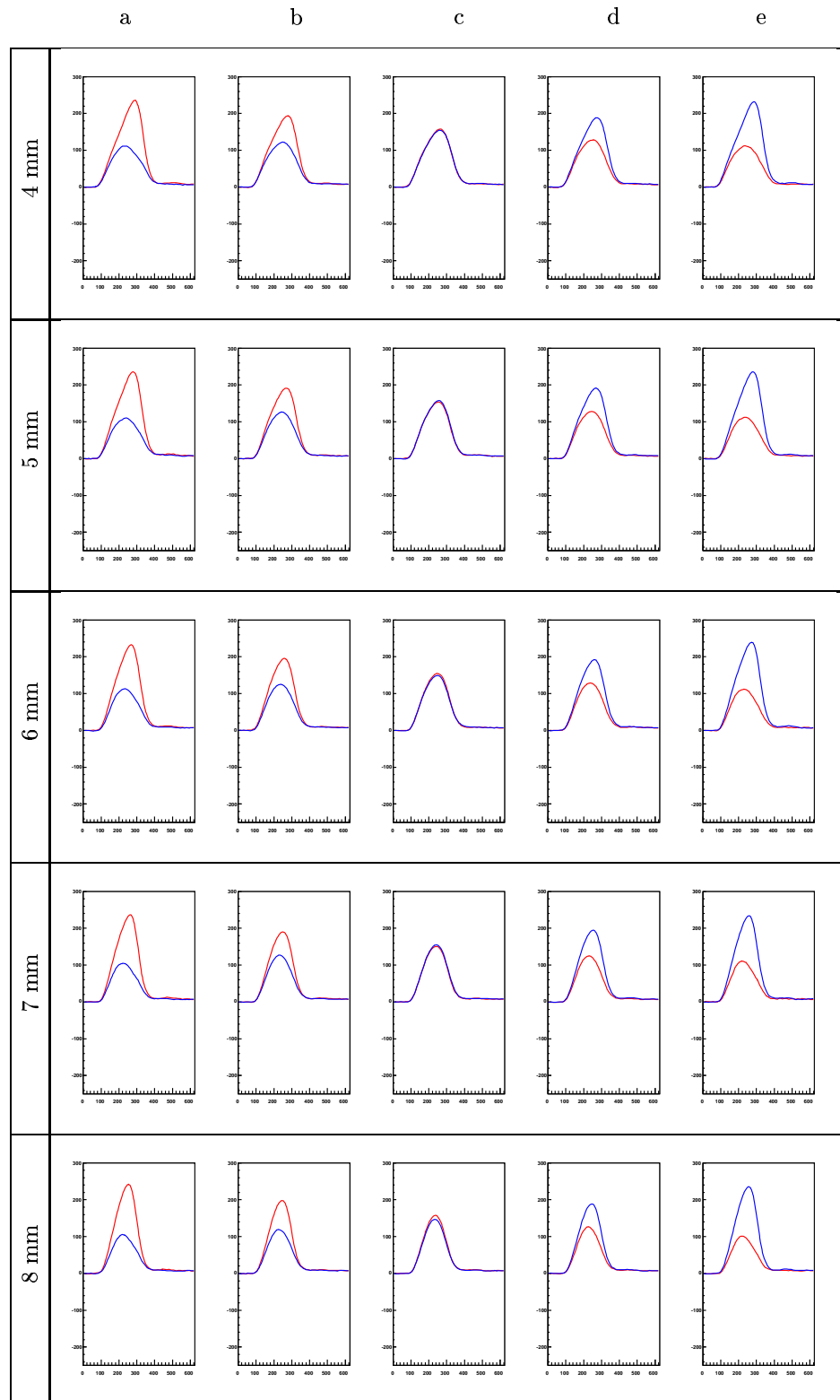


Table C.2: Adjacent transient charges for depths 4 - 8 mm

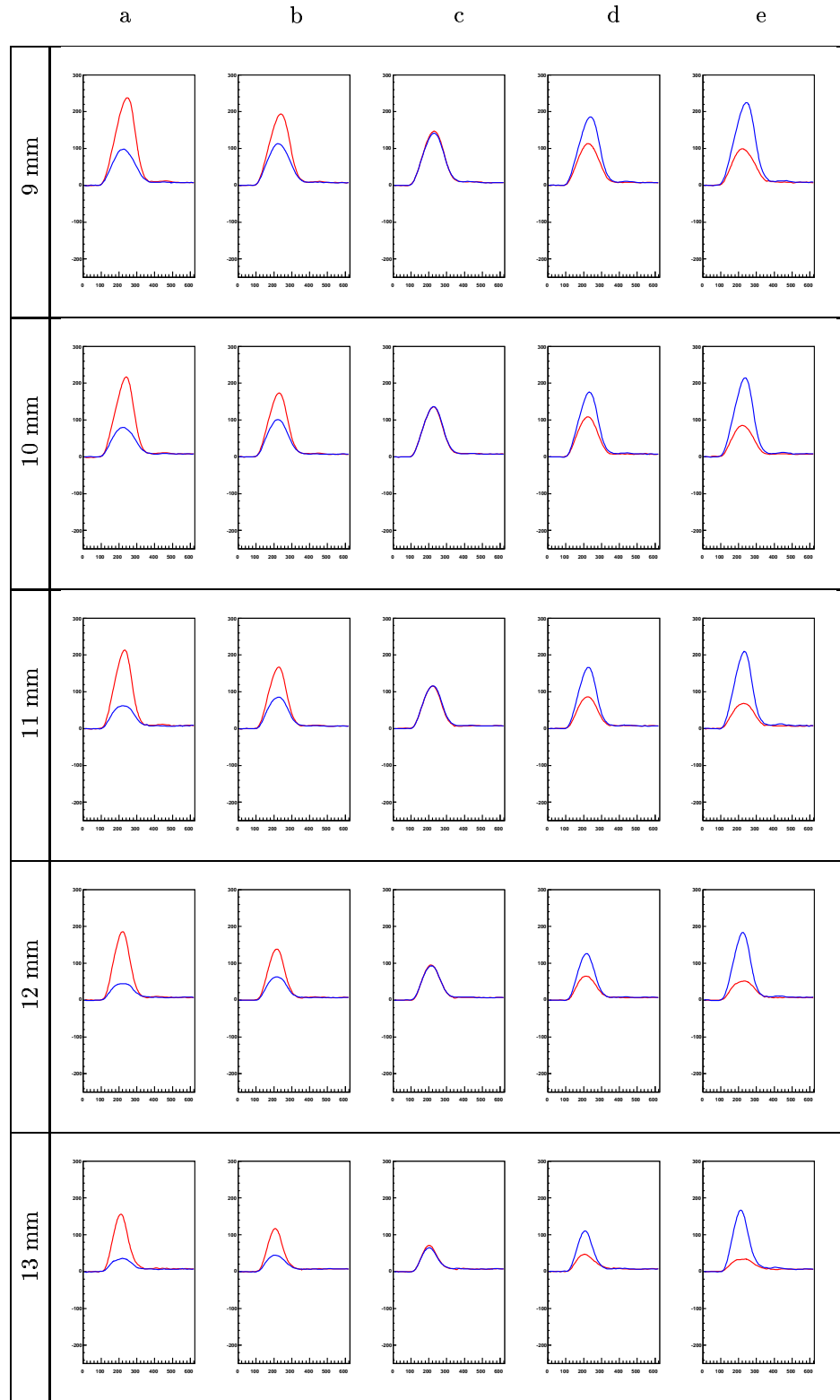


Table C.3: Adjacent transient charges for depths 9 - 13 mm

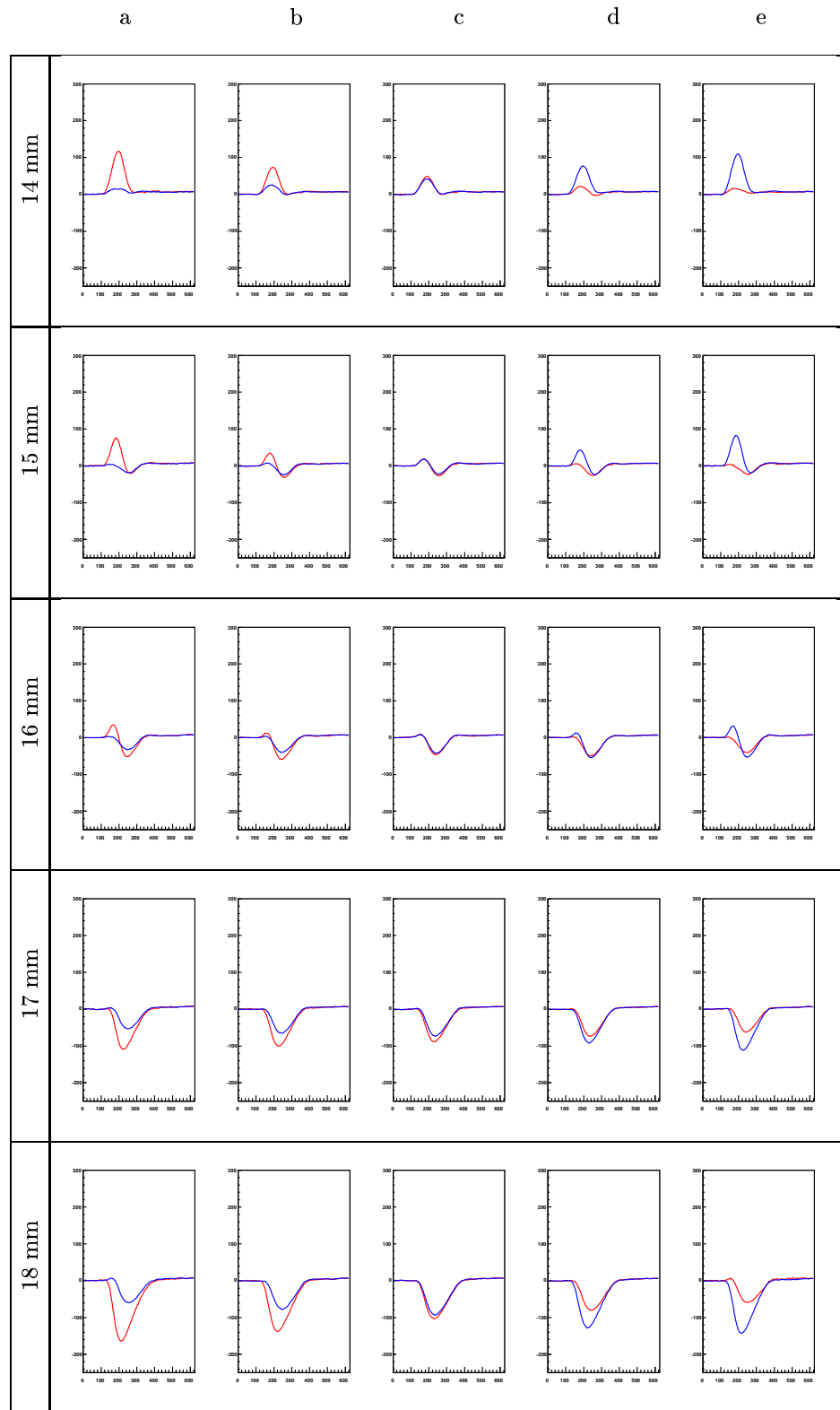


Table C.4: Adjacent transient charges for depths 14 - 18 mm

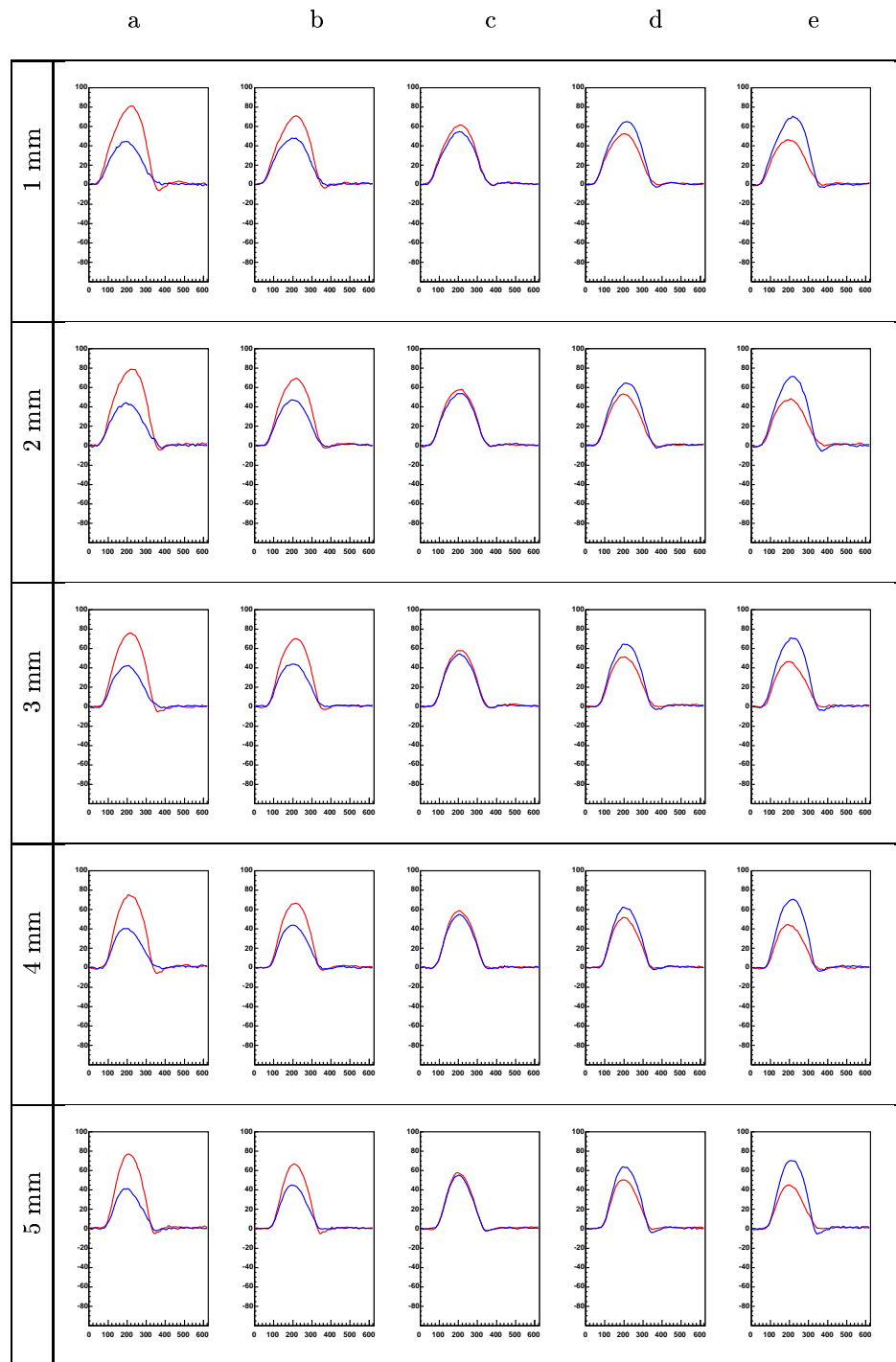


Table C.5: Next-to-adjacent transient charges for depths 1 - 5 mm

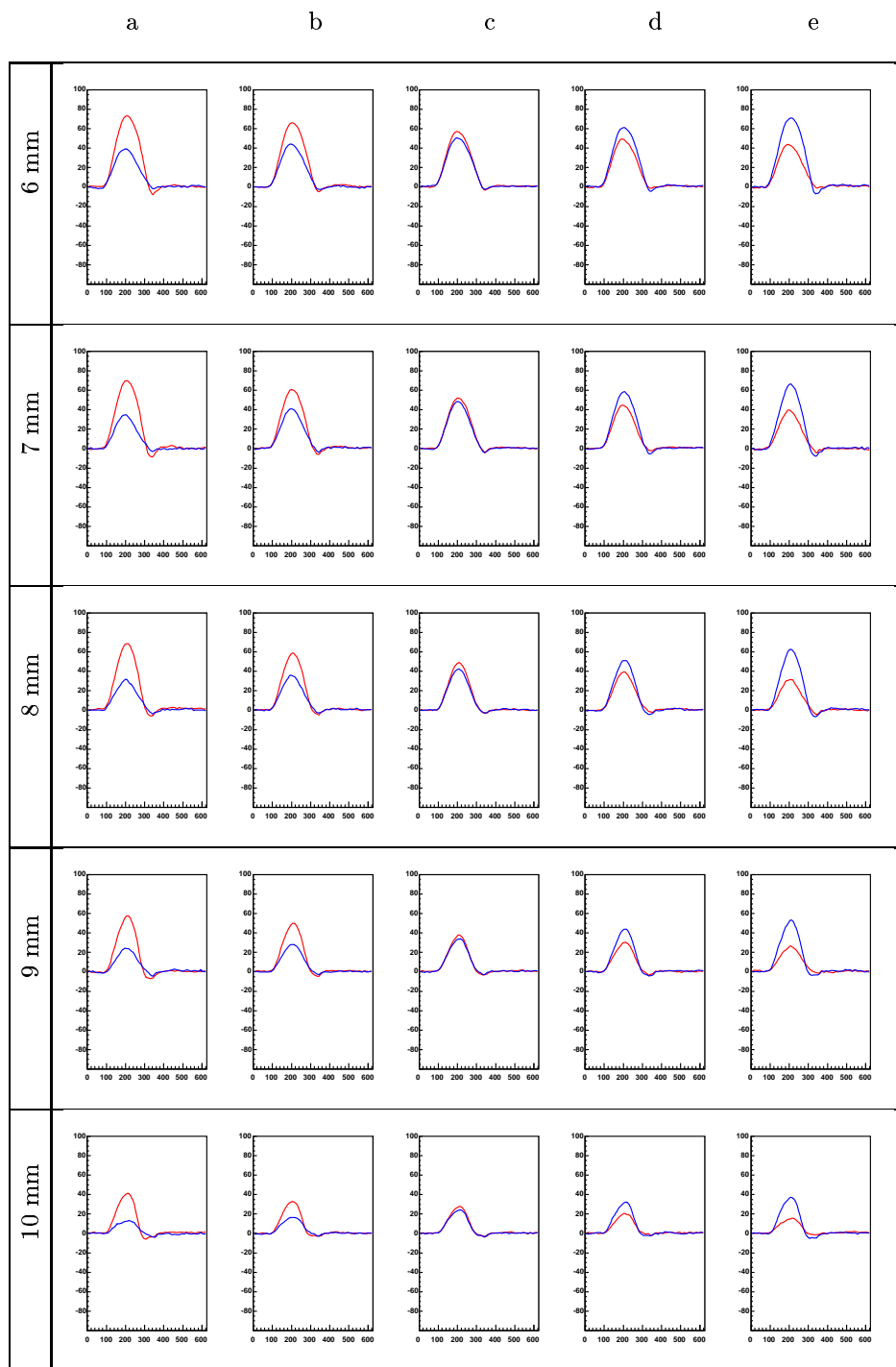


Table C.6: Next-to-adjacent transient charges for depths 6 - 10 mm

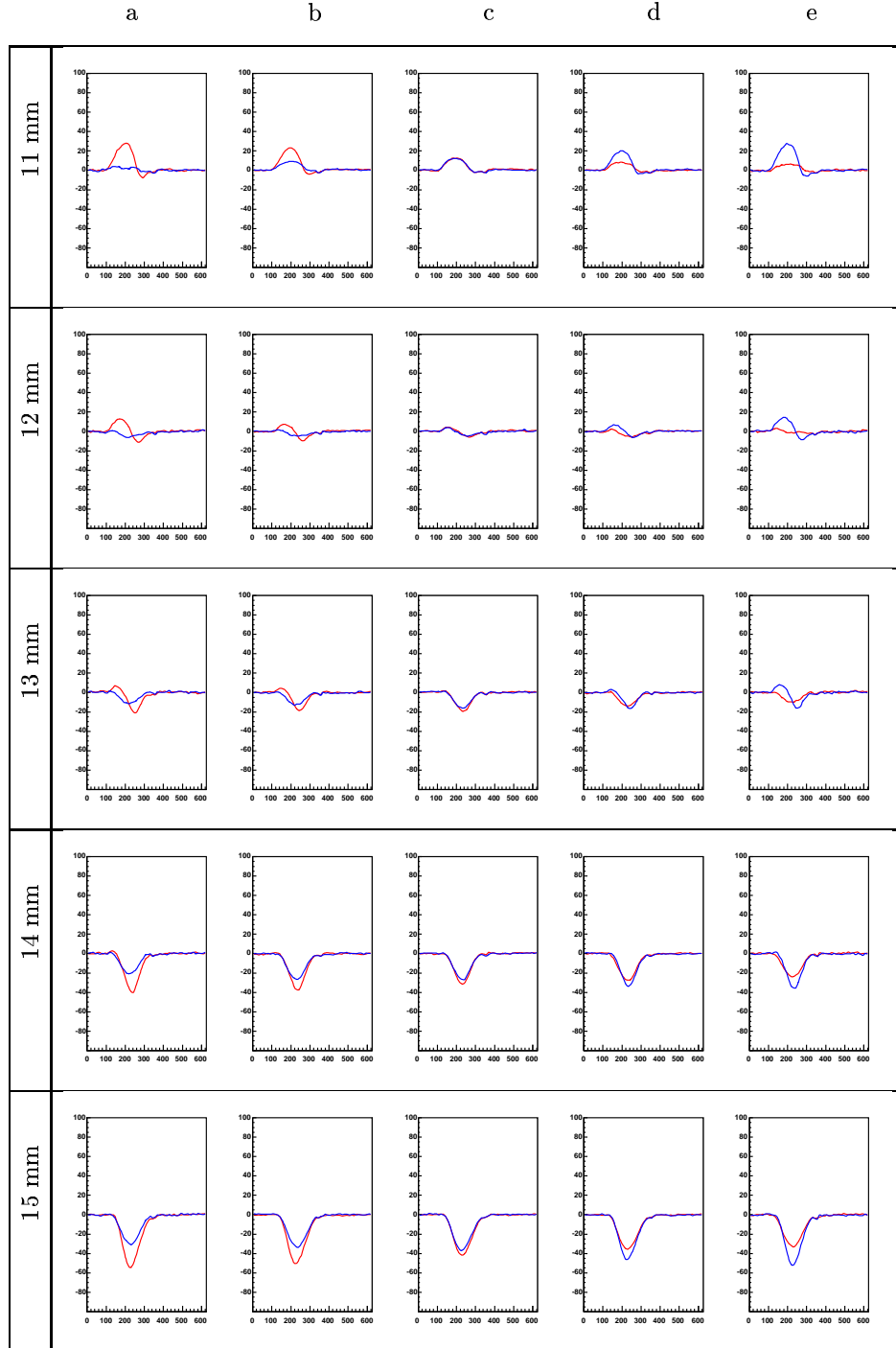


Table C.7: Next-to-adjacent transient charges for depths 11 - 15 mm

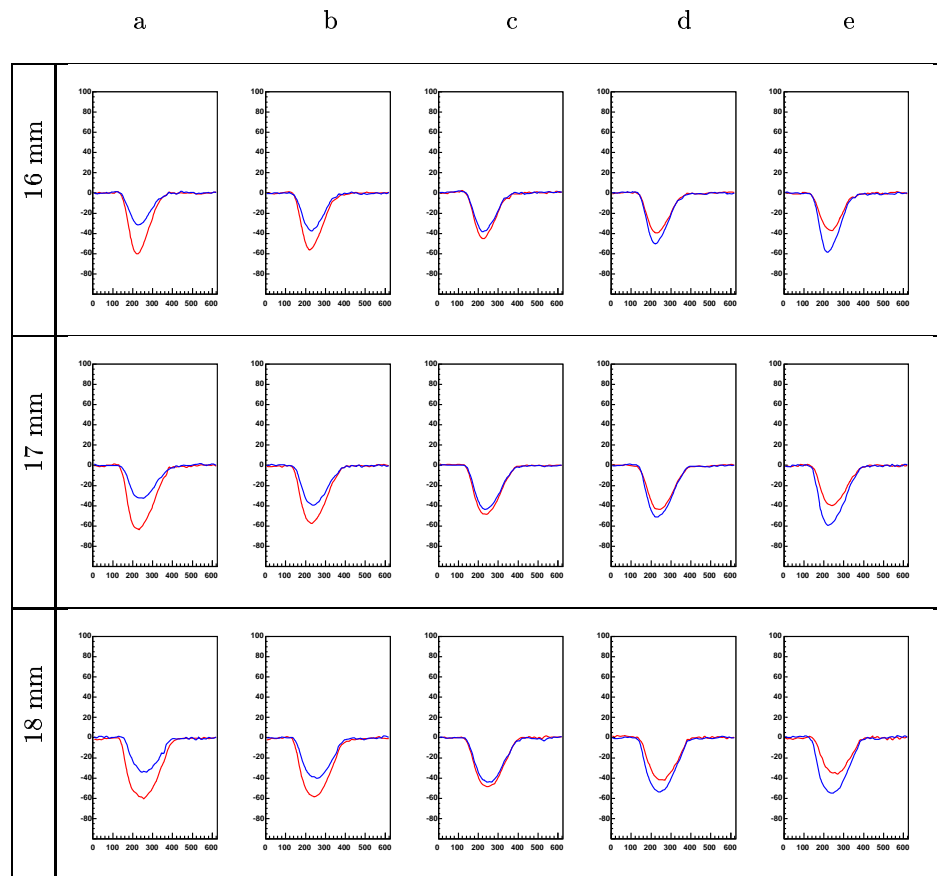


Table C.8: Next-to-adjacent transient charges for depths 16 - 18 mm

Appendix D

Position resolutions

In the following table, the lateral position resolutions for all depths have been included.

Depth (mm)	Position resolution of the AC side from collimator position (mm)						Position resolution of the AC side from reconstructed position (mm)						Position resolution of the DC side from reconstructed position (mm)				
	1	2	3	4	5	Average	1	2	3	4	5	Average	1	2	3	4	Average
DC side																	
1	1.66	1.80	1.71	1.90	1.80	1.77	0.94	1.07	1.01	0.82	0.98	0.96	1.13	1.29	1.26	0.87	1.14
2	1.44	1.79	1.71	1.81	1.90	1.73	0.87	1.08	0.97	1.06	1.02	1.00	1.61	1.57	1.53	1.43	1.54
3	1.63	1.96	1.72	1.88	1.80	1.80	1.05	1.18	1.11	1.11	1.16	1.12	3.59	3.21	2.99	3.42	3.30
4	1.65	1.80	1.66	1.98	1.85	1.79	1.09	1.14	1.14	1.16	1.17	1.14	3.42	14.54	13.34	12.95	13.64
5	1.57	1.86	1.71	1.83	1.86	1.77	1.11	1.22	1.17	1.12	1.13	1.15	7.57	6.80	6.59	7.20	7.04
6	1.72	1.83	1.72	1.80	1.95	1.81	1.18	1.19	1.16	1.17	1.21	1.18	3.56	3.31	3.24	3.58	3.42
7	1.56	1.72	1.66	1.76	2.10	1.76	1.32	1.21	1.18	1.22	1.23	1.23	1.97	2.04	2.04	1.95	2.00
8	1.59	1.76	1.70	1.83	1.78	1.73	1.09	1.20	1.10	1.14	1.23	1.15	1.68	1.89	1.98	1.74	1.82
9	1.77	1.95	1.64	1.98	1.86	1.84	1.07	1.31	1.15	1.20	1.22	1.89	1.71	1.71	1.70	1.60	1.68
10	1.87	1.88	1.76	1.84	1.99	1.87	1.19	1.19	1.20	1.21	1.24	1.21	1.56	1.68	1.73	1.58	1.64
11	1.92	1.89	1.70	1.91	1.82	1.85	1.17	1.34	1.20	1.23	1.51	1.22	1.52	1.65	1.67	1.50	1.58
12	1.74	1.86	1.69	1.83	1.62	1.75	1.34	1.42	1.35	1.31	1.46	1.38	1.51	1.65	1.62	1.53	1.58
13	2.00	1.99	1.62	1.93	2.05	1.92	5.90	1.97	1.92	1.74	2.21	2.75	1.54	1.59	1.49	1.60	1.56
14	2.47	2.11	1.80	2.08	2.30	2.15	1.08	1.10	1.03	-	-	1.07	1.56	1.65	1.60	1.61	1.60
15	2.92	2.24	1.86	2.04	3.09	2.43	2.86	2.46	2.24	2.39	2.85	2.56	1.53	1.65	1.71	1.60	1.62
16	5.78	3.53	2.97	3.83	5.48	4.32	12.41	10.21	9.28	9.58	11.77	10.65	1.53	1.74	1.66	1.68	1.65
17	59.85	39.15	31.32	38.04	55.42	44.76	9.69	7.99	6.75	7.52	9.12	8.21	1.67	1.71	1.86	1.67	1.73
18	6.37	3.50	3.20	3.71	5.12	4.48	2.01	1.82	1.98	1.81	2.31	1.98	1.59	1.63	1.81	1.51	1.63
19	8.70	6.56	4.53	5.50	10.58	7.18	1.23	1.19	1.37	1.21	1.07	1.21	1.63	1.73	1.83	1.90	1.72
20	7.14	5.15	3.36	4.65	7.65	5.59	-	-	-	-	-	-	1.45	1.64	1.58	1.32	1.50
AC side																	

Table D.1: The position resolution based on the Rayleigh criterion for the lateral position as a function of depth. The position resolutions over 5 mm are due to the method chosen for the calculation. (-) means no peak could be identified in the distribution.

References

- [Aga01] Gerl, J., Korten, W., (2001):*An Advancend Gamma Tracking Array for the European Gamma Spectroscopy Community.*
- [Cha02] Chatziioannou, A.F. (2002): *PET Scanner Dedicated to Molecular Imaging of Small Animal Models.* Molecular Imaging and Biology, Vol.4, p. 47-63.
- [Dav52a] C.M. Davisson and R.D. Evans (1952) *Gamma-Ray Absorbtion Coefficients* Reviews Modern Physics, Vol. 24, No.2. p. 82 - 94
- [Dav52b] C.M. Davisson and R.D. Evans (1952) *Gamma-Ray Absorbtion Coefficients* Reviews Modern Physics, Vol. 24, No.2. p. 86
- [Dav65] Davisson, C.M. (1965): Interaction of γ -Radiation with Matter *Alpha-, Beta- and Gamma Ray Spectroscopy.* Ed. by Siegbahn, K. Pub. bu North-Holland, p37-78.
- [Fan47] Fano, U., Phys. Rev. 72, 26 (1947).
- [Geo93] Georgiev, U. and Gast, W. (1993): *Digital Pulse Processing in High Resolution, High Throughput Gamma-Ray Spectroscopy,* IEEE Transactions on nuclear science, Vol. 40, No.4, p. 770-779.
- [Ham96] Hamel, L.A. and Paquet, S. (1996):*Charge transport and signal generation in CdTe pixel detectors* Nuclear Instruments and Methods in Physics Research Section A, 380, P. 238-240
- [Har84] (1984): *Harshew Radiation Detectors Catalogue*

- [Kno00a] Knoll, G.F. (2000): *Radiation Detection and Measurement*, third edition, John Wiley & Sons, Inc. p. 611.
- [Kno00b] Knoll, G.F. (2000): *Radiation Detection and Measurement*, third edition, John Wiley & Sons, Inc. p. 116.
- [Kno00c] Knoll, G.F. (2000): *Radiation Detection and Measurement*, third edition, John Wiley & Sons, Inc. p. 116-117.
- [Knp65] Knop, G., Paul, W. (1965): Interaction of Electrons. Ed. by Siegbahn, K., Pub. by North-Holland, p. 12.
- [Kro99] Kroeger, R.A. et.al. (1999): *Charge spreading and position sensitivity in a planar germanium detector*, Nuclear Instrumentation and Methods in Physics A, 422, p. 206-210.
- [Lan84] Lange, K., Carson, R. (1984) *EM reconstruction algorithms for mission and transmission tomography* J. Comput. Asst. Tomogr., Vol. 8 No. 2, p. 306-316.
- [Laz04] I. Lazarus et.al. (2004) IEEE Trans. Sci. NS-51, 4, 1353.
- [MCN] <http://www.laws.lanl.gov/x5/MCNP/index.html>
- [Mih00] Mihailescu L. et.al. (2000) *The influence of Anisotropic Electron Drift Velocity on the Signal Shapes of Close-End HPGe detectors*. Nuclear Instrumentation and Methods in Physical Research A, 447, p. 350-360.
- [Mil05] Milechina, L. and Cederwall, B. (2005) *3D position sensitivity of a highly segmented Ge detector* Nuclear Instruments and Methods in Physics Research A, 550, p. 278-291.
- [Mis04] Missimer, J. et. al. (2004) *Performance evaluation of the 16-module quad-HIDAC small animal PET camera* Phys. Med. Biol. 49 p. 2069-2081
- [Nol94] Nolan, P.J. et.al. (1994) *Large Arrays of Escape-Suppressed Gamma-Ray Detectors*. Annual Review of Nuclear and Particle Science, Vol. 45, p. 561-607.
- [NSM] <http://www.ioffe.ru/SVA/NSM/Semicond/Ge>

- [Ort] <http://www.ortec-online.com/pdf/preamptut.pdf>
- [Rad88] Radeka V., *Ann. Rev. Nucl. Part. Sci.* 38 (1988) p. 217-277.
- [Ram39] Ramo, P.I.R.E. 27 (1939) 584
- [Rea03] Reader, A.J. et.al. (2003): *EM Algorithm System Modeling by Image-Space Techniques for PET Reconstruction* IEEE Transaction on Nuclear Science, Vol. 50, p. 1392 - 1397.
- [She82] Shepp, L.A., Vardi, Y. (1982): *Maximum likelihood reconstruction for emission tomography* IEEE Trans. Med. Imaging, vol. MI-1 p. 113-122.
- [Sho38] Shockley, W. (1938): *Currents to Conductors Induced by a Moving Point Charge*. Journal of Applied Physics, Issue 10, p. 635.
- [Sze02a] Sze, S.M., (2002): *Semiconductor Devices, Physics and Technology*, second edition, John Wiley & Sons, Inc., p. 48.
- [Sze02b] Sze, S.M., (2002): *Semiconductor Devices, Physics and Technology*, second edition, John Wiley & Sons, Inc., p. 93-99.
- [Spi01] Spieler, H. (2001): *Radiation Detectors and Signal Processing - II. Signal Formation* Heidelberger Graduate Lectures in Physics, p. 68.
- [Tar03] Tarantola, G. et.al. (2003): *PET Instrumentation and Reconstruction Algorithms in Whole-Body Applications* The Journal of Nuclear Medicine, Vol. 44, No. 5, p. 756-769.
- [Va03] Valk, P.E. et.al. (2003), *Position Emission Tomography, Basic Science and Clinical Practice*, (Springer-Verlag London Berlin Heidelberg)